UC Santa Barbara
UC Santa Barbara Electronic Theses and Dissertations

Title

Probing condensed matter order with nitrogen-vacancy center scanning magnetometry

Permalink

https://escholarship.org/uc/item/3kk5r27m

Author

Jenkins, Alec

Publication Date

2019

Peer reviewed|Thesis/dissertation

University of California
Santa Barbara

Probing condensed matter order with nitrogen-vacancy center scanning magnetometry

A dissertation submitted in partial satisfaction
of the requirements for the degree

Doctor of Philosophy
in
Physics

by

Alec Alvin Jenkins

Committee in charge:

    Professor Ania Bleszynski Jayich, Chair
    Professor Andrea Young
    Professor Boris Shraiman

September 2019

The Dissertation of Alec Alvin Jenkins is approved.

_____

Professor Andrea Young

_____

Professor Boris Shraiman

_____

Professor Ania Bleszynski Jayich, Committee Chair

July 2019

Probing condensed matter order with nitrogen-vacancy center scanning magnetometry

Acknowledgements

Curriculum Vitæ
Alec Alvin Jenkins

Education

2019	Ph.D. in Physics, University of California, Santa Barbara.
2017	M.A. in Physics, University of California, Santa Barbara.
2013	B.A in Physics, University of Colorado, Boulder.
2013	B.A in Mathematics, University of Colorado, Boulder.

Publications

Alec Jenkins, Matt Pelliccione, Guoqiang Yu, Xin Ma, Xiaoqin Li, Kang Wang, and Ania Jayich, "Single spin sensing of domain wall structure and dynamics in a thin film skyrmion host", Phys. Rev. Mater., 3(8), 083801 (2019).

Guoqiang Yu, Alec Jenkins, Xin Ma, Seyed Armin Razavi, Congli He, Gen Yin, Qiming Shao, Qing lin He, Hao Wu, Wenjing Li, Wanjun Jiang, Xiufeng Han, Xiaoqin Li, Ania C. Bleszynski Jayich, Pedram Khalili Amiri and Kang L. Wang, "Antiferromagnet-stabilized room-temperature skyrmions in the absence of an external magnetic field", Nano Lett. 18 (2), 980-986 (2018).

Matthew Pelliccione, Alec Jenkins, Preeti Ovartchaiyapong, Christopher Reetz, Eve Emmanouilidou, Ni Ni, Ania C. Bleszynski Jayich, "Scanned probe imaging of nanoscale magnetism at cryogenic temperatures with a single-spin quantum sensor", Nature Nano. AOP, DOI: 10.1038/nnano.2016.68 (2016).

Abstract

Probing condensed matter order with nitrogen-vacancy center scanning magnetometry

by

Alec Alvin Jenkins

The development of new scientific instruments often leads to the observation of new physical phenomena. In this thesis, I will describe a new imaging instrument aimed at uncovering and understanding electronic and magnetic phenomena arising on the nanometer length scale. In recent years, the nitrogen-vacancy center in diamond (NV) has emerged as a unique tool for sensing magnetic fields with high spatial resolution. We have extended these sensing capabilities to a wide temperature range and harnessed this temperature control to probe the emergence of nanoscale collective order in condensed matter systems. The NV center has properties that make it an ideal tool for this purpose: it is an atomic-sized defect with a spin that can be optically initialized and read-out, it is noninvasive, and it retains quantum coherence from cryogenic to room temperature. In this thesis, I will describe the design and construction of a variable temperature scanning microscope built around the sensing capabilities of single NV centers. I will also describe the design and fabrication of the NV sensors themselves. The scanning microscope consists of a confocal microscope for addressing NVs, an atomic force microscope housed in a closed-cycle optical cryostat, and single-crystal diamond probes containing NV centers. Scanning NV magnetometry excels in probing systems that require good magnetic field sensitivity and high spatial resolution. I will describe how we have applied this measurement technique to several condensed matter systems that display magnetic or electronic structure on the nanometer to micrometer scale. I will focus on our measurements of magnetic skyrmions, where we show that NV magnetometry can be used to simultaneously probe the structure

and dynamics of chiral domain walls. And I will describe our measurements exploring different regimes of electron transport in graphene, where the NV is used as local probe of current density, in search for signatures of electron hydrodynamic behavior.

Contents

Chapter 1

Introduction

Starting with the invention of the compound light microscope in the 1600s, advances in microscopy and imaging have been followed by leaps in our understanding of condensed matter systems, both in the study of hard condensed matter, and in soft condensed matter and biology. Often these advances are related to improvements in resolution, which allow scientists to uncover spatial order that was previously hidden at small length scales. Sometimes, however, these advances stem from the development of a totally new sensing modality. In this thesis, I will describe the development of a new microscopy tool based on the nitrogen-vacancy center in diamond (NV), used primarily for hard condensed matter research. The NV at the heart of this microscope is a single spin with long quantum coherence times over a wide temperature range. Much of the power of this new tool comes from the NV's robustness and versatility. In this thesis, I will describe how this tool is used for the high resolution microscopy of novel order of several condensed matter systems, including magnetic skyrmions and regimes of current flow in graphene.

The role of scanning microscopy experiments in condensed matter research is somewhat determined by the relative slowness and technical difficulty of these measurements compared to transport or bulk material measurements. This has typically meant that scanning imaging of hard condensed matter systems has been used to validate existing

models that were developed to describe the results of transport or bulk-type measurements. This is in contrast to the situation in biological research, where optical microscopy has historically played a more active role in uncovering unexpected phenomena. This difference may be due to the comparative ease with which biological systems can be probed with optical microscopy, or could be related to the complexity of biological systems versus hard condensed matter systems. In hard condensed matter physics, we are often concerned with the behavior of the same basic components— electrons, spins, or phonons in some kind of periodic structure. In this respect, the amount of complexity and diversity that emerges out of these systems is kind of amazing. But unfortunately for scanning microscopists of hard condensed matter systems, the level of complexity is still no match for the imagination of condensed matter theorists aimed at any new puzzling results from comparably fast bulk characterization measurements. There are an abundance of hard, unsolved problems in condensed matter physics, and scanning microscopy is an excellent tool for studying these problems, but scanning experiments tend to be used for validation or refinement of a particular model. Transport and bulk measurements can often play the validation role as well but seem to have a much higher probability of uncovering new, perplexing phenomena than do scanning microscopy experiments. The main exception to this categorization is maybe in the ability of microscopy to highlight the importance of local defects and disorder, whose effects can be easily overlooked in bulk measurements. The role of scanning microscopy as a validation tool, as well as a tool for examining the effects of local disorder, is demonstrated in this thesis, where scanning NV measurements are used to clarify the results of lower-resolution measurements of magnetic skyrmions in Chapter 4, and transport measurements of electron hydrodynamics in Chapter 5.

(a)

(b)

(c)

B_{NV} (G)

500 nm

(d)

$|j|$ (A/m)

2 µm
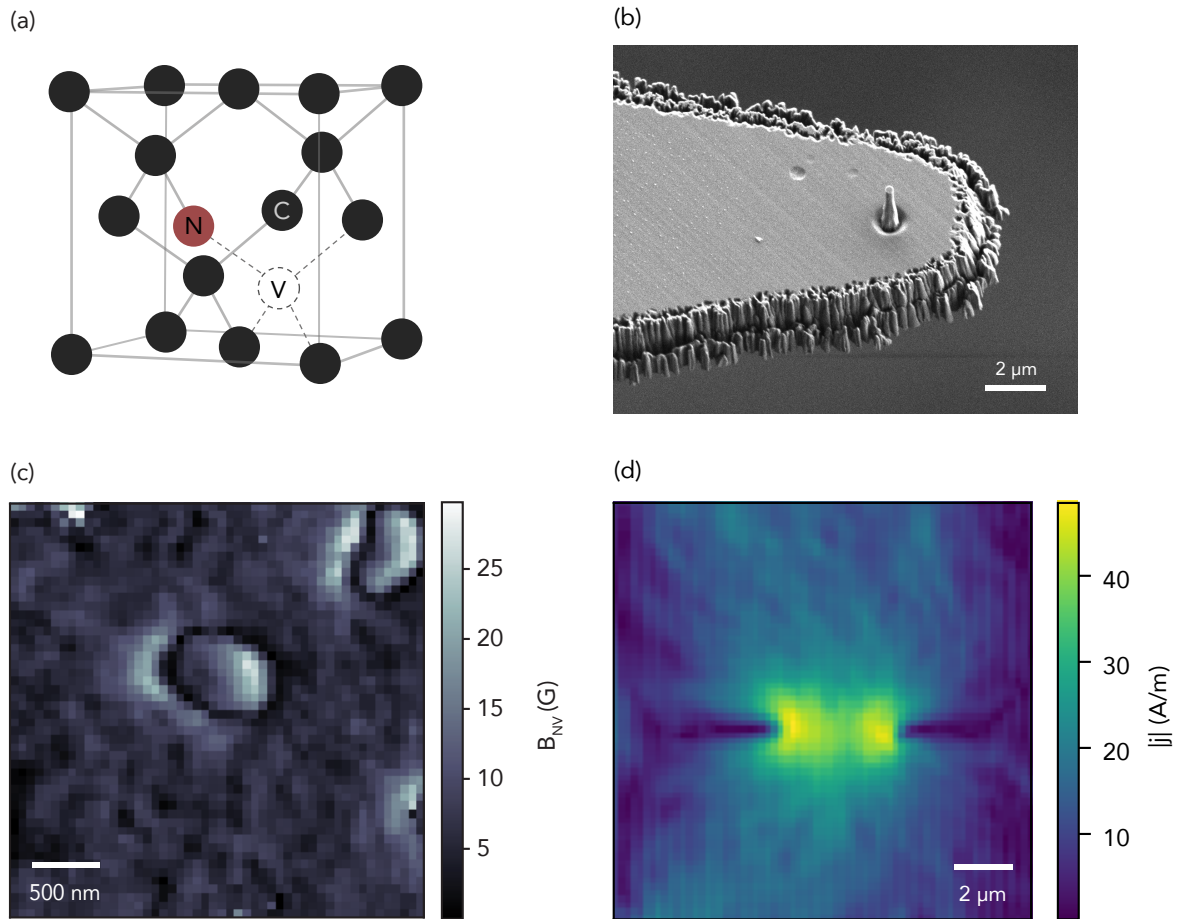
Figure 1.1: (a) Structure of the nitrogen-vacancy center defect in the diamond lattice. (b) SEM image of a diamond probe used for scanning NV magnetometry. (c) Map of the magnetic field along the NV axis above a magnetic bubble in thin film Ta/CoFeB/MgO. (B) Reconstructed map of the current density, showing ohmic flow through a constriction in graphene.)

Chapter 2

Nitrogen-vacancy center magnetometry

The NV defect has a few key features that make it a powerful sensor of magnetic fields: it is a spin-1 defect, with a spin state that can be optically initialized and read-out; it's read-out mechanism is noninvasive to many condensed matter systems; it has long coherence times, giving it good magnetic field sensitivity; it operates from cryogenic temperatures to above room temperature; and its atomic scale gives it the ability to image magnetic fields with high spatial resolution. This chapter describes the structure of the NV from the point of view of using the NV as a sensor of magnetic fields.

2.1   Electronic structure of the NV center

The NV is a diamond defect center composed of a single, substitutional nitrogen atom and a neighboring lattice vacancy. The electronic structure is determined by a combination of the C_{3v} symmetry of the defect and the number of electrons trapped in the defect. Three electrons are contributed from sp^3 dangling bonds of the vacancy-adjacent carbon atoms, two are contributed from the nitrogen atom, and for the sensing charge state, NV^-, another electron is borrowed from another defect somewhere else in the crystal. This charge state is referred to as the NV throughout this thesis.
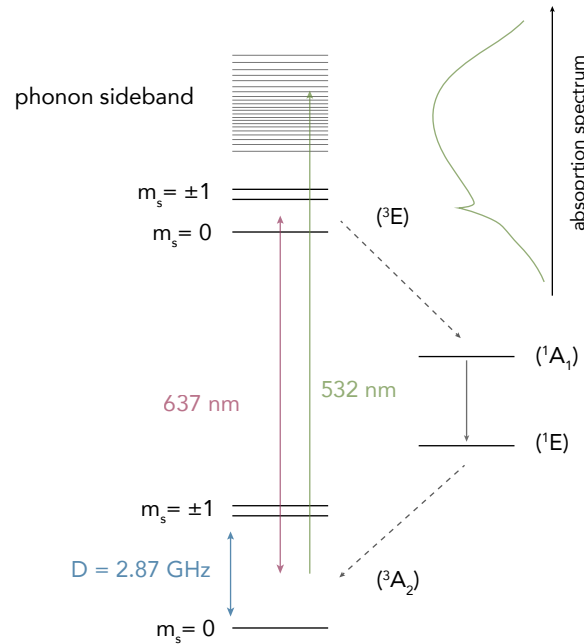
Figure 2.1: The room temperature electronic structure of the NV center. The ground state $^3A_2$ is a spin triplet with a crystal field splitting of 2.87 GHz between the $m_s = \pm 1$ and $m_s = 0$ spin states. The excited triplet state ^3E is separated from the ground state by 637 nm. In most magnetometry applications, transitions between $^3A_2$ and ^3E states are driven by excitation through a phonon sideband, using green laser light. Nonradiative transitions between the triplet states to the singlet states $^1A_1$ and ^1E can change the spin state, giving rise to spin polarization and optical contrast between the NV spin states.

The aspects of the electronic structure relevant for NV magnetometry are shown in Fig. 2.1. This structure has been determined by experimental and theoretical work over many decades [1–8]. The ground state $^3A_2$ is a spin triplet with a spin-spin induced crystal field splitting $D = 2.87$ GHz between the $m_s = \pm 1$ and $m_s = 0$ spin states. Transitions to the excited triplet state ^3E can be driven with 532 nm laser light through a broad phonon sideband. The NV will often then fluoresce a red photon through an emission sideband, in a spin-preserving cycle. But spin-orbit coupling also enables nonradiative intersystem crossings between these triplet states and the singlet states $^1A_1$ and ^1E. These crossings happen preferentially from the $m_s = \pm 1$ states of ^3E. This, combined

with the long lifetime of the ^1E state [9, 10], lead to the polarization of the NV spin state under optical illumination. This same process results in different fluorescence rates for the $m_s = \pm 1$ states and the $m_s = 0$ state. Combined, these two effects give rise to the optically detected magnetic resonance signal (ODMR) that NV magnetometry is built on. This signal is often referred to as the NV electronic resonance spectrum (ESR).
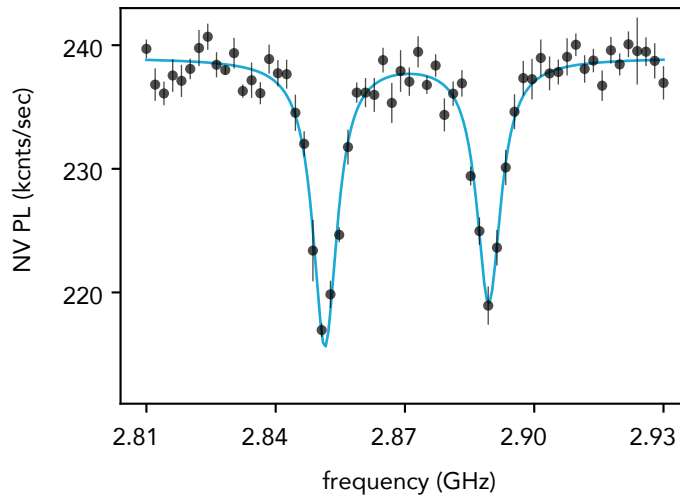
Figure 2.2: NV optically detected magnetic resonance spectrum (ODMR). This spectrum is measured by illuminating a single NV in a diamond pillar with 532 nm light and collecting the red fluorescence (NV PL), while running microwaves through a near-by wire. When the applied microwaves are off resonance, the green light polarizes the NV to the $m_s = 0$ spin state and the fluorescence level corresponds to brighter $m_s = 0$ state. When the microwave frequency is resonant with either the $m_s = 0 \leftrightarrow m_s = 1$ or $m_s = 0 \leftrightarrow m_s = -1$ transitions, the spin state population will be divided between the two states, as determined by a competition of polarization under optical illumination and the microwave transition rate. On resonance, the NV fluorescence rate will be given by a mixture of the fluorescence rates in the brighter $m_s = 0$ and the darker $m_s = \pm 1$ states. The splitting between the two resonance lines in this spectrum is proportional to the external magnetic field along the axis of the NV.

Figure 2.2 shows the ESR spectrum of a single NV in a diamond pillar. This is a continuous wave ESR signal, where the NV is constantly illuminated with green light while the frequency of applied microwaves is swept. The splitting between the two resonance

lines is proportional to the external magnetic field along the NV axis. Measuring changes in this splitting is the basis for almost all magnetic sensing NV experiments.

2.1.1   Ground state spin

Most NV sensing techniques are based on probing its ground state spin energy levels. The NV ground state spin can be described by the following Hamiltonian, ignoring hyperfine couplings for now, with $\hbar = 1$ and z along the NV axis[1],

$$H = \left(D + d_\parallel \Pi_z\right) S_z^2 + \frac{\gamma}{2\pi} \mathbf{S} \cdot \mathbf{B} - d_\perp \Pi_x \left(S_x^2 - S_y^2\right) + d_\perp \Pi_y \left(S_x S_y + S_y S_x\right) \qquad (2.1)$$

where D is the crystal field splitting (2.87 GHz at room temperature), $\mathbf{B}$ is the external magnetic field, $\mathbf{S}$ is the NV spin, $\gamma = 2\pi \times 2.8$ MHz/G is the gyromagnetic ratio, $d_\perp$ and $d_\parallel$ are couplings to perpendicular and parallel electric fields respectively, and $\Pi_{x,y,z}$ are the components of the total electric field, due to both external fields and effective electric fields due to crystal strain. We will be concerned with the magnetic response of the NV, usually in the regime where the strain and the external electric fields are small (an exception discussed in Appendix F is that the stray electric fields can be quite large near the edges of gated graphene devices). In the case the strain and electric field are negligible, NV spin is well described by

$$H = D S_z^2 + \frac{\gamma}{2\pi} \mathbf{S} \cdot \mathbf{B} \qquad (2.2)$$

and for $(\gamma/2\pi)B_\perp = (\gamma/2\pi)\sqrt{B_x^2 + B_y^2} \ll D$, the transition frequencies from the lower energy state to the upper two spin states is given by the field along the NV axis, $\Delta f_{1,2} =$

---

[1]In this chapter, the coordinate system is defined with z along the NV axis, while in later chapters z will be defined normal to the sample plane, and the field along the NV axis will be named B_{NV} in those chapters.

$D \pm (\gamma/2\pi)B_z$. If $B_\perp \ll B_z$, then the eigenstates will be the $|m_z = 0, \pm 1\rangle$ states. For increasing $B_\perp$, the eigenstates will be mixtures of these spin states, and the mean of the transition frequencies will shift higher but their splitting will still be proportional to B_z as long as $|B| \ll D$. In this range of external fields, $\Delta f_{1,2} = D + f_0 \pm (\gamma/2\pi)B_z$, where f_0 depends on the magnitude of $B_\perp$ relative to D and B_z. This is the regime relevant to all the scanning magnetometry measurements described in this thesis.

In NV magnetometry we would like to solve the inverse problem to that described above— we measure the transition frequencies and we want to use these frequencies to learn something about the magnetic field. Section 2.2.4 describes the calculation of B_z and $B_\perp$ from the measured transition frequencies.

2.1.2   NV spin coherence

A key feature of the NV spin is its long coherence times. The relevant coherence time for a DC magnetic field measurement is the dephasing time T_2^*, while the relevant coherence time for an AC measurement is T_2. These are the characteristic times of the NV phase coherence in a Ramsey (T_2^*) or Hahn echo/dynamical decoupling sequence (T_2), as described in 2.2.5. T_2^* determines the minimum achievable linewidth in an ESR measurement, and so ultimately contributes to the sensitivity of our measurement. Similarly, T_2 limits the phase accumulation time in an AC measurement and thus factors in to the AC sensitivity. The long coherence times of the NV are owed partly to the magnetically quiet environment of the diamond lattice, and partly to the high Debye temperature of diamond which gives low rates of spin-phonon bath coupling at room temperature (resulting in long longitudinal relaxation times, T_1). The main sources of magnetic noise intrinsic to the diamond are paramagnetic defects, including ^{13}C atoms, with a natural abundance of about 1%, and defects originating from our implantation

procedure, such as unpaired nitrogen atoms and vacancies. As discussed in Sec. 2.3.1, for very shallow NVs (< tens of nm from the diamond surface), paramagnetic and electronic defects at the diamond surface can become the main sources of decoherence.

2.1.3   Hyperfine interactions

The hyperfine structure of the NV arises from coupling between the electronic NV spin defect's nitrogen nuclear spin. This interaction can be described by

$$H_{hf} = A_{gs}^{\parallel} S_z I_z + A_{gs}^{\perp} \left(S_x I_x + S_y I_y \right) \tag{2.3}$$

where $A_{gs}^{\parallel} \simeq -2.2$ MHz for ^{14}N and $A_{gs}^{\parallel} \simeq 3.0$ MHz for ^{15}N. For ^{14}N, the interaction between the nuclear spin-1 and the NV electron spin splits each of the NV spin state transitions into three lines, spaced by 2.2 MHz. For the spin-1/2 ^{15}N, the transitions split into two lines separated by 3.0 MHz. For the CWESR measurements used for imaging, this hyperfine interaction is mostly relevant in that it is possible to achieve slightly better magnetic field sensitivity in CWESR measurements with the larger spectral spacing and larger contrast of the ^{15}N hyperfine.

2.1.4   Orbital states and transitions

The NV orbital structure gives rise to the optical spin state polarization and spin state read-out that are so crucial to NV sensing. Understanding the orbital structure and the symmetries of the different NV levels is thus important for understanding how the spin state polarization and read-out work and when these mechanisms will fail. A lot of information about the structure can be obtained by examining its symmetry. Starting from the defect's C_{3v} symmetry group, approximate molecular orbitals of the NV can be projected from arbitrary combinations of the dangling bonds onto each of the irreducible

representations of C_{3v} using the operator $\mathcal{P}^{(j)} = \frac{l_j}{6} \sum_R \chi^{(j)}(R)^* P_R$, where j labels the irreducible representation, l_j is the dimension of the jth representation, the sum over R runs over the 6 symmetry elements of this group, and P_R is the symmetry operator describing the group element R acting on the space of dangling bond functions. This calculation has been done nicely in several places [6, 7, 11, 12]. This process, combined with information obtained by including the Coulomb interaction, yields two lower-energy, nondegenerate, totally symmetric orbitals $a_1(1)$ and $a_1(2)$, and a pair of degenerate orbitals e_x and e_y. The six electrons of the NV$^-$ state are then distributed among these orbitals, filling up the lower energy $a_1(1)$ and $a_2(2)$ states and two of the four available $e_{x,y}$ states, giving the ground state configuration. The defect may be modeled equally well using these six electrons, or two holes in the remaining unoccupied states. In the hole picture the ground state has two spins in e states and is often labeled as e^2.

When the NV is excited optically, a hole is transferred from an e state to an $a_1(2)$ state, and this orbital excited state is labeled ea. The total symmetry of these states is set by the total two hole wave function, including the spin state. The ground state spin triplet has three levels and the excited orbital doublet and spin triplet has in general 6 levels. These states are shown in Fig. 2.3. Note that the orbital fine structure of the excited state shown here is washed out at room temperature as described below.

Some information about the relative intersystem crossing rates from the ^3E states to $^1A_1$ (shown in Fig. 2.1) can be obtained by looking at the symmetry of the states. For example the $|A_1\rangle$ triplet state is the only ^3E state directly coupled to a vibrationally excited level of the spin singlet $^1A_1$, and thus is expected to have the largest intersystem crossing rate, while the E_1 and E_2 states couple to $^1A_1$ through a second-order phonon process and their crossing rates are expected to be slower. And this is indeed what is observed when these rates are measured directly [13, 14]. At temperatures above $\sim$20 K, vibrations mix the excited orbital doublet states and the intersystem crossing rates

e^2 ae

$$|E_-\rangle \otimes |\uparrow\uparrow\rangle - |E_+\rangle \otimes |\downarrow\downarrow\rangle \quad A_1$$
$$|E_-\rangle \otimes |\uparrow\uparrow\rangle + |E_+\rangle \otimes |\downarrow\downarrow\rangle \quad A_2$$

$$|e_x e_y - e_y e_x\rangle \otimes \begin{cases} |\uparrow\uparrow\rangle & {}^3A_+ \\ |\uparrow\downarrow + \uparrow\downarrow\rangle & {}^3A_0 \\ |\downarrow\downarrow\rangle & {}^3A_- \end{cases}$$

$$|E_-\rangle \otimes |\downarrow\downarrow\rangle - |E_+\rangle \otimes |\uparrow\uparrow\rangle \quad E_1$$
$$|E_-\rangle \otimes |\downarrow\downarrow\rangle + |E_+\rangle \otimes |\uparrow\uparrow\rangle \quad E_2$$
$$|X\rangle \otimes |\uparrow\downarrow + \downarrow\uparrow\rangle \quad E_x$$
$$|Y\rangle \otimes |\uparrow\downarrow + \downarrow\uparrow\rangle \quad E_y$$

conduction band   conduction band

$\uparrow\uparrow$ —— $e_{x,y}$ $\uparrow\uparrow\downarrow$ —— $e_{x,y}$

$\uparrow\downarrow$ — $a_1(2)$ $\uparrow$ — $a_1(2)$

$\uparrow\downarrow$ — $a_1(1)$ $\uparrow\downarrow$ — $a_1(1)$

valence band   valence band
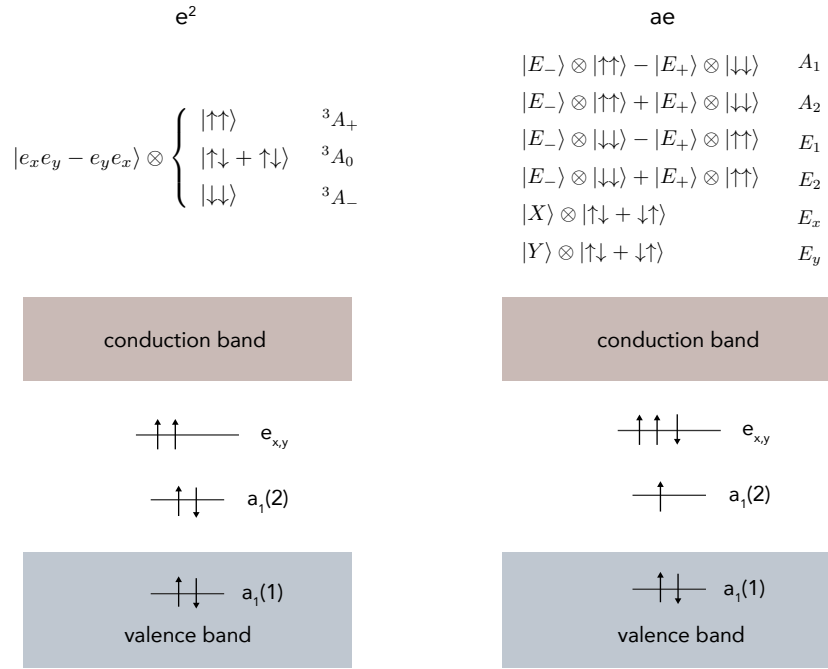
Figure 2.3: NV states shown schematically, relative to the diamond valence and conduction bands. The full two hole states are shown above in terms of the molecular orbitals $e_{x,y}$ and $a_1(2)$, where $|E_\pm\rangle = |ae_\pm - e_\pm a\rangle$, $|e_\pm\rangle = \mp(e_x \pm ie_y)$, $|X\rangle = (|E_-\rangle - |E_+\rangle)/2$, and $|Y\rangle = i(|E_-\rangle + |E_+\rangle)/2$ [6]. The name of each state is given to the right the state.

are given by the average rates over the relevant orbital states [15]. At room temperature the excited state is effectively an orbital singlet (the zero-field splitting D_{es} between the $m_s = 0$ and $m_s \pm 1$ states remains) and there are two intersystem crossing rates, a fast rate for the $m_s = \pm 1$ states and a much slower rate for the $m_s = 0$ state. This results in the spin polarization of the NV under optical illumination.

This polarization mechanism is spoiled by perpendicular magnetic fields, which lead to mixing of the $|m_s = 0, \pm 1\rangle$ states in the ground and excited orbital states. As a result of the mixing, the intersystem crossing rates for the different spin states are altered and, for example, the lowest energy spin level of the excited orbital, $|{}^3E\rangle |0\rangle \to c_0 |{}^3E\rangle |m_s = 0\rangle + c_1 |{}^3E\rangle |m_s = 1\rangle + c_2 |{}^3E\rangle |m_s = -1\rangle$ has a higher probability to undergo an intersystem crossing to the ${}^1A_1$ level. This reduces the optical spin state contrast. Due to the

crystal field spin state splittings of both the ground ($D_{gs} = 2.87$ GHz) and excited states ($D_{es} = 1.42$ GHz), in the low-field regime ($(\gamma/2\pi)|\mathbf{B}| \ll D_{gs}, D_{es}$) the spin state mixing and drop in contrast is mostly independent of the field component along the NV axis [16].

Examining the symmetry of the NV gives an intuition for the electronic structure and the allowed transitions, but more sophisticated *Ab initio* studies combined with experimental measurements are required whenever more quantitative descriptions are required. Studies like these [1–5, 7, 8, 13–15] have validated this simple symmetry-based model and converged on the electronic structure described above and shown in Fig. 2.1 and Fig. 2.3.

2.1.5   NV photophysics and photon statistics

In our scanning magnetometry experiments we typically prefer to use single NVs to probe the magnetic field, as this allows us to achieve high spatial resolution. The time-dependent fluorescence signal of a single emitter like the NV center displays non-classical correlations in fluorescence intensity. Measurements of these correlations are useful for determining whether our NV probes contain single NVs. Specifically, we measure the second-order time-intensity correlation function

$$g^{(2)} = \frac{\langle I(t+\tau)I(t)\rangle}{\langle I(t)\rangle^2} \tag{2.4}$$

to help determine if we have a single NV in a particular probe, where the measured intensity at time t is $I(t)$. Using single photon detectors, this function can be written as [17]

$$g^{(2)}(\tau) = P(t+\tau|t)/P(t) \tag{2.5}$$

where $P(t + \tau | t)$ is the probability to detect a photon at time $t + \tau$, given that a photon was detected at time t and $P(t)$ is the probability to detect a photon at any time t.

In practice this function is measured using two single photon detectors as shown in Fig. 2.4. Fluorescence from an NV(s) is collected in an optical fiber and a broad-band fiber 50:50 beamsplitter (custom from Gould Fiber Optics) is used to direct this fluorescence to two single-photon detectors based on silicon avalanche photodiodes (Excelitas SPCM-AQRH). These detectors output short TTL pulses, which are routed to a time-correlated single photon counting system (PicoHarp 300). We use the first input channel to trigger the timing of photon events on the second channel. Measured in this way, the correlation function is given by

$$g^{(2)}(\tau) = \frac{P(B_{t+\tau} | A_t)}{P(B_t)} \tag{2.6}$$

where probability $P(B_{t+\tau} | A_t)$ is the probability to receive a photon on detector B at time $\tau + t$, given that a photon was detected at time t on detector A, and $P(B_t)$ is the probability to receive a photon on detector B at arbitrary times t.

Understanding the $g^{(2)}$ correlation measurement of the NV requires an analysis that takes intersystem crossings into the singlet states into account. Figure 2.5 has an example of a $g^{(2)}$ signal measured on a diamond pillar. There is a sharp dip at $\tau = 0$ indicating that the probability of receiving a photon at detector B at the same time as one on detector A is lower than the probability to receive a photon at detector B at arbitrary times. The time of the exponential rise out of this dip is given by the radiative lifetime of the excited state, here measured to be about 12 ns. The $g^{(2)}$ signal then rises above the long-time average value of 1 before decaying back to this value over several hundred ns. The timescale of this second decay is given by the lifetime of the metastable singlet state. This dip below, and hump above, the level of $g^{(2)} = 1$ are described as anti-bunching and bunching of photons respectively. As the optical power is increased, the amplitude
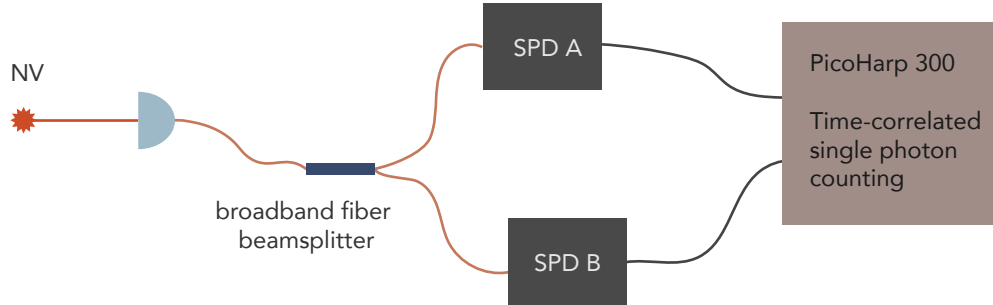
Figure 2.4: Setup for a $g^{(2)}$ correlation measurement. NV fluorescence is collected in an optical fiber, and a ~50:50 broadband fiber beamsplitter directs the fluorescence to two single-photon detectors. These detector emit short TTL pulses when a photon is detected and these pulses are routed to a Time-correlated single-photon counting system (TCSPC), capable of registering these pulse events wth picosecond level resolution. In the $g^{(2)}$ measurement, one input channel of this TCSPC is used as a trigger for events registered on the second channel. Making a histogram of events on channel B measured relative to a photon event on channel A gives a measurement of $P(B_{t+\tau}|A_t)$.

of the bunching hump gets larger, and the timescale of the second exponential decay decreases [17]. There is another feature, often visible in these $g^{(2)}$ measurements, that is an artifact caused by the limitations of the photon correlation hardware. The TCSPC is designed to detect only one photon per excitation cycle (where the excitation cycle is triggered by a photon received on detector A). This means that if the powers incident on the two detectors are about even, then there will be a non-negligible probably of receiving two or more photons on the second detector between photon events on the first, and these events won't be registered. This will lead to a decay in the measured $g^{(2)}$ over long times scales. To avoid this, the second detector should have a much lower incident fluorescence power than the first. This can be accomplished by loosening the fiber connection to SPD

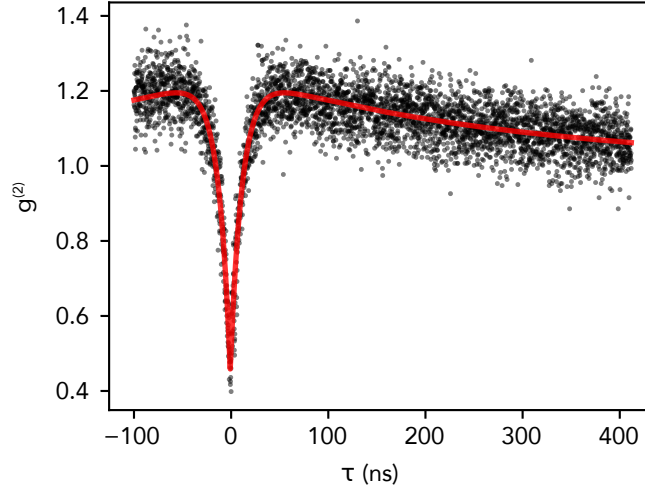B slightly. This will, however, make the measurement slower.

Figure 2.5: An ambiguous $g^{(2)}$ correlation measurement. The $g^{(2)}$ correlation from a diamond pillar is measured with the setup shown in Fig. 2.4. The minimum value dips below 0.5, but there are two NVs in this pillar with different fluorescence detection rates.

The $g^{(2)}$ correlation measurement is useful for determining whether or not a diamond probe contains a single NV, but some care is required in interpreting the measurement results from optical nanostructures, like the diamond pillars used in our scanning probes. In these structures, the NV fluorescence rates and detection efficiencies depend strongly on the lateral position of the NV within the pillar. This means that it is possible to measure values $g^2 < 0.5$ even for pillars containing multiple NVs. The correlation function for two single-photon emitters with uncorrelated, differing fluorescence collection/detection probabilities P_1 and P_2, is given by [18]

$$g^{(2)}(\tau) = g^{(2)}(0) + (1 - g^{(2)}(0))g_0^{(2)}(\tau) \tag{2.7}$$

15

where $g_0^{(2)}(\tau)$ is single-NV correlation function and

$$g^{(2)}(0) = \frac{2\frac{P_1(B_t)}{P_2(B_t)}}{\left(\frac{P_1(B_t)}{P_2(B_t)} + 1\right)^2} \tag{2.8}$$

An example of this measurement for a pillar containing two NVs is shown in Fig. 2.5, which gives $g^{(2)} \approx 0.44$. For magnetometry applications, the acceptable level $g^{(2)}$ for use as a single-NV probe is set by the practical consideration that we would like our magnetic signal to be dominated by a single NV. In practice, the first step in determining the number of NVs in a probe is to split resonance lines of the four NV orientations by different amounts using a magnetic field with different projections along each NV axis. Depending on the application, probes with multiple NVs of different orientations can still be used, as long as the ESR lines for the different orientations can be separated throughout the imaging measurement, but these probes will suffer from decreased spin state contrast due to the fluorescence from the off-resonant NVs. The $g^{(2)}$ measurement can then confirm whether the fluorescent signal of these remaining single-splitting probes is dominated by a single NV. In other NV measurements, for example those probing the charge state dynamics of single NVs, the presence of secondary NVs with very low collection rates can be detected by looking at the distribution of photons detected in a read-out measurement sensitive to the NV charge state [18].

2.2   NV sensing

The general idea of using solid-state spin defects for scanning magnetometry [19] was proposed in 1996 a year before the first demonstration of an ODMR measurement from a single NV center [3]. A decade later, a similar idea was proposed, this time specific to fluorescent spins or nanoparticles with ODMR signals [20]. But it wasn't until a few

years later, in 2008, that detailed proposals for using NV centers for high spatial resolution magnetometry were put forward [21, 22]. Around the same time, there was the first experimental demonstration of scanning NV magnetometry (in which a magnetic tip was scanned over a single NV center in bulk diamond [23]). Since then, there has been an explosion of papers related to NV sensing, both theoretical and experimental. These include techniques that have been (or will likely prove to be) practical for imaging or localized measurements or electric and magnetic noise [24,25,25–34] and more sophisticated techniques often aimed at nanoscale nuclear or single electron spin magnetic resonance imaging (MRI) [35–41]. There has also been a parallel development of ensemble NV sensing, where samples are packed with as many NVs as possible, while attempting to minimize inhomogeneous broadening [42–44]. Better magnetic field sensitivities can be achieved in ensembles, at the sacrifice of some spatial resolution.

2.2.1 CWESR

The simplest methods of sensing magnetic fields with an NV are based on continuous wave measurements of the ESR spectrum (CWESR), like that shown in Fig. 2.2. In these measurements, the NV is continuously illuminated with green light and microwaves. The relative power of the light and microwaves is adjusted depending on the sensing application. In this thesis I will break the applications up into two groups— sensing low fields from sources like currents flowing in graphene (µT-scale), or high fields from sources like ferromagnets (mT-scale). The classification of low vs. high in an NV sensing measurement is determined by the dynamic range of the NV CWESR measurement, which is roughly the linewidth of the NV ESR transition. This linewidth is limited by the coherence time T_2^*, but is also typically broadened by the driving optical and microwave fields. The linewidth of an NV spin state transition can be determined from the two-level

17

Bloch equations, where the light-induced polarization and dephasing processes are each treated with a relaxation term, and it is assumed that the optical power is not very small ($> 1\%$ of the saturation power), [24]

$$\Delta\nu = \frac{\Gamma_c^\infty}{2\pi}\sqrt{\left(\frac{s}{s+1}\right)^2 + \frac{\Omega_R^2}{\Gamma_p^\infty \Gamma_c^\infty}} \tag{2.9}$$

where Γ_c^∞ is high power limit of light-induced dephasing (on order of the NV excited state lifetime), Γ_p^∞ is the high power limit of optical spin polarization (a few hundred ns), Ω_R is the microwave Rabi rate, and s is the optical saturation parameter ($\Gamma_p = \Gamma_p^\infty s/(s+1)$).

2.2.2 Low-field sensing

In the low-field sensing case, it is often favorable to operate at low enough microwave and optical powers so that the hyperfine transitions are resolvable. The best magnetic sensitivity is achieved when the microwave frequency is parked on the steepest part of the resonance line. For a Lorenztian line-shape, like that describing a power-broadened resonance, the positions of maximum slope are at

$$f_m = \pm\frac{\Delta\nu}{2\sqrt{3}} \tag{2.10}$$

The slope of the resonance line at these positions, in terms of the NV $|m_s = 0\rangle$ fluorescence rate I_0, $|m_s = \pm\rangle$, fluorescence rate $I_\pm$, and frequency f, is given by the mixed spin state fluorescence rate $I_c = I_0(1 - 3\alpha/4)$ for spin state contrast $\alpha = (I_0 - I_\pm)/I_0$,

$$\frac{dI}{df} = \frac{3\sqrt{3}}{4}\frac{I_c\alpha}{\Delta\nu} \tag{2.11}$$

In the well-resolved-hyperfine case, assuming a shot-noise limited measurement, this would translate into a magnetic field sensitivity,

$$\eta_{cw} = \frac{4}{3\sqrt{3}} \frac{2\pi}{\gamma} \frac{\Delta\nu}{\alpha\sqrt{I_c}} \tag{2.12}$$

When the optical and microwave powers are increased the situation gets more complicated and the overlapping hyperfine lines begin to effectively increase the contrast, but the overlap also smears out the steep resonance slopes. For the NVs in our scanning probes, it is often possible to achieve $\eta_{cw} \sim 2\,\mu\mathrm{T}/\sqrt{\mathrm{Hz}}$.

The measurement described above, with a microwave frequency fixed to the side of the NV resonance converts a change in magnetic field along the NV axis into a change in the NV fluorescence, which gives a change in the photon collection rate of our confocal microscope. However, there are many other reasons that this collection rate can change during a scan:

- The NV transition width depends on the NV position relative to sample features, like magnetic domain walls

- The NV photoluminescence rate (PL) is sensitive to the NV-sample separation, sample material, NV charge state, or large perpendicular magnetic fields

- The background PL rate can depend on sample position

- The green laser power can fluctuate

- The focus of the green laser will drift over time

- The NV contrast can change due to changes in the charge state balance, or changes in the microwave field as the NV is moved relative to the sample or microwave wire

   Since these changes in the NV PL can be large compared to the changes in the NV PL due to the magnetic field from low-field samples, any measurement of the magnetic field should be immune to these non-B_{NV} changes in the NV ESR signal. To avoid these issues, we use square wave frequency modulation to alternately drive an NV transition on either side of the resonance, at the frequency positions where the sensitivity is highest. The PL detection is locked to the frequency modulation, similar to the method demonstrated in [26]. The mid-point of the frequency modulation square wave is swept over a linear region of this modulated frequency signal and the x-intercept of a linear fit to the resulting demodulated signal gives the best estimate of the transition frequency. This measurement is diagrammed in Fig. 2.6. For ^{14}N, the best modulation amplitude is roughly $2|A^{||}_{gs}| + \Delta\nu/\sqrt{3}$. The sensitivity of this measurement can be optimized by computing the frequency error using the linear regression of the measurement as diagrammed in Fig. 2.6.
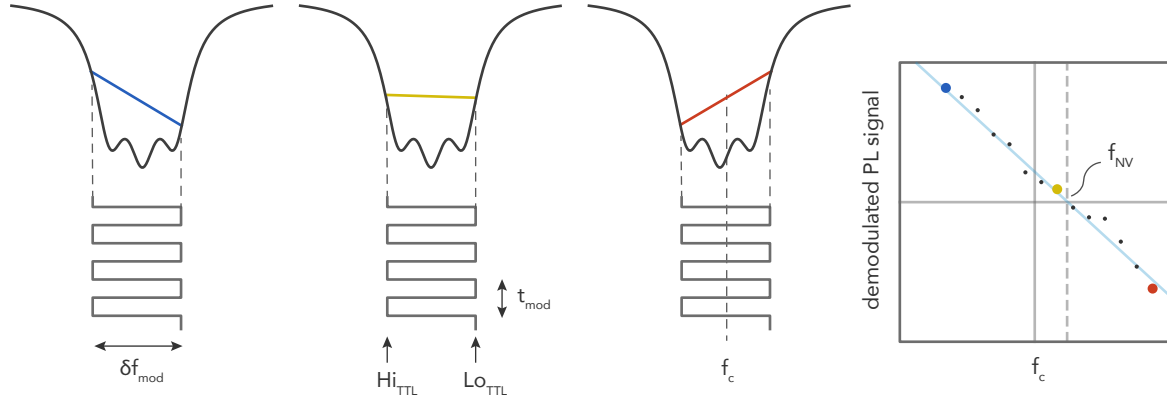
Figure 2.6: NV frequency modulation lock-in measurement. The microwave drive frequency is square-wave modulated to either side of an NV transition. A TTL square-wave controlling the modulation is routed to the NV signal counter and sets the counter direction up (down) for TTL high (low). For the 5 kHz modulation typically used, the TTL demodulation is in phase with the frequency modulation. When the midpoint of the modulation frequencies f_c is below (above) the center of the NV resonance, the demodulated signal is positive (negative). The transition frequency is measured by sweeping f_c in a small range over which the demodulated signal remains linear and extracting the x-axis intercept. When demodulated signal is zero, f_c matches the NV resonance, assuming a symmetric NV hyperfine.

2.2.3 High-field sensing

The other relevant sensing regime is for samples that produce large magnetic fields (compared to the dynamic range $\gamma \Delta \nu$). In this thesis, this regime applies to the magnetic skyrmion samples examined in Chapter 4. In these materials, the stray fields produced near sharply varying magnetization patterns can be quite large, many tens of Gauss for the materials and NV heights in our work. For sensing high fields, the required measurement time to reach a given signal-to-noise ratio (SNR) is limited not by the slope of the resonance, as above, but by the dynamic range of the NV ESR lines, or equivalently by the total depth of the NV resonance. While the resonance slope and the amplitude are related, they do not correspond to exactly the same thing, and the difference implies a different measurement strategy. In the high-field case, it is favorable to crank up the optical and microwave excitation to maximize the amplitude of the NV

resonance, while sacrificing the narrow transition widths to power broadening. This will increase the resonance amplitude up until the point that the NV orbital transition is saturated, at which point the contrast will begin to decrease.

For stray fields of tens of Gauss, the frequency shifts of the NV are on the order of 100 MHz or above, much larger than the typical, hyperfine and power broadened NV lines of several MHz, and it is possible to achieve high SNRs just by locating the ESR transitions above the PL noise floor. In this case, still assuming a shot-noise limited measurement, the fixed-frequency SNR for measurement time T_m is given by

$$SNR = \alpha \sqrt{I_c T_m} \tag{2.13}$$

This SNR applies to the case of a fixed frequency, or contour measurement, where an NV is scanned over a sample surface while the NV fluorescence, or photoluminescence (PL), rate is measured for a given microwave frequency. The resulting image is a *field contour image* with dark contours in the image corresponding to particular values of the stray magnetic field emanating from the sample that brings either one of the NV spin transitions into resonance with the applied microwaves. For an NV PL rate of 300 kcnts/sec and a contrast of 0.1, the minimum measurement time to acquire a pixel with an SNR of 10, is about 30 ms. For a 100x100 pixel image, this would yield an SNR = 10 image in about 5 minutes, ignoring any scanning or measurement overhead. The total measurement time for a contour scan is usually around tens of minutes for a 100x100 pixel image including scanning overhead and using a PL referenced measurement— often we take referenced microwave on/off-type measurements to avoid artifacts due to changes in the fluorescence background, caused by position-dependent variations in sample fluorescence, variations in laser intensity, or drift in the optical path. An example of a contour image is shown in Fig. 2.7a, where the microwave frequency is chosen so that the dark contours

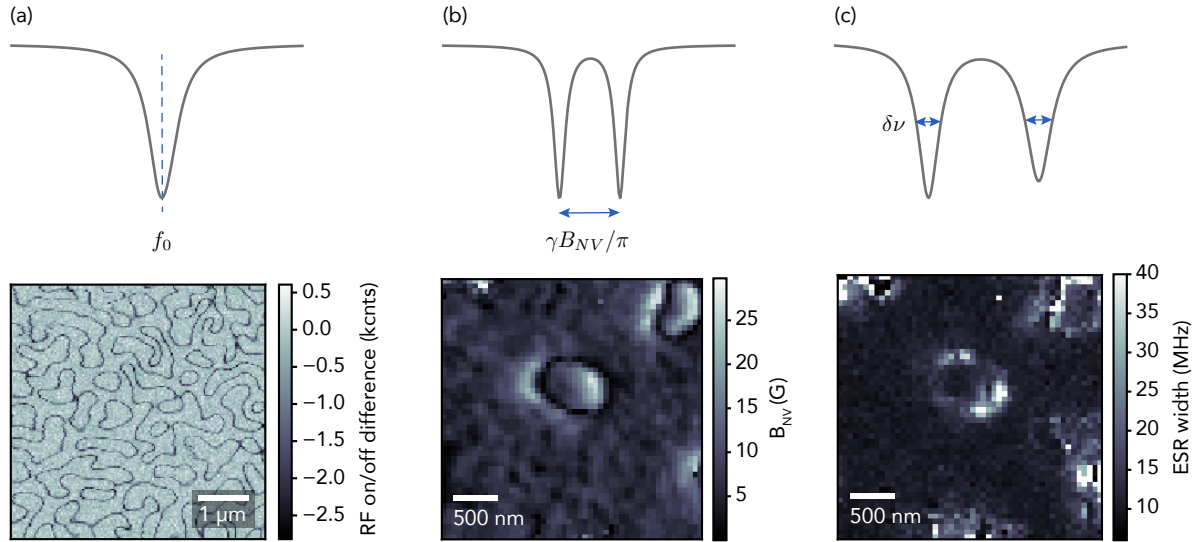roughly mark the locations of domain walls in a thin film structure Pt/Co/MgO.

Figure 2.7: High-field sensing methods. (a) Contour imaging of domain walls in a thin film magnetic heterostructure (Pt/Co/MgO). The microwave frequency is fixed to the NV zero-field splitting of 2870 MHz so that dark contours in the image correspond to locations where the magnetic field along the NV axis is zero. For this sample, these zero-field contours approximately mark the locations of the domain walls. (b) Full-field image of a bubble skyrmion in another thin film structure (Ta/CoFeB/MgO). The CWESR spectrum is measured at each point of the scan and the field B_{NV} is extracted. (c) Plotting the ESR widths from the full-field scan (b) highlights areas with increased magnetic noise. In this material, domain wall fluctuations give rise to increased ESR linewidths in the vicinity of the domain walls.

Depending on the application, it may be desirable to get more information about the stray field than a single field contour can supply. For example, a measurement of the magnetic field along the NV axis in the imaging plane can sometimes be used to reconstruct the full vector magnetic field, or make fairly quantitative predictions about the underlying magnetic or electric system that is producing the stray field, Appendix E. In order to measure the "full-field" information for high magnetic field samples, we need to locate the ESR transitions within the large frequency range spanned by the lines throughout the scan. There are many ways to do this. The most naive method, which also seems to be the most robust, is just to take a CWESR measurement like that shown

in Fig. 2.2 at each point in the scan, with large enough frequency point spacing so that there are a few measurement points within each resonance line. An NV image taken in this way is shown in Fig. 2.7b. For ESR lines that move over a range ±100 MHz and a frequency spacing of 1 MHz, the required scan time can increase by a factor of 100 over the contour scan described above, and even a 50x50 pixel image can take several hours. Some strategies to reduce the scan time, but still record full-field information include locking the microwave frequency to the NV transition or sweeping over smaller frequency ranges centered on each transition, and then updating the center of the sweep range as the tip moves relative to the sample. In both of these methods, some error-catching protocols are need so that if the frequency becomes unlocked, or a transition jumps out of the sweep range between pixel points, the scanning software will know and re-lock or adjust the sweep range appropriately. Other than robustness, the naive CWESR sweep method has the added benefit of containing more information than just the center positions of the NV resonances. The resulting spectrums of CWESR measurements can be used to simultaneously image both stray fields and magnetic noise fluctuations. An example of this is shown in Fig. 2.7c, where broadening in the NV lines indicates fluctuations of magnetic domain walls. These CWESR measurements also reveal multiple NV splittings at some locations, caused by the hopping of domain walls between bistable positions (see chapter 4).

2.2.4   Extracting magnetic field from NV transitions

As mentioned in section 2.1.1, we typically measure the frequencies of the NV ground state spin transitions and want to convert these frequencies into the magnetic field at the NV position. To first order, the magnetic field along the NV axis is just given by the Zeeman splitting between the $|m_s = \pm 1\rangle$ spin states, $B_{NV} \approx \pi \Delta f / \gamma$. But assuming

the effects of strain and external electric fields are small, the NV ground state is well represented by Eqn. 2.2, and we can solve for the magnetic field using the measured NV transitions, *including* the effects of perpendicular magnetic field [34]. Without loss of generality, assume the perpendicular magnetic field is oriented along the x axis. Then the characteristic equation for the Hamiltonian in Eqn. 2.2 becomes

$$-\lambda \left[(D - \lambda)^2 - \left(\frac{\gamma}{2\pi} \right)^2 B_z^2 \right] + \left(\frac{\gamma}{2\pi} \right)^2 B_\perp^2 (D - \lambda) = 0 \qquad (2.14)$$

and we have three independent equations in terms of the three eigenvalues $\lambda_{0,1,2}$. Defining transition frequencies, $\lambda_1 = \lambda_0 + \Delta f_1$ and $\lambda_2 = \lambda_0 + \Delta f_2$, we can combine the three characteristic equations and find quadratic equations for the three parameters λ_0, B_z, and $B_\perp$ in terms of Δf_1 and Δf_2. This gives $\lambda_0 = (2D - \Delta f_1 - \Delta f_2)/3$, and knowing Δf_1 and Δf_2, we can calculate the magnitude of the magnetic field components parallel and perpendicular to the NV axis,

$$|B_z| = \frac{2\pi}{3\gamma\sqrt{3D}} \sqrt{-(D + \Delta f_1 + \Delta f_2)(D + \Delta f_1 - 2\Delta f_2)(D - 2\Delta f_1 + \Delta f_2)} \qquad (2.15)$$

$$B_\perp = \frac{2\pi}{3\gamma\sqrt{3D}} \sqrt{-(2D - \Delta f_1 - \Delta f_2)(2D - \Delta f_1 + 2\Delta f_2)(2D + 2\Delta f_1 - \Delta f_2)} \qquad (2.16)$$

Note that $(\Delta f_1 + \Delta f_2)/2 \geq D$ giving a real $B_\perp$, because perpendicular fields will shift the mean transition frequency higher as described in section 2.1.1. At small external fields, this mean shift due to perpendicular fields will be small and extracting small $B_\perp$ from the transition frequencies is difficult, especially if D is not well known. Thankfully, we can do a lot with a spatial map of B_z alone.

2.2.5   Pulsed and AC magnetometry

The CWESR measurements described above are simple and using them in conjunction with a cryogenic scanning microscope already opens up an overwhelming number of materials systems for study. But there are a number of ways to extend NV sensing that may be useful in future scanning NV magnetometry experiments. In this section, I will briefly describe some of these techniques, and connect them to experiments that may be useful for the materials systems discussed in Chapters 4 and 5.

Pulsed measurements can be broken into DC and AC sensing categories. Pulsed DC measurements include pulsed ESR and Ramsey sequences (see Fig. 2.8). The sensitivity of these measurements is ultimately still limited by the T_2^* coherence time of the NV. Nevertheless, better sensitivity can be achieved with pulsed measurements over the CW methods because the spin contrast can be disentangled from the optical/microwave power ratio, and the ESR linewidth can be separated from the optical read-out power. The best sensitivity for a pulsed ESR measurement (left side of Fig. 2.8) is achieved for low microwave powers and long π pulses such that the resonance is not broadened significantly by the microwaves, but not so long that that the spin contrast starts to decrease [24]. A nice balance is reached for $T_\pi \sim T_2^*$.

The Ramsey sequence, shown on the right side of Fig. 2.8, consists of optical initialization to the $|m_s = 0\rangle$ state, followed by a short $\pi/2$ pulse that produces a superposition of $|m_s = 0\rangle$ and $|m_s = \pm 1\rangle$ (either one). The superposition then evolves for the free precession time T_p with neither microwaves or optical illumination, after which another short $\pi/2$ pulse converts the accumulated phase to a population difference. The population difference is read-out optically. Since both the optical and microwave excitations are separated from the field-sensing time in this sequence, the linewidth is given by the T_2^* dephasing time. This means that a Ramsey measurement will give better magnetic field

sensitivity than the CW measurements described above. On the other hand, the Ramsey sequence is less robust than CW measurements because the Ramsey signal depends critically on the NV contrast and Rabi time, both of which will typically varying throughout a scan. There are also proposals and initial demonstrations of extending the NV DC magnetometry sensitivity to the T_2 limit, but these require jumping through technical hoops, like rotating the NV sample at 20 krpm [45] or operating near the ground state level anti-crossing with $B_{NV} \sim 1000$ G [46] that are not practical for general measurements in our scanning NV system.

The more promising way to push the NV's sensitivity to the T_2 limit is to use it to detect AC signals. This can be a signal that's naturally oscillating, at frequencies $> \Gamma_2 = 1/T_2$. For example, NV AC magnetometry can be used to probe the magnetic noise spectrum in the tens of kHz to MHz range, set by the maximum achievable T_2 times and minimum achievable Rabi times. Alternatively, the signal of interest can be promoted to AC. This is especially easy when measuring the stray magnetic fields produced by current sources, if an AC current can be driven at tens of kHz and the underlying electron dynamics are at much higher frequency scales. Another way to produce an AC magnetic signal from a DC source would be to oscillate the NV position at frequencies $> \Gamma_2$. This is similar to the idea of rapidly rotating an ensemble sample, but is a natural extension to a scanning NV measurement with the NV probe attached to an oscillating tuning fork. This sensing scheme is best for samples that produce large field gradients, such as magnetic samples with small feature sizes.

Figure 2.9 shows examples of AC measurements. The simplest AC pulse sequence is the Hahn echo measurement, shown on the left. This sequence is similar to the Ramsey sequence, except that the free precession time is broken in two by a π pulse. Phase that is accumulated by magnetic fields that are fluctuating at frequencies well below $1/2\tau$ in the first half of the sequence will be canceled out in the second half, when the post-π-pulse

NV accumulates phase in the opposite direction for a given magnetic field sign. Below the pulse sequence in Fig. 2.9(a), a schematic of an NV coherence measurement is shown for an NV in a natural ^{13}C environment and an external magnetic field of tens of G. The collapses and revivals of NV coherence are caused by the precession time aligning with multiples of the spin-1/2 ^{13}C precession time in the external field.

In the case where the signal of interest has been promoted to AC as described above, one benefit of an AC measurement is that the NV AC sensitivity is higher than its DC sensitivity because $T_2 > T_2^*$ generally. The AC sensitivity is [22]

$$\eta_{AC} \approx \frac{\pi}{2} \frac{1}{\gamma} \frac{1}{C\sqrt{T_2}} \tag{2.17}$$

where T_2 is the Hahn echo coherence time and C is a parameter that includes the photon collection efficiency, spin projection, and photon shot noise. The noise in our measurements, with a green laser used for spin state read-out, is dominated by photon shot noise and in this case the prefactor looks like

$$\frac{1}{C} = e^{1/2} \frac{\sqrt{4(2-\alpha)}}{\alpha} \frac{1}{\sqrt{I_0 t_r}} \tag{2.18}$$

for spin state optical contrast α, $|m_s = 0\rangle$ state fluorescence rate I_0, and single measurement read-out time t_r, assuming an in-phase square wave signal. Plugging in typical values for our grade AA NV probes ($I_0 = 300$ kcnts/s, $\alpha = 0.2$, $T_2 = 50$ μs, $t_r = 400$ ns), we get Hahn echo sensitivities of ~ 100 nT/$\sqrt{\text{Hz}}$, about a factor of 10-20X better than our DC sensitivities.

There has been a lot of work to develop more complicated pulsed measurements that fall under the umbrella of *dynamical decoupling* sequences. A general example of these is shown on the right side of Fig. 2.9. They include $2N$, usually equally-spaced, π pulses,

with particular variations in pulse phases relative to the initial $\pi/2$ pulse. For example, the CPMG-N sequences have x-$\pi/2$ pulses and y-π pulses. The sequences are useful for extending T_2 coherence times beyond those measured with Hahn echo. As the number of π pulses increases, for a fixed total sequence time T, the NV becomes less sensitive to magnetic noise at lower frequencies. The effect of these sequences can be described by their frequency space filter functions $\mathcal{F}(T, \omega)$. For a magnetic noise spectrum $\tilde{S}(\omega)$, the NV coherence under an ideal dynamical decoupling sequence is [47, 48]

$$C(T) = \exp\left(-\int d\omega \tilde{S}(\omega)\mathcal{F}(T, \omega)\right) \tag{2.19}$$

An example of a filter function with $N = 16$ and $T = 50\,\mu s$ is shown in Fig. 2.9 below the dynamical decoupling schematic. Looking at this filter function, it is clear that the power of dynamical decoupling sequences for sensing applications is in their ability to probe narrow windows of the magnetic noise spectrum at a frequency set by the π pulse spacing. This gives a method for measuring the local magnetic noise spectrum, in which the NV coherence is measured for varying τ times and pulse numbers N. In some cases the noise spectrum can be deconvolved from these measurements [48, 49]. This type of magnetic noise spectroscopy may prove useful for studying magnetic dynamics such as those described in Chapter 4.
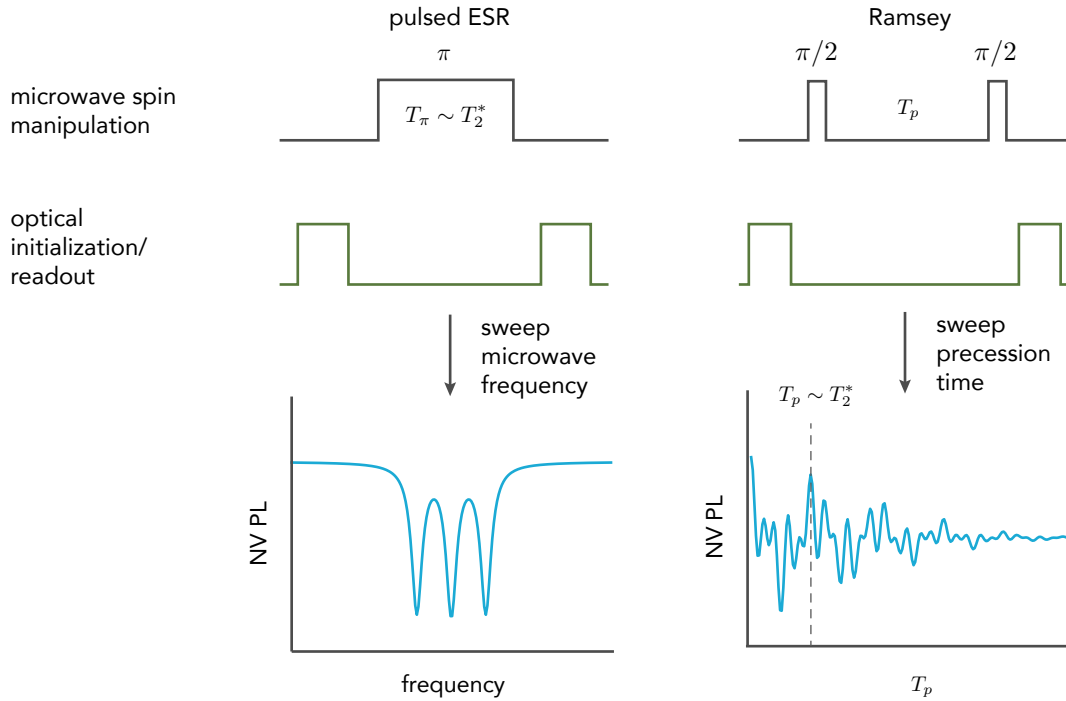
Figure 2.8: Pulsed DC measurements of a magnetic field. In a pulsed ESR sequence, the NV is initialized to the $|m_s = 0\rangle$ state with green light, the light is turned off, a long π microwave pulse is applied, and finally the NV spin state is read out optically. In this way, the NV ESR spectrum can be obtained if the measurement is repeated many times as the microwave frequency is swept over the NV resonance. In a Ramsey sequence, precession of the phase of a superposition of spin states is used to measure the magnetic field. In this measurement, the NV is initialized with green light, and then placed in a superposition of $|m_s = 0\rangle$ and either $|m_s = \pm1\rangle$ with a short $\pi/2$ pulse. The accumulated phase between the spin states is proportional to the magnetic field along the NV axis and the free precession time T_p. A second $\pi/2$ pulse converts the accumulated phase into a population difference and the spin state population difference is read-out optically.
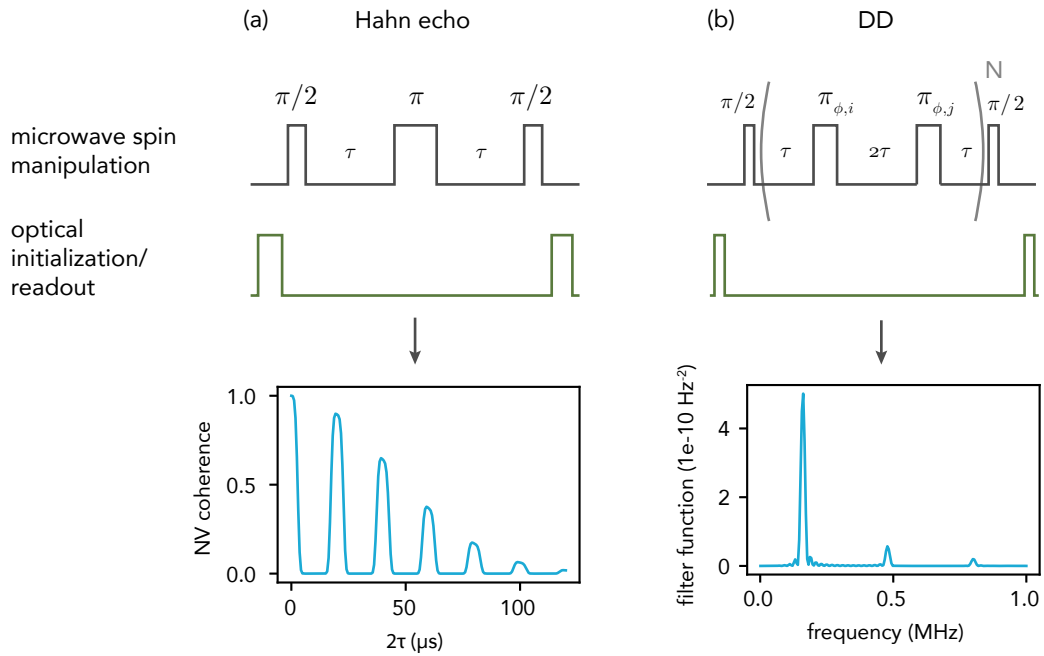
Figure 2.9: AC magnetometry. The Hahn echo sequence consists of two free precession periods, split by a π pulse. Phases accumulated during the first free precession time τ due to low frequency magnetic noise are canceled in the second free precession time. The microwave sequence is sandwiched between optical initialization and read-out. The expected Hahn echo signal for an NV in a diamond with natural ^{13}C abundance is shown below the sequence. Dynamical decoupling (DD) sequences such as CPMG, XY4, or XY8 have the structure shown on the right. These sequences have $2N$ π pulses, with particular combinations of pulse phases. These sequences can be represented by filter functions in frequency space, an example of which is shown on the lower right.

The magnetic noise environment of the NV can also be probed using the NV relaxation time [31, 50, 51]. The most straight-forward way to do this is to optically initialize the NV, turn off the green light for a *dark time* τ, and then turn it back on to read-out the spin state. But this method is sensitive to charge-state dynamics, which can depend on τ, confusing the resulting measurement of the T_1 decay. A better method involves separately measuring the PL change starting from alternating initialization into the $|m_s = 0\rangle$ and $|m_s = 1\rangle$ states and then taking the difference. The NV spin relaxation between $|m_s = 0\rangle$ and the $|m_s = \pm 1\rangle$ states is sensitive to magnetic fields perpendicular to the NV axis at the frequencies of the spin state splittings. These splittings can be tuned with an external magnetic field in order to probe the noise at different frequencies.

T_1 measurements may also be good probes of NV height z_{NV} above non-magnetic metallic samples, and measuring T_1 vs. z_{NV} may be a useful method for calibrating the NV scan height. The height dependence of the NV relaxation rate $\Gamma_1 = 1/T_1$ above a non-magnetic, metallic sample of thickness t, conductivity σ, at temperature T, is expected to go like [51]

$$\Gamma_1 \propto \sigma T \left(\frac{1}{z_{NV}} - \frac{1}{z_{NV} + t} \right) \qquad (2.20)$$

in the ohmic regime, where the momentum relaxing mean-free-path $l_{mr} \ll z_{NV}$ (see Chapter 5 for a discussion of ohmic conductors and l_{mr}). As we will see in Chapters 4 and 5, knowing the NV height is critical for making quantitative predictions about the materials system under study, and this height is often difficult to calibrate. Along with the $m = 1$ relaxation processes, relaxation between $|m_s = 1\rangle$ and $|m_s = -1\rangle$ can also be measured, and this relaxation is sensitive to the electric field noise in the NV environment [29].

The simple expression of NV relaxation rate Γ_1 above a metal given above is altered when probing the magnetic noise from different electronic regimes like ballistic or hydro-

dynamic. For example, above a 2D material this relaxation rate is given more generally by [27]

$$\Gamma_1 \propto \frac{\sigma^T(q = 1/2z_{NV}, \omega)T}{z_{NV}^2} \tag{2.21}$$

where $\sigma^T(q)$ is the transverse conductivity at wavenumber q. The longitudinal and transverse conductivities are related to the conductivity tensor $\sigma_{\mu\nu}(\boldsymbol{q}, \omega)$ through the longitudinal and transverse projection operators $P_{\mu\nu}^L$ and $P_{\mu\nu}^T$

$$\sigma(\boldsymbol{q}, \omega) = P_{\mu\nu}^L \sigma^L(\boldsymbol{q}, \omega) + P_{\mu\nu}^T \sigma^T(\boldsymbol{q}, \omega) = \frac{q_\mu q_\nu}{q^2}\sigma^L(\boldsymbol{q}, \omega) + \left(\delta_{\mu\nu} - \frac{q_\mu q_\nu}{q^2}\right)\sigma^T(\boldsymbol{q}, \omega) \quad (2.22)$$

The transverse conductivity can be probed by measuring the NV relaxation rate as a function of z_{NV} and this conductivity in turn yields information about electronic correlations in the material: the wavenumber dependence for the ohmic, ballistic, and hydrodynamic regimes of a 2D material are expected be $\sigma^T \sim$ const., $1/q, 1/q^2$ respectively [27].

The NV relaxation rate can also be used to probe dynamics in magnetic samples. The relaxation measurement is particularly useful for probing magnetic insulators, where the noise signal due to magnetization dynamics is separated from the current-induced noise described above. In these systems, measurements of NV relaxation times can be used to probe the magnon chemical potential [52], as well as spin transport coefficients like the spin diffusion length or spin relaxation time [53].

Altogether, several different measurement techniques can be used to probe magnetic noise over a very wide frequency range. Direct measurements of NV PL can probe magnetic dynamics up to a few kHz, ESR broadening or T_2^* measurements may be used to probe noise up to MHz frequencies, while dynamical decoupling sequences provide a more quantitative means of probing magnetic noise spectrum in the MHz range, and T_1 relaxometry can be used to probe frequencies in the MHz to GHz range.

2.3   Shallow NVs

A lot of the power of single NV sensors comes from their atomic size. The sensing volume of a single NV is ridiculously small, comprising the electronic orbitals described in section 2.1.4, spread over only a couple lattice sites. This means that a single NV can spatially resolve changes of the magnetic field at the atomic scale, just by moving the NV around and measuring its spin transitions at different points. Unfortunately, being able to measure a stray magnetic field with atomic resolution is not the same thing as being able to measure the underlying electronic or magnetic structure at this same atomic resolution. The magnetic field components with wavelength $\lambda = 2\pi/k$ die off exponentially away from sample surfaces like $\tilde{B}_i(k) \propto \exp(-kz)$ for height z above the sample. So even though the NV can measure variations in magnetic field with sub-nm resolution, structure within the samples cannot be probed with this resolution because the large-k components of stray fields will be too small to detect at the NV position if $kz_{NV} \gg 1$, even if the k-field component right at the sample surface is large. This exponential decay, set by the NV height z_{NV}, gives a practical imaging resolution of $\sim z_{NV}$ for most scanning NV applications. The resolution described here is relevant for real-space imaging. The resolution of other imaging techniques like coil-based MRI, depends partly on the magnitude of the magnetic field gradients, and the frequency resolution of an inductive pick-up coil. In that case, the imaging resolution is obviously not set by the sensor volume and sensor-sample separation.

It is clear then, that for scanning NV imaging, small NV-sample separations are crucial to high spatial resolution imaging. This means that it is desirable to have NVs that live extremely close to the diamond surface in order to take advantage of the NV's high resolution capabilities. Also, it is then necessary to have a diamond probe geometry that allows small separations between the diamond surface at the position of the NV
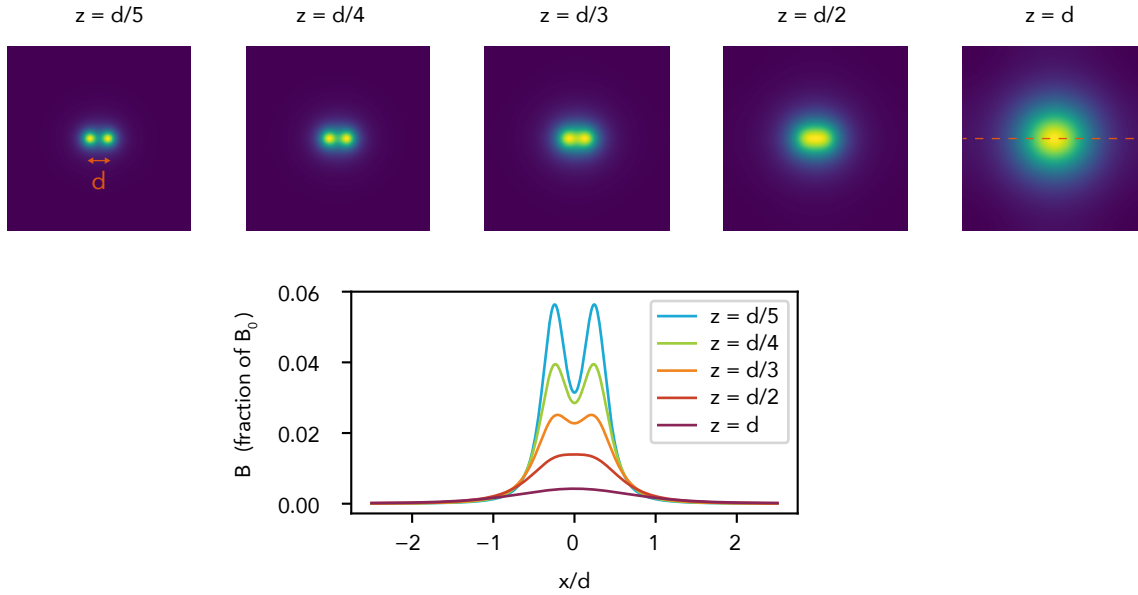
Figure 2.10: Imaging resolution as a function of scan height, demonstrated with a field pattern consisting of two gaussians separated by a distance d, for an arbitrary field component B_i. The gaussian widths at $z = 0$ are $0.1d$. The top row of images shows the field evolution as the imaging height is increased, with each color scale normalized independently. Below are linecuts through the center of the images, showing the decreasing field magnitude relative to the maximum B_0 at $z = 0$.

and the sample surface, as will be described in the next chapter. However, there is tradeoff between resolution and magnetic field sensitivity when using extremely shallow NVs, because their decoherence rates will typically increase the closer the NVs are to the diamond surface. We typically use NVs implanted at depths 10-30 nm below the diamond surface. We have found that 30 nm deep NVs are are less susceptible to surface-related changes in charge-state stability, which often show up with shallower NVs at cryogenic temperatures in our system.

2.3.1 Spin coherence and charge state stability of near-surface NVs

Shallow NVs (tens of nanometers from the diamond surface or shallower) are preferable for sensing with high spatial resolution, but as mentioned above, they often come with the downsides that they suffer decreased coherence times [30, 54, 55] and decreased charge state stability [56, 57]. The details of the diamond surface determine the coherence and charge state stability of shallow NVs. The coherence times of shallow NVs are degraded by magnetic and electric field noise due to paramagnetic surface spins or charge traps [30, 58], while the charge state behavior is affected by the diamond surface termination and the energy levels of electronic surface states [59–61]. The main two types of termination discussed and encountered in normal diamond processing are hydrogen termination and oxygen termination, which can come in various flavors like C-OH and C=O as well as the more desirable C-O-C. The surface can have mixtures of all these types of termination. The negative electron affinity of the hydrogen termination produces surface electric dipoles that point into the diamond. If water adsorbates are present on the surface, the Fermi level can be pinned to adsorbate levels, bending the conduction and valence bands upward at the surface. This can result in hole accumulation at the surface, and stabilization of NV^0 over NV^-. Another important surface feature is the presence of graphitic layers, produced in ion implantation or high temperature annealing. These graphitic layers can similarly lead to an instability of the NV^- charge state [61, 62].

These surface related problems are at least partially mitigated by uniformly terminating the diamond surface with a particular form of oxygen termination, in which the oxygen atoms are connected to the carbon atoms in bridge like C-O-C bonds [59]. Oxygen termination recipes have been empirically developed in a process by which new treatment procedures that are seen to improve the diamond surface favorably for shallow NVs are

added on to existing methods. This can involve multiple interleaved high temperature vacuum anneals, lower temperature oxygen anneals, and boiling acid treatments. For our probe fabrication, discussed in the next chapter, we haven't pushed these surface treatments to their full potential yet. After a high temperature anneal in vacuum or an inert Ar atmosphere at 850° C, we typically remove graphitic layers and oxygen terminate the diamond surface using a 1:1:1 boiling mixture of nitric, sulfuric, and perchloric acid, followed by an oxygen anneal for 2 hours at 450° C, prior to probe fabrication. After probe fabrication, the violently bubbling tri-acid clean becomes risky, and we stick to lower temperature nitric + sulfuric acid cleans, oxygen anneals, and oxygen ashing.

In the course of scanning or cooling the diamond probes to low temperature, we have seen that the NV contrast can decrease due to a modification of the surface caused by picking up junk from our samples or from condensation on our probes at low temperature in a leaky vacuum environment (likely due to changes in the charge state stability of the NV). These probes will show greatly reduced optical spin state contrast. The difficulty in handling these mounted probes and incompatibility of tuning-fork/glue materials make the acid or oxygen annealing surface treatments difficult for individual probes, but there is another oxygen treatment that we have found that can *bring these reduced contrast NVs back to life.* This oxygen treatment is done in a Gasonics Aura 2000 downstream oxygen asher. Early attempts to oxygen terminate diamond surfaces and control NV depths using oxygen plasmas found that direct exposure to oxygen plasmas damage shallow NVs, even tens of nanometers below the diamond surface (well below depth actually etched by the plasma), likely due to the plasma-induced creation of vacancies [63]. The downstream oxygen ashing treament on the other hand has reliably revived our probes without degradation of the original NV properties, for up to several minutes of ashing (we use a sample temperature of 100-150° C during the ashing). In the downstream system, the sample chamber is separated from the plasma, and the reactive oxygen ions

produced in the plasma chamber are pumped to the sample chamber. By the time the single oxygen atoms reach the sample they no longer have the high kinetic energies present in the plasma, but are still very chemically reactive. This downstream arrangement also separates the sample from the UV produced by the plasma.

Chapter 3

A cryogenic scanning NV microscope

NV sensors are well-known for their long coherence times, even at room temperature. So it may seem curious to take this excellent room-temperature sensor and add all the complications of cryogenics. In this Chapter, I will try to convince you that combining a confocal microscope and atomic force microscope (AFM) inside a cryostat is worth the effort: extending scanning NV magnetometry to cryogenic temperatures opens the technique for use probing a wide-range of condensed matter phenomena and provides improved AFM stability. I'll explain the microscope design and operation, and at the end, I'll discuss our initial demonstrations: using this system to image a magnetic hard disk drive and probe vortices in an iron pnictide superconductor.

3.1 Probing condensed matter order

A lot of initial excitement around NV sensors was related to their possible applications in biology. There were many proposals and initial demonstrations of nanoscale magnetic resonance imaging of biological molecules. This is an appealing application of NV sensing because of their high spatial resolution, operation under ambient conditions, non-invasiveness, and because of the biological inertness of diamond.

A parallel branch of NV sensing has been aimed at using NVs to probe magnetic and electronic phenomena in non-biological, hard condensed matter systems. In these systems, structures on the lengths scales accessible with scanning NV magnetometry (tens of nanometers) often emerge as long-range order out of collective short range interactions. These interactions often display nontrivial dependence on temperature, with particular patterns and order arising in particular temperature ranges. Hence, studying the temperature dependence of condensed matter phases gives us key information about the underlying interactions and in some cases allows us to disentangle the competing magnetic or electronic effects. Furthermore, the nature of the phase transitions themselves often contain information about the dominant phenomena.

For almost all applications of NV sensing demonstrated so far, there exist other technologies that can be used for similar purposes. Other techniques usually have differences in resolution, speed, and invasiveness that make NV sensing complimentary to existing techniques, but the NV is unique in its combination of magnetic and electric field sensitivity, high spatial resolution, non-invasiveness, and operation over a wide temperature range. For this reason, there are not many imaging tools applicable to the same breadth of condensed matter problems as NVs. Also, the importance of having complimentary methods for detecting the same phenomena should not be down-played. Even direct imaging of condensed matter systems can often give somewhat murky results that can be interpreted in different ways. Some examples of condensed matter systems where NV sensing has been or likely will be useful include, biomolecules, superconductors, topological insulators, multiferroics, ferromagnetic domain walls or other magnetic textures, current flow in graphene or other high-purity electronic systems [28, 33, 34, 41, 52, 64–70]. NV sensing has also been used as a probe of the dynamics of large ensembles of interacting spins, including densely packed NVs themselves [44, 71, 72].

As mentioned above, the tool described in this chapter has a few key features: it is
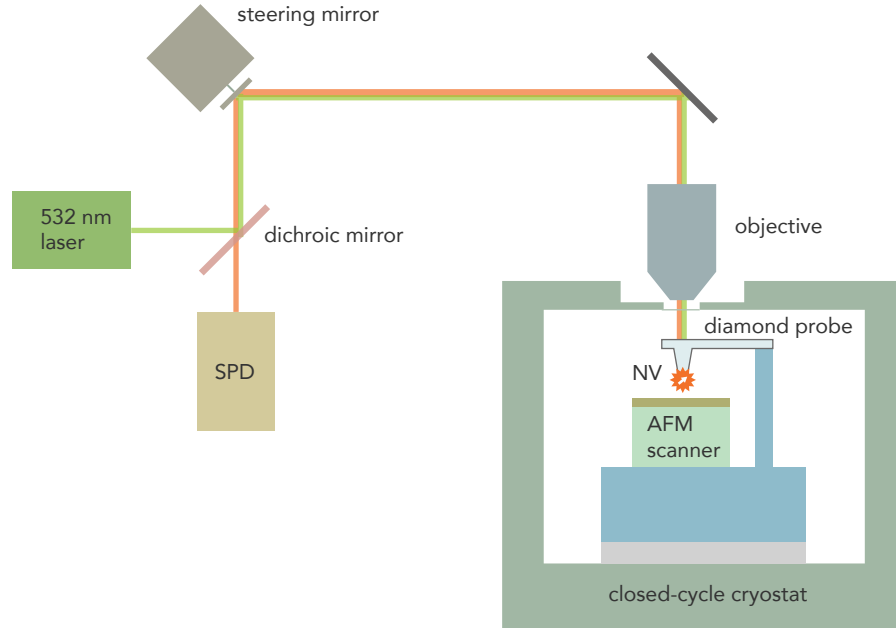
Figure 3.1: Overview of the cryogenic scanning NV system. A confocal microscope is made from a 532 nm excitation laser, a single photon detector, a microscope objective and a series of mirrors and lenses that focus the excitation light onto an NV and collect the red NV fluorescence. The excitation and collection paths are split by a dichroic mirror which transmits red light and reflects green light. Inside the closed-cycle cryostat, piezo steppers are used to coarsely align the probe and sample underneath the objective and coarsely align the sample underneath the probe. A piezo scanner is used for fine positioning for imaging.

a local probe, it is non-invasive to most systems, it has high-spatial resolution, operates over a wide-temperature range, is a quantitative probe of magnetic fields, and it has good magnetic field sensitivity. Local probes are important in cases where material variation and disorder are present. For example, Neutron scattering, a complimentary technique, is an excellent way to detect small scale magnetic order, but is limited to studying large single crystals or studying the average structures over a disordered material. Furthermore, having a local probe can be useful for studying the behavior of small electronic

or magnetic devices. Transport measurements can give bulk-type information about a device's behavior, but the measurements are an indirect probe of what it going on inside a sample. Thin-film skyrmion materials made from sputtered heterostructures are an excellent example of systems where local measurements are important. The sputtered films can contain a lot of disorder and the eventual goal is to make these systems into devices, where the ability to study the behavior of individual skyrmions will be important (see chapter 4).

Another important feature of the NV sensing is its relative simplicity compared to many complimentary techniques. Figure 3.1 shows a broad overview schematic of the scanning NV microscope. A confocal microscope is used to find and optically address NVs. The excitation beam is 532 nm light, focused onto single NVs inside a diamond probe using a microscope objective external to the closed-cycle cryostat. Inside the cyrostat, a series of positioners and a piezo scanner are used to arrange and scan the sample underneath the probe. Fluorescence from the NVs is collected with the same objective and follows the same optical path as the excitation light, back to a dichroic mirror that separates the excitation and collection paths. The fluorescence is fiber coupled and sent to the single photon detector.

The main difficulties in constructing a cryogenic scanning NV microscopes have been related to the integration of the main components (1) NV probes, (2) confocal microscope, (3) AFM, (4) closed-cycle cryostat. If the demand is there for a commercialized version of this system, it seems simple enough that it could be integrated into a standard AFM-type instrument. One down-side to this system that may hinder its adoption as a widespread material characterization tool is its slow imaging speed. The slow scan speeds currently make these systems well-suited to highly focused, long-term studies of a single, hard problem, but they have not yet become useful for the high-throughput characterization of many samples.

In the following sections, I will expand on the individual components of our scanning NV microscope.

3.2   NV probes

The main goal while making diamond probes for scanning magnetometry is to improve, or at least maintain, the sensing properties of the NVs as compared to NVs in bulk diamond, while making geometries that are conducive to high resolution imaging (shallow NVs placed at the ends of sharp tips). High-yield is also important, so that we get many useable probes for one round of lengthly fabrication (this favors making smaller probes). On the other hand, the probes should be easy to handle and mount (this favors making larger probes).

3.2.1   NV formation

We make our diamond probes out of CVD-grown, single crystal, electronic grade diamond from Element Six. These diamonds have properties that promote good NV sensitivity and uniformity— they have low strain, and low levels of dopants. The first step of the process is to create the NVs themselves. For many centuries, it was thought that NVs formed spontaneously in muddy puddles after rainstorms. We start with a $2 \times 2 \times 0.5$ mm plate of $\langle 100 \rangle$ diamond. To make our lives easier during diamond fabrication and mounting, we have the plate sliced and polished into thinner pieces. We send the plates to Applied Diamond for this process, where they extract and polish down three 20 µm thick pieces from one 500 µm plate. We further thin these 20 µm thick pieces to around 10 µm with a dry Ar/Cl etch, using the recipe described in Appendix A. This both removes sub-surface polishing damage and is useful because we ultimately want our diamond probes to be even thinner (< 5 microns) so they can be easily broken

off the larger diamond chip for mounting. The thinned diamonds are electrostatically bonded to clean Si pieces, simply by pressing down on them and nudging them around while they are immersed in acetone.

At this point the diamonds are sent to Innovion for nitrogen implantation. The nitrogen is implanted at a fixed energy, around 5-25 keV, depending on the desired NV depth, with a total implantation density around 3×10^{10} N/cm^2. The ions are implanted at 7° from the diamond plate normal in order to avoid channeling of the N ions through the diamond lattice. The implantation density is chosen so that we end up with about one NV per 400 nm diameter diamond pillar at the end of the fabrication. The final NV density depends on the conversion efficiency from nitrogen atoms to NVs. We have observed that this conversion efficiency depends on the depth of implantation, consistent with [73]. The conversion efficiency also depends on the length of the NV-forming high temperature anneal. This anneal is done at 850° C for 3-6 hours. Since diamond will begin to etch in an oxygen environment at temperatures around 500° C [63, 74], it is important that this high temperature anneal is performed in an inert atmosphere or under high vacuum. The number of functional NVs in a 400 nm circle on the diamond surface at this point in the process may not be the same as at the end of the process, as NVs near the sidewalls of the probe pillars will likely be damaged during the pillar etching step.
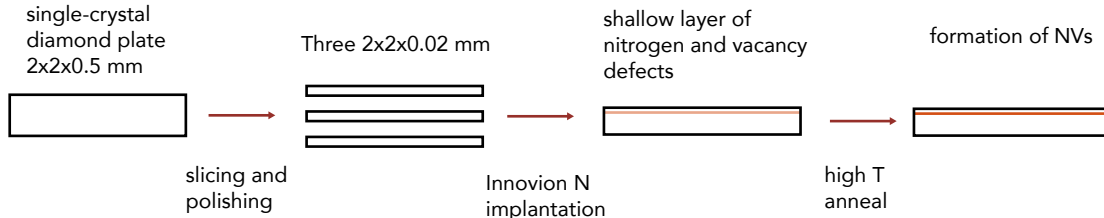
Figure 3.2: Making NVs via implantation.
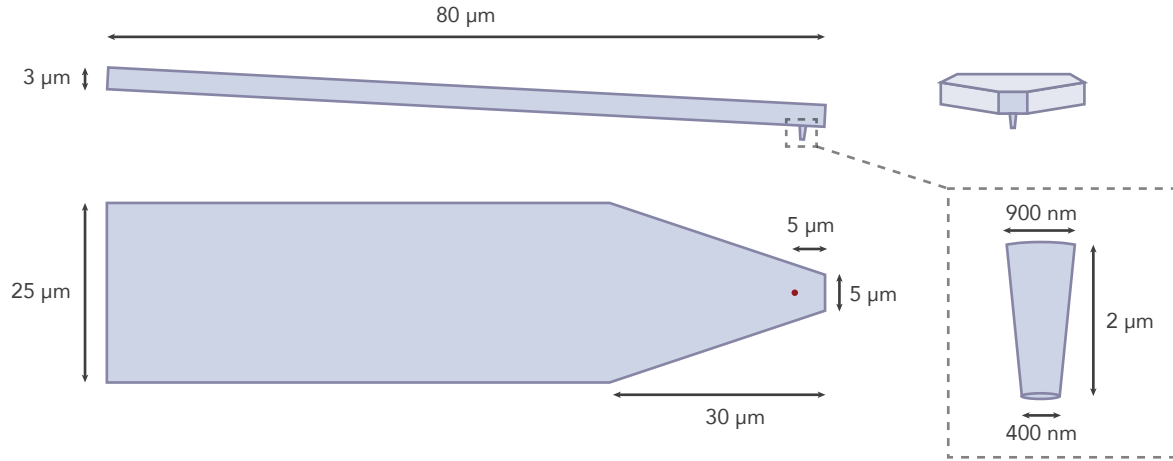
3.2.2 Probe fabrication

Figure 3.3: Rough geometry of a diamond probe.

Figure 3.3 shows the basic design of our diamond probes. As described above, the geometry is chosen based on a few competing considerations. The starting point for this design is that we want to be able to bring a shallow NV in the apex of a diamond pillar close to whatever sample we're looking at. This implies a tall pillar with a sharp tip, but the height and sharpness are constrained by two other factors. The pillar height is limited because not many good mask materials exist with large diamond/mask etch ratios for either the Ar/Cl or O_2 inductively coupled plasma (ICP) diamond etches. And the pillar end-diameters are limited by considerations of NV emission and collection, as well as the problem of NV degradation near etched surfaces. Due to the high index of refraction of diamond, the pillars have the added benefit of waveguiding light out of the backside of the probe and towards our collection objective. For our NA 0.7 microscope objective, this gives us a roughly 10X increase in collection efficiency of the NV fluorescence. But this waveguiding only works well if the pillar diameter is > 200 nm [75, 76]. The collection efficiency also depends on the sidewall angle of the pillars, and is maximized for a 20°-30° sidewall angle (see Fig. 3.4) combined with a tip diameter of 350-400 nm. It is possible

45

to control the sidewall angle somewhat during the ICP diamond etching step described below. Finally, the collection efficiency also depends strongly on the lateral location of the NV inside the pillar, it being largest if the NV is well-centered in the pillar [76].
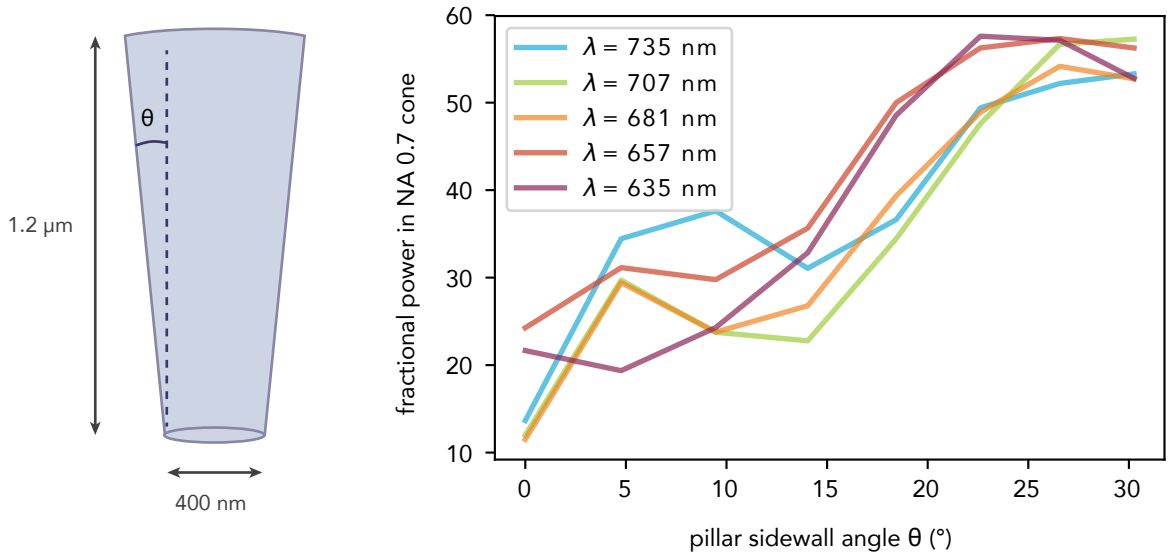

Figure 3.4: Fraction of radiated power in a 0.7 NA cone behind the cantilever (not shown at left) as a function of pillar sidewall angle (shown at left) and wavelength. The power fraction is calculated using Lumerical FDTD simulations of an electric dipole centered on the pillar axis, oriented at 35° relative to the pillar axis. The power fraction is calculated relative to the total emitted power and thus does not take changes in the local density of states into account.

The cantilever geometry is determined by practical considerations of handling and mounting the probes. We place the pillars at one end of an 80–100 micron long cantilever, far enough from the edge that the pillars can be safely positioned a few microns from the cantilever sides in a contact aligner, but not so far that there is any danger of the diamond cantilever contacting the sample before the pillar when the probe is tilted by a few degrees. We intentionally tilt the probes a few degrees towards the pillar end when mounting to ensure that the pillar contacts the sample before other parts of the diamond cantilever. The length and width are chosen to be large enough that we can glue a blunt pulled-glass piece (end broken at 25-50 micron diameter) to the diamond

cantilever, without covering up the collection cone of the objective when focusing on the pillar.

The main steps in the probe fabrication are shown in Figure 3.5. (1) The diamond plates are bonded to 280 micron thick silicon carrier wafers ($\sim$ 15x15 mm) using a spin-on glass known as hydrogen silsesquioxane (HSQ). A thin silicon piece and a plate of graphite are used to protect the NVs and to distribute the bonding pressure evenly over the entire carrier wafer. (2) The diamond pillars are defined using a thick (500-700 nm) HSQ mask pattern, written with e-beam lithography, and the diamond is etched in an inductively coupled plasma (ICP) tool with oxygen and argon ions. (3) The diamond cantilever support structures are defined with optical contact lithography and a Ti/Al etch mask. (4) Trenches are etched all the way through the Si carrier wafer to expose the cantilevers. (5) The cantilevers are released with a final diamond etch, if necessary, and the diamond surface is oxygen treated. Figure 3.6 shows SEM images of diamond cantilevers made with this fabrication process.
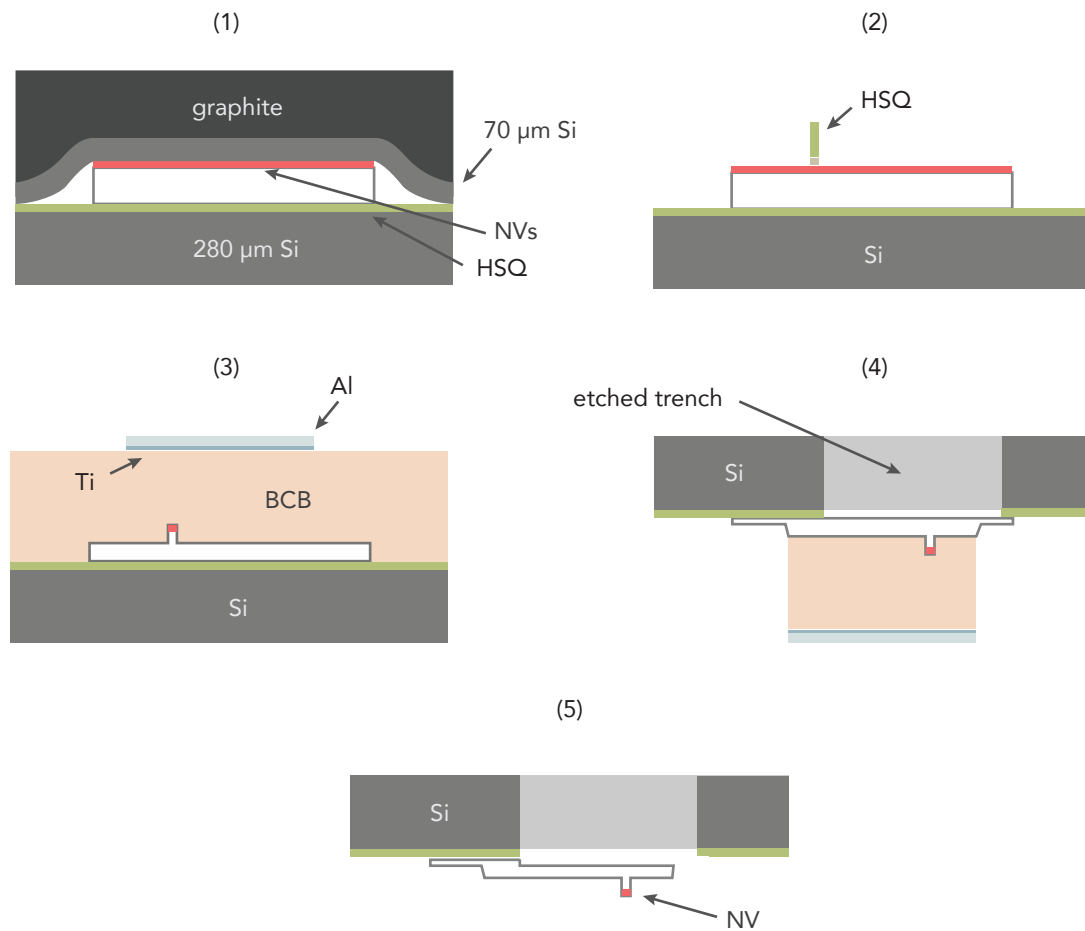
Figure 3.5: Main steps in the fabrication of the diamond probes. (1) A 10 micron diamond plate is bonded to a silicon carrier wafer with a spin-on glass. (2) E-beam lithography of an HSQ mask and O_2 plasma etching is used to shape diamond pillars. (3) The cantilevers are defined with optical contact lithography and a Ti/Al mask. (4) A deep silicon etch is used to make trenches all the way through the carrier wafer, exposing the diamond cantilevers so they can be mounted on a tuning fork. (5) Masks are removed and probes are acid cleaned and oxygen annealed.
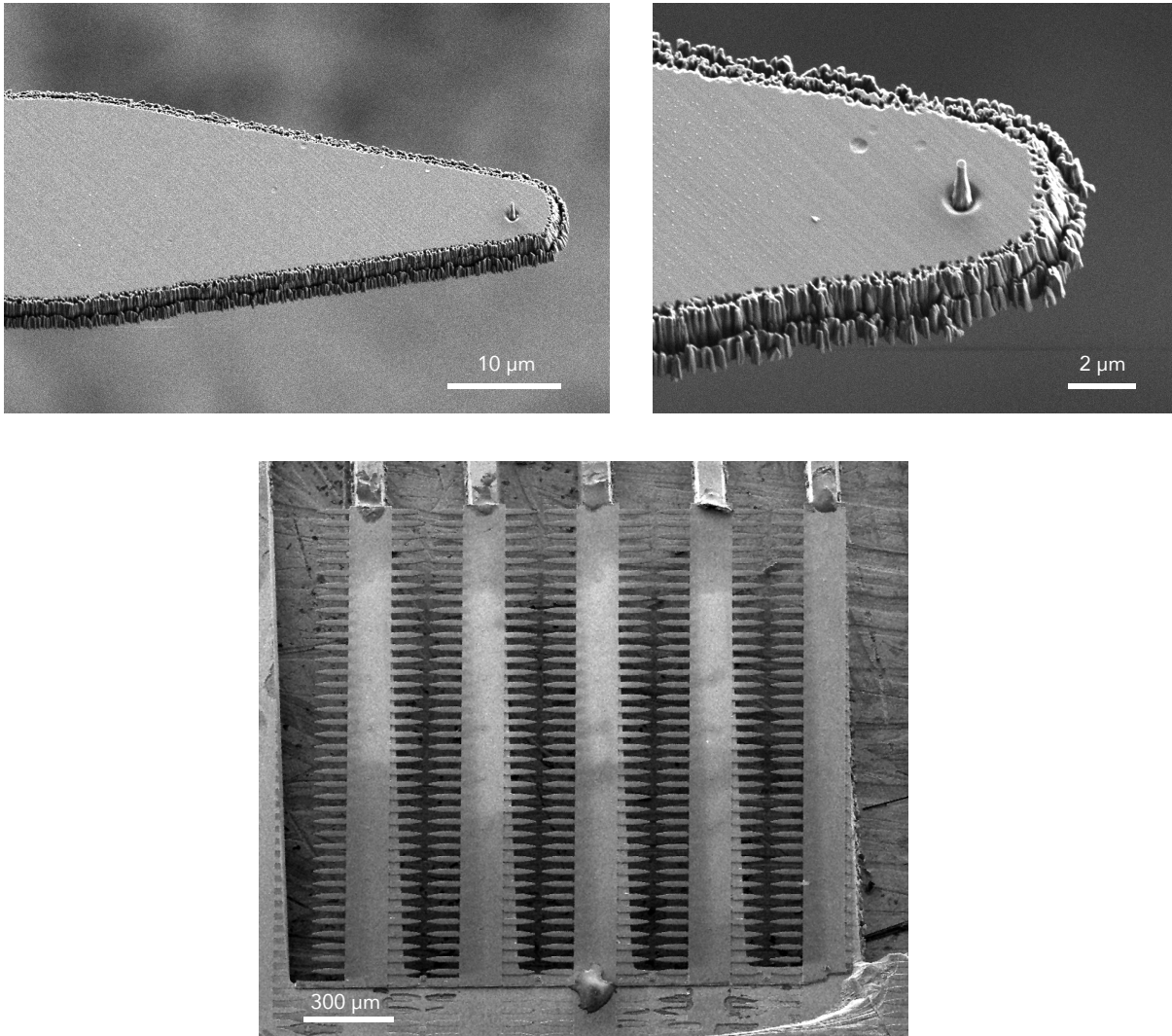
Figure 3.6: (top) SEM images of a diamond probe. (bottom) 2×2 mm diamond chip containing an array of diamond probes.

3.2.3   Characterization

After the fabrication of a set of probes, an initial characterization is required to
find the usable ones. In our process, we form NVs at a uniform, high density over the
whole surface of the diamond plate, without any alignment of our probe lithography
to the locations of individual NVs. Aligning the pillar fabrication to individual NVs is
possible, but tricky [77]. Instead we just make a large number of probes and if we form
NVs at the right density, then in the end some fraction of them will host single NVs
with good magnetic field sensitivity. To screen the good probes we filter them using PL
rate, CWESR contrast, number of distinct NV splittings, and finally a $g^{(2)}$ correlation
measurement like that described in Sec. 2.1.5. Figure 3.7(a) shows an example of a
confocal image of an NV in a probe, and Fig. 3.7(b) shows a representative Hahn echo
measurement for an NV in a pillar. The 58 µs T_2 shown is representative of the upper
end of the T_2 measurements for this set of 400 nm diameter pillars, while there is a large
spread in T_2 times, down to a few µs. The NVs with longer coherence times, $T_2 \sim 50$
µs, appear to be limited by the density of paramagnetic substitutional nitrogen defects,
known as P1 centers. In the limit where the P1 centers dominate the decoherence of
the NV, the $1/T_2^*$ and $1/T_2$ decoherence rates are expected to be inversely proportional
to the nitrogen density [78], with $(1/T_2^*) \approx 0.5\rho_{P1}$ MHz/ppm and $(1/T_2) \approx 0.07\rho_{P1}$
MHz/ppm where ρ_{P1} is the nitrogen density in ppm. Elsewhere these relationships have
been quoted as $(1/T_2^*) \approx 0.19\rho_{P1}$ MHz/ppm and $(1/T_2) \approx 0.05\rho_{P1}$ MHz/ppm [30].
Roughly approximating the nitrogen density in our implanted probe samples using the
straggle calculated by SRIM and the implantation densities, we get nitrogen-limited T_2^*
times of 5-13 µs and T_2 times of 35-50 µs from this model.

To mount the probes for scanning, a micromanipulator is used to glue a pulled glass
piece to one of the cantilevers. The pulled glass is then pushed down to break off the
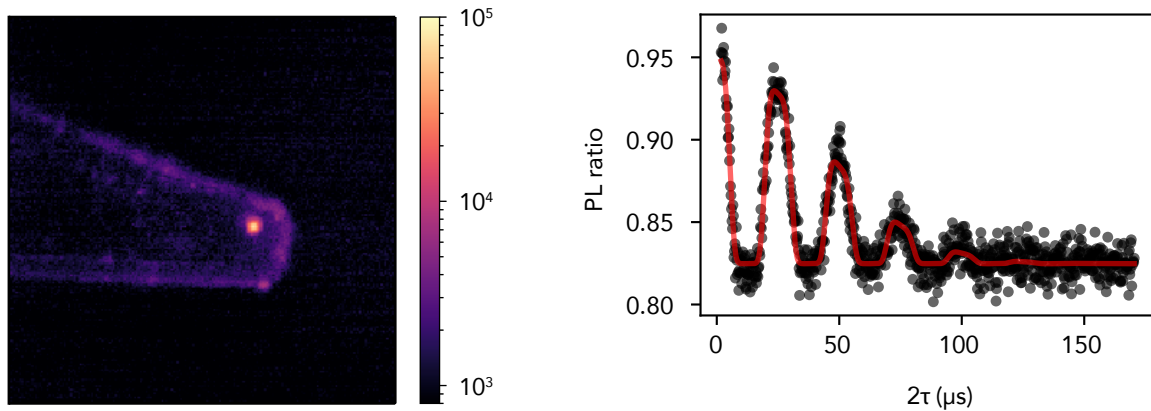
Figure 3.7: (a) Confocal image of a diamond probe. The bright spot is a single NV in a diamond pillar. The image is taken using an SM800 fiber for collection. (b) Example of a Hahn echo measurement of an NV T_2 coherence time. The decay envelope of the ^{13}C collapses and revivals is 58 µs. The total free precession time is 2τ and the PL signal is plotted in terms of the contrast ratio between the Hahn echo measurement at time 2τ and the PL rate in the $|m_s = 0\rangle$ state.

cantilever. Sometimes sharply tapping the micromanipulator table can break the can-tilever free. The other end of the pulled glass piece is connected to a 32 kHz tuning fork, which is used for AFM sensing. An image of a pulled-glass piece connected to a tuning fork is shown in Fig. 3.8(a), and Fig. 3.8(b) shows a pulled glass piece being glued to a cantilever.
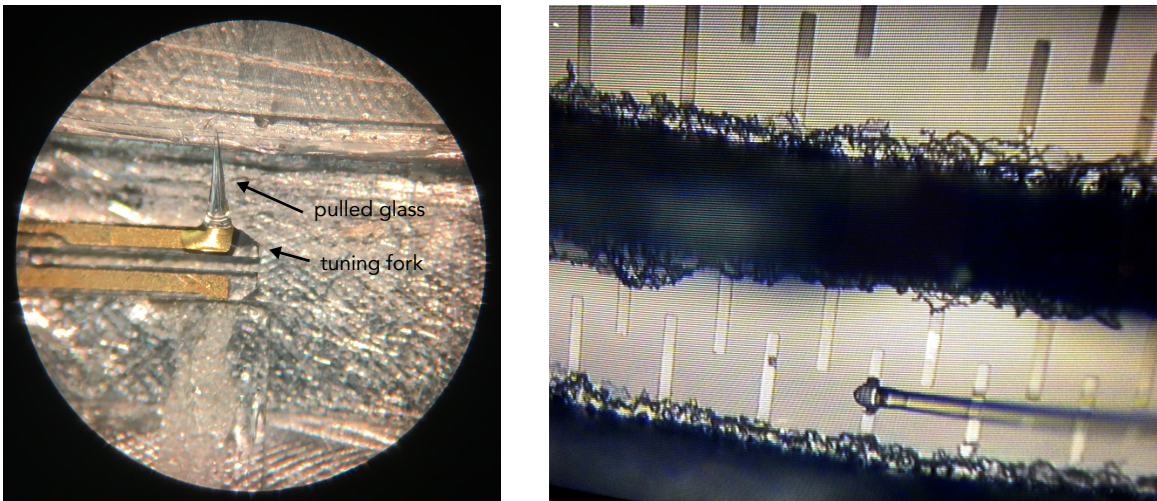
Figure 3.8: (a) Optical image of a pulled glass piece glued to a 32 kHz tuning fork. (b) Screenshot of a pulled glass piece being glued to a toothbrush-style cantilever (see Fig. 3.20). The pillars are facing downward in this image.

3.3   Confocal and AFM design

Scanning NV magnetometry with these diamond probes is performed using a custom-built AFM system inside a closed-cycle cryostat together with a custom confocal microscope. The tricky bit is balancing the coupling between these two microscope systems and the cryostat vibrations.

3.3.1   Optical closed-cycle cyrostat

The closed-cycle, optical cryostat is a Nanoscale Workstation, made by Montana Instruments. A top-down view of the cyrostat insides is shown in Fig. 3.9. The platform and the radiation shield are connected to two stages of the cold head through a pair of concentric cylinders. At base temperature, the 1st stage of the cryocooler gets down to around 40 K and has a cooling power of a few W. The second stage gets down to $\sim$4 K and has a cooling power around 100 mW. The concentric cylinders are connected to the platform and radiation shield with a floppy mechanical connection made of high purity copper, that help minimize the coupling of the cold head mechanical vibrations to the platform. Depending on the heat-sinking from the platform to our sample mount, we can get sample temperatures around 5–8 K. It takes about 28 hours to reach this base temperature when cooling from room temperature. The outer black ring surrounding the bottom of the radiation shield in Fig. 3.9 is a PCB board with electrical feedthroughs. It is recommended that this board be replaced by a metal plate.

The photo in Fig. 3.9 also shows the fine and coarse positioners of the AFM system. The large triangular stage is a coarse positioner consisting of six piezo-stepper knobs. It is a custom-built positioning system made by Janssen Precision Engineering. These knobs use alternating slow and fast cycles of piezo extension to produce a slip-stick motion of the knob, turning a finely threaded screw. The screws press on flexible plates, thereby

tilting the triangular stage. By moving all three knobs in the right ratio Cartesian x, y, and z motion can be produced, albeit with some tilting of the sample or tip mount with respect to the z-axis. There are two sets of these knobs, an outer set, for positioning the sample and diamond tip relative to the external confocal optics, and an inner set (hidden underneath that titanium ring in the photo), for positioning the sample with respect to the tip. Atop the inner JPE stage, there is an ANSxyz100hs Attocube scanner for fine positioning and imaging.
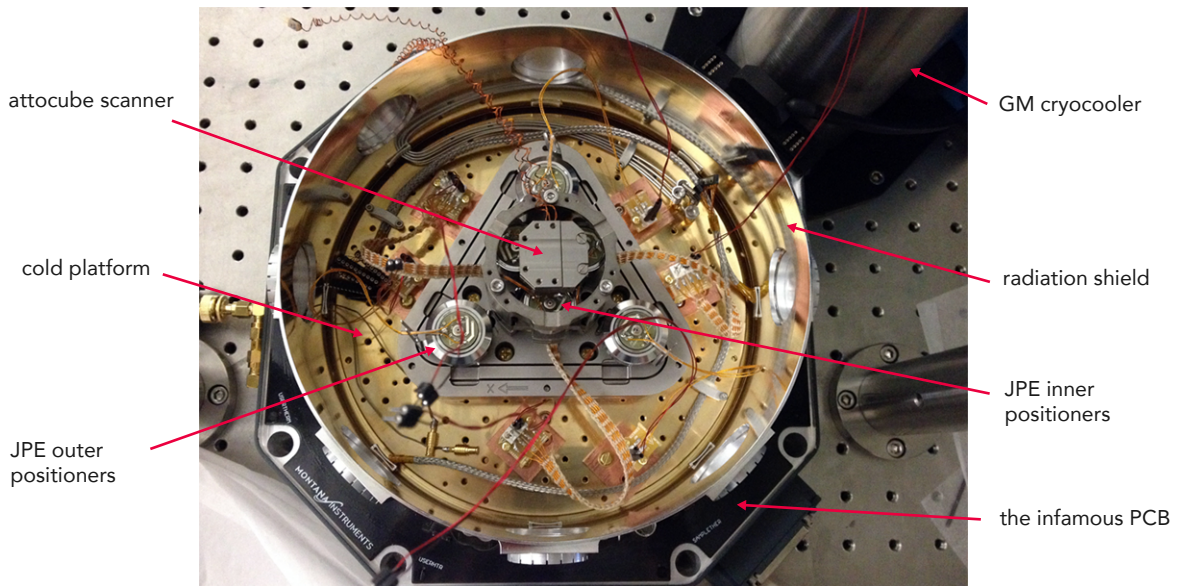
Figure 3.9: Top-down view of the cryostat with AFM positioners exposed. A custom pair of triangular JPE positioners is used for coarse positioning of the tip and sample with respect to the confocal microscope, and an attocube scanner is used for fine positioning when imaging. The cyrocooler is visible in the top right of the photo.

The triangular design of the JPE positioners was chosen because it allows the stage to be designed with a higher frequency mechanical resonance, but it does have the downside that the sample tilt changes as the sample is moved around. This is a small effect however and the sample tilt only changes by a few degrees relative to the diamond probe over the whole x-y range of the inner positioner. The outer positioner range is about $6 \times 6 \times 6$

mm and the inner range is roughly $1 \times 3 \times 3$ mm, where these numbers represent the maximum $x \times y \times z$ displacement ranges. These positioning ranges don't correspond to a cubic volume because of the tilt-type motion of the positioners. See Appendix B for a description of the JPE stage positioning volume.
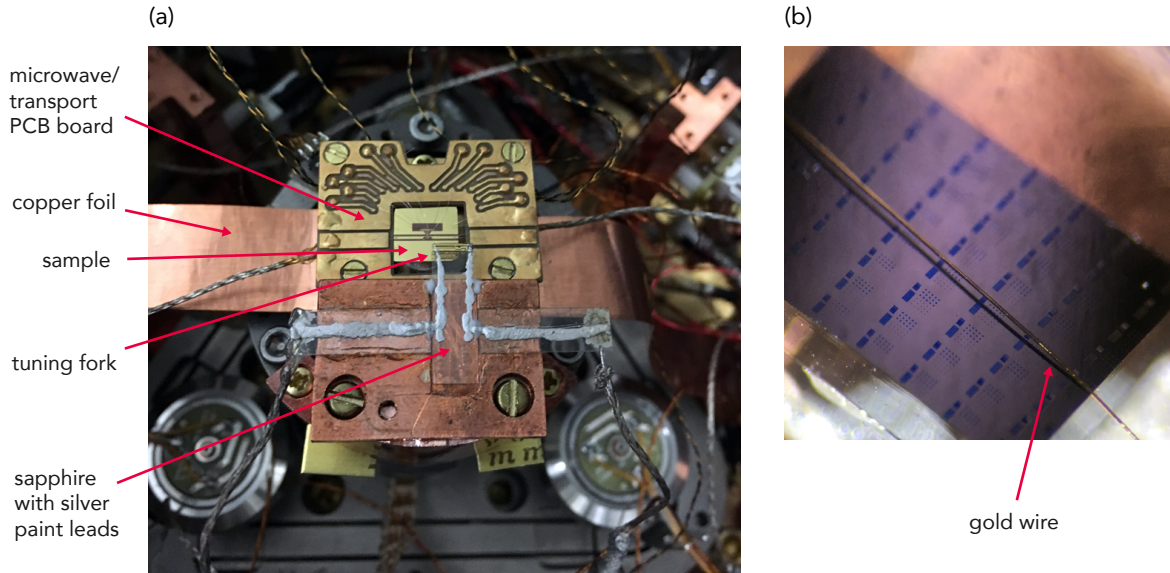

Figure 3.10: (a) Top down view of the inside of the cryostat, with a sample and diamond probe mounted. An RF waveguide is visible on the sample mount PCB board, as well as another waveguide on the sample chip itself. The copper tip mount supports 0.2 mm sapphire pieces with electrical leads drawn on in order to connect to the tuning fork. The pulled glass and diamond probe are hard to see at this scale. (b) An example of wire-bond delivery of microwaves. A thin gold wire is stretched over the sample and the scanning NV measurements are performed just next to the wire.

Figure 3.10(a) gives a top-down view of the system with the scanner, PCB board, sample, and tip mount installed. Microwaves are delivered to the NV with waveguides on PCB, connected to a waveguide on the sample itself. Electrical connections to the tuning fork are made by drawing silver paint leads on pieces of sapphire connected to the copper tip mount. An alternative method of delivering microwaves involves bonding a thin gold wire over the sample as shown in Fig. 3.10(b).

A superconducting vector magnet was added on the system after the fact. It is shown

in Fig. 3.11 The magnet can produce a 0.1 T field in an arbitrary direction, and a 0.5 T field along the z-axis. The magnet wires are made from niobium-tin and need to be thermally anchored to the platform, with the platform set to its base temperature. The wires are connected to BSCCO high-T_c superconducting leads that bridge the temperature gap from the platform to the radiation shield. Long copper leads connect from the radiation shield to room temperature vacuum feedthroughs. The length and diameter of these copper wires is optimized for the amount of current flowing in the leads. This implies different diameter leads for the x/y leads vs. the z leads because the current-to-field ratio is larger for z and more current will need to be applied to the x or y leads to align the field to the NV axis of our $\langle 100 \rangle$ probes. Running enough current to produce the 0.1 T vector field will heat the platform by several K and care should be taken to not quench the magnet when operating at large fields and simultaneously heating the sample.

The sample can be heated somewhat independently of the platform using an Agile Temperature sample mount from Montana Instruments, which is designed to quickly heat and cool a small mass sample with a small amount of heat. In the configuration where a large magnetic field and a high sample temperature is desired, it is best to minimize the thermal connection from the sample to platform by removing the high-purity copper foil (Fig. 3.10(a)) that is normally used for sample heat-sinking.

Operation of this magnet pushes the cooling power of the Nanoscale Workstation coldhead to its limit, causing the radiation shield to heat significantly. Also, the magnet is not well-designed for vacuum compatibility. When the magnet is not required, it should be removed and the copper magnet leads should be disconnected from the radiation shield.

Figure 3.12 shows a cut-away of the cyrostat design. The objective is lowered into a recession in the outer housing. A 12 mm diameter, 200 micron thick BK7 glass window holds vacuum just below the objective. The height of this window can be adjusted over a range of several mm, by rotating the (leaky) threaded recession. A 100-200 micron
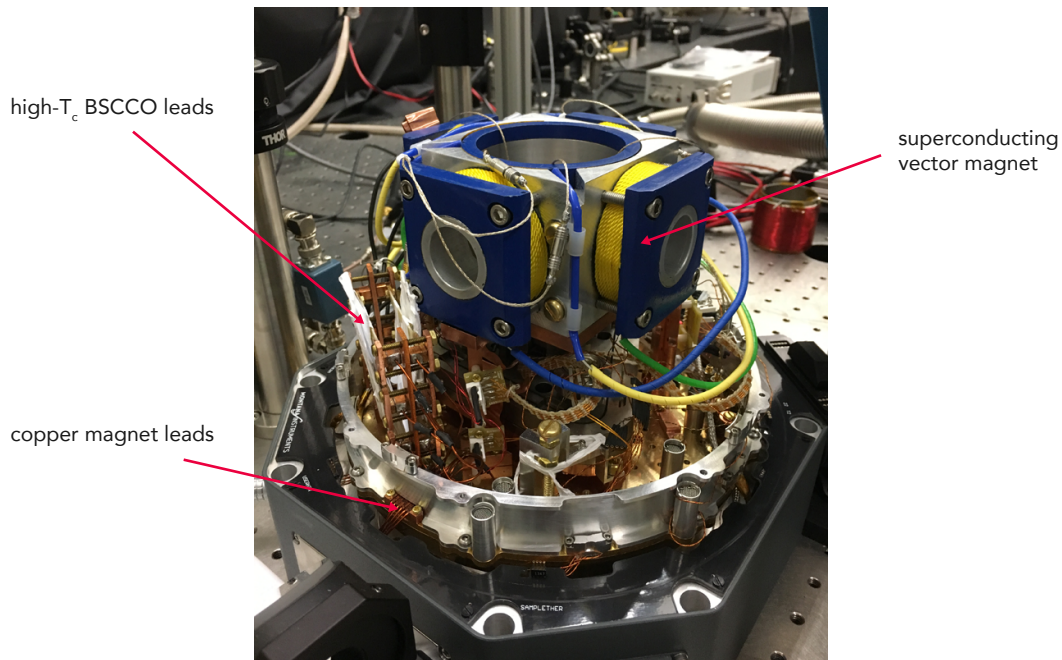
Figure 3.11: Superconducting vector magnet installed in the cryostat.

glass slide can be attached to the radiation shield recession, shielding the sample from thermal radiation of the outer, room temperature window. More importantly, it also acts as barrier to the formation of ice on the sample, probably due to a leak in the adjustable window recession, which would otherwise prevent scanning experiments below ~ 115 K.

Figure 3.13 has the dimensions of various spacings and thickness of parts between the microscope objective and the diamond probe. The distance from the diamond to the top of the inner, radiation shield window depends on the tip construction (pulled-glass length and angle, tuning fork position on the sapphire piece, sapphire on the tip mount, position of outer JPE stage relative to its center). In recent experiments, it has been limited to a distance > 1.7 mm. Below that point it touches some feature on the tip mount. The maximum distance between the outer window and the tip is around 2.5 mm. If this distance is much larger, then the objective will run into some feature on the outer housing before it can focus on the NV. In the end, taking into account small

tilts of the various parts, pieces of glue, etc. there is hardly any room to spare. In a recent cool-down, the final distance between the objective and outer housing was about 50 µm, the distance between the tallest feature of the tip mount and the radiation shield was about 20 µm, and the distance between the radiation shield and the outer housing was about 100 µm. During a cool-down to base temperature, the AFM stage will often contract $\sim$200 µm, and the radiation shield will contract as well, $\sim$50–100 µm. This means that we need independent control over the tip to radiation shield distance and the radiation shield to outer window distance. The outer JPE stage is used to control the former, while the threaded, adjustable window recession is used to control the latter.
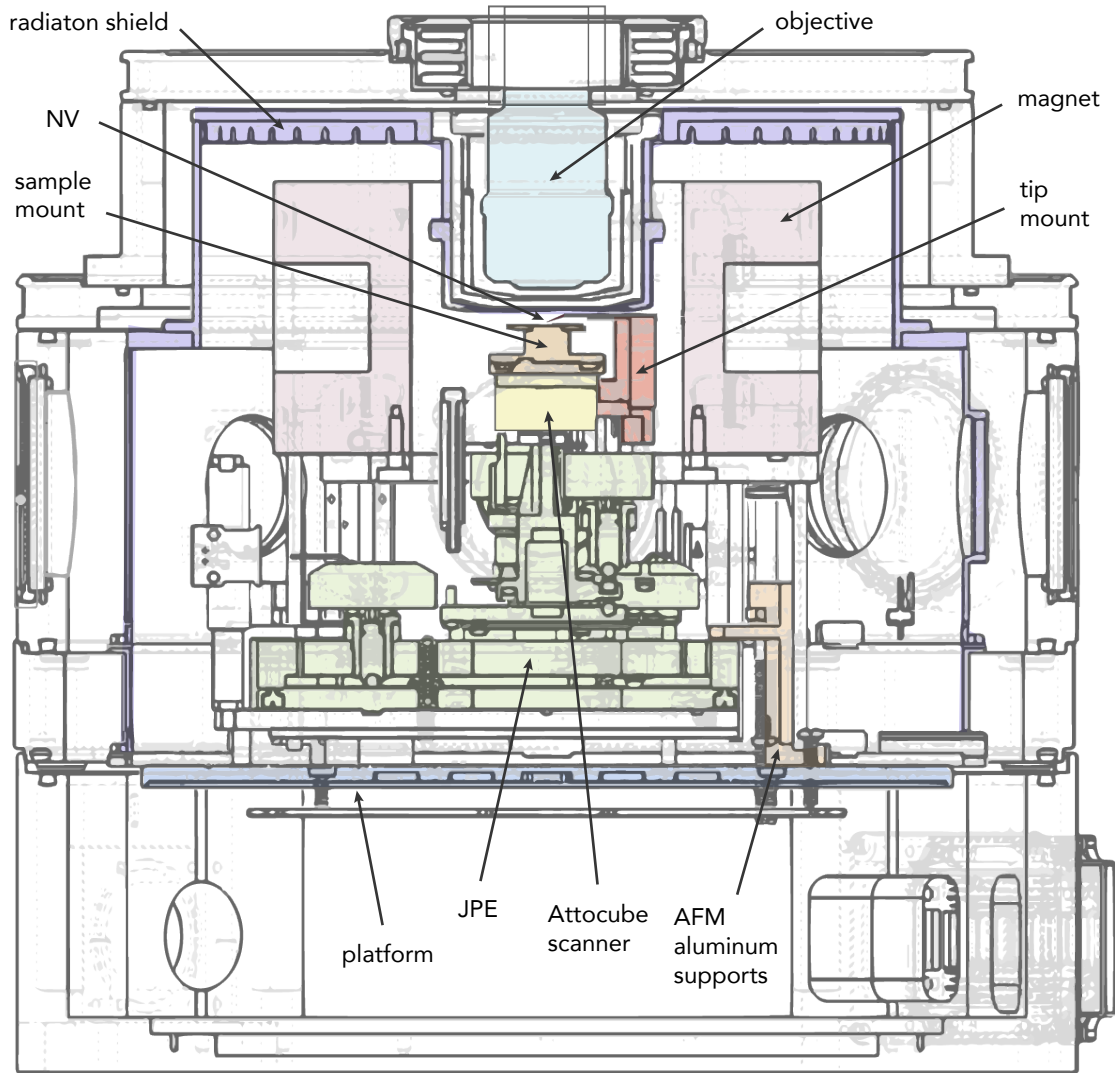
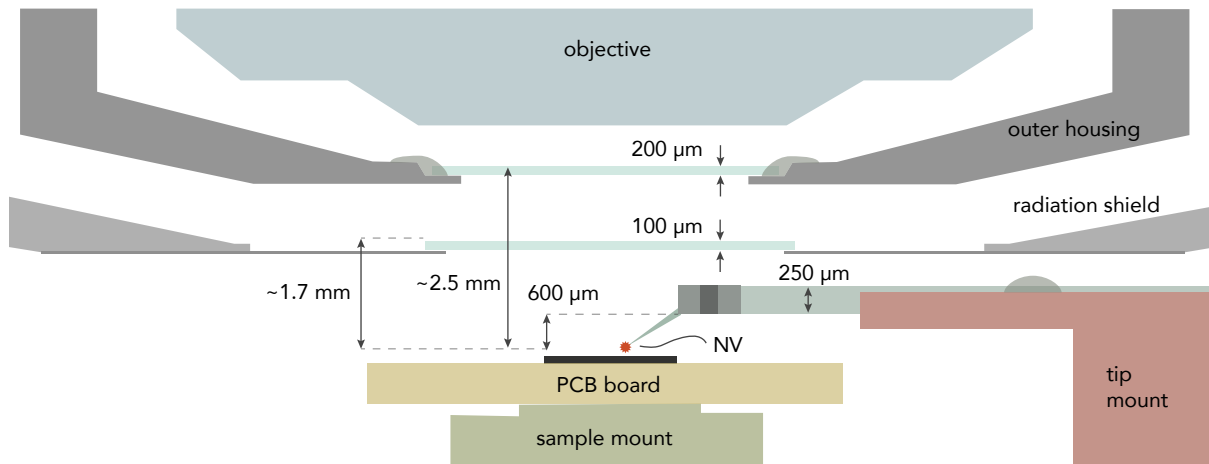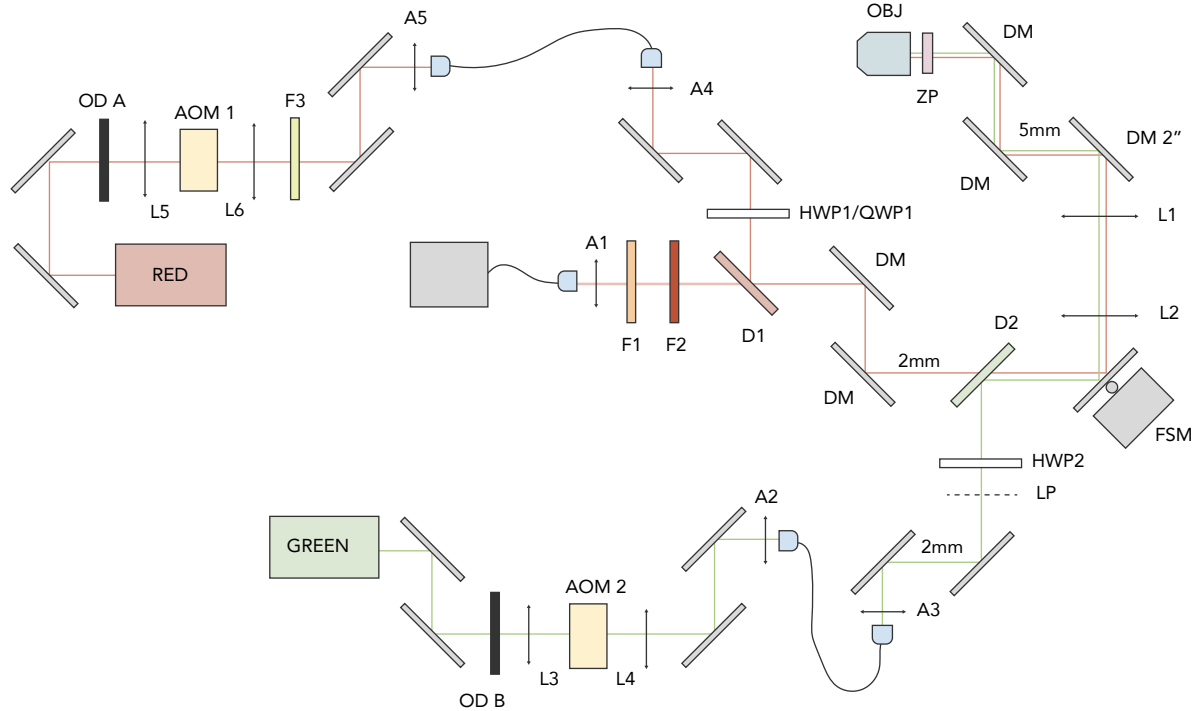Figure 3.12: Diagram of the cryostat design.

Figure 3.13: Spacing of objective, windows and tip. The distances are stretched along the y-axis for clarity.

3.3.2   Confocal microscope

APD	Excelitas SPCM-AQRH-14-FC
RED	New Focus 6304-LN
GREEN	Thorlabs DJ532-40/LDM56
AOM1/2	Intraaction ATM-200C1
FSM	Newport FSM-300-02
ZP	nPoint nPFocus250SG
OBJ	Olympus LCPLFLN50xLCD
F1	Semrock BLP01-594R-25 (bandpass)
F2	Semrock NF03-633E-25 (notch)
F3	Edmund 65-712 (633 bandpass)
D1	Semrock FF650-Di01-25x36 (dichroic)
D2	Semrock FF560-Di01-25x36 (dichroic)

L1	Thorlabs AC508-750-B-ML
L2	Thorlabs AC508-300-B-ML
A1	Thorlabs C240TME-B (8 mm)
A2	Thorlabs C170TME-A (6 mm)
A3	Thorlabs C220TMD-A (11 mm)
A4	Thorlabs C240TME-B (6 mm)
A5	Thorlabs C240TME-A (8 mm)
H(Q)WP1	Foctek WPF212H(Q)-633nm
HWP2	532 nm 1/2 waveplate
LP	linear polarizer
DM	Thorlabs BB1-EO2 (dielectric mirror)

Figure 3.14: Diagram of the confocal microscope optics.

A layout of the confocal optics is shown in Fig. 3.14. Starting from the green diode laser, the excitation path goes through a neutral density filter, which is used to set the optical power, and is focused into a TeO_2 acousto-optic modulator (AOM). This AOM is used to quickly turn the laser on and off (within tens of ns) in pulse sequence measurements. The first order deflected beam is coupled into a single-mode, polarization

maintaining fiber, while all other modes are blocked with an iris (not shown in the diagram). The output of the excitation fiber is collimated and sent through a linear polarizer and a half-wave plate. The half-wave plate is used to align the excitation polarization perpendicular to the axis of the NV. The beam then reflects off a dichroic mirror designed to reflect light below 560 nm and transmit light above this wavelength. The beam then reflects off a fast steering mirror. This FSM-300 mirror can tilt in both x and y directions over a $\pm$ 1.5° range, giving an optical angle range of $\pm 3°$. The beam then travels through a telescope. The first lens L1 has focal length $f_1 = 300$ mm and the second L2 has focal length $f_2 = 750$ mm. The green beam is expanded by this ratio of 5/2. The lenses are spaced so that L1 is a distance f_1 from the steering mirror, L1 and L2 are a distance $f_1 + f_2$ apart, and L2 is a distance f_2 from the back aperture of the microscope objective. This spacing converts changes in steering mirror tilt into changes in focal position on the sample, while keeping the excitation power transmitted through the objective roughly constant. A piezo stage is used to change the focus position by moving the objective up and down over a 250 micron range. Our objective, an Olympus LCPLFLN50xLCD, has a 0.7 NA and a 3.0 mm working distance. It has an adjustable window correction collar, that allows us to use the objective at room temperature without any window, or use it looking through the outer cryostat window and radiation shield window. This working distance is actually a bit too short for looking through two windows, one of which is holding vacuum, and focusing down below the tip mount and tuning fork onto a diamond probe.

Light collected by the objective from the volume near the green excitation focus travels backwards through the same optical path until it reaches the dichroic mirror. At this point, light below the 560 nm cutoff is reflected and longer wavelengths, like those comprising the NV fluorescence are transmitted. The amount of red fluorescence collected from a single NV is very small, and so another color filter, with a higher rejection

ratio (OD 5-6) is used to filter light below 594 nm before it is fiber coupled and sent to our single-photon detector. The fiber is either an SM800 or 50 micron core multimode fiber. With a multimode fiber, we can usually get much higher collection rates from the diamond pillars, without sacrificing too much contrast from the increased background of the larger collection volume. The figure also shows another excitation path, with a red external cavity diode laser, used for resonant excitation of the NV. The optics in this path have been cannibalized by other experiments due to infrequent use.

During a scanning measurement, the confocal microscope's only purpose is to optically address the NV, and periodically shift the focal position to correct for any drift in the optics. For this purpose, it seems like an unnecessarily large optical setup. In the future, maybe this optical system can be replaced by some type of fiber-coupled structure integrated with the diamond probe.
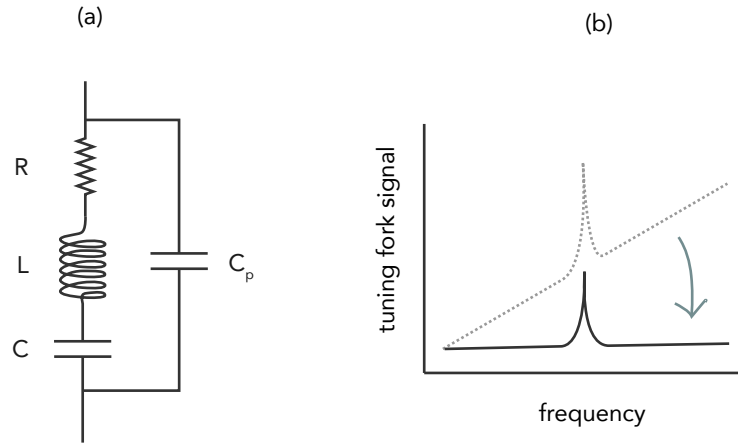
Figure 3.15: (a) Equivalent circuit model of a tuning fork resonance. The tuning fork behaves as an RLC circuit in parallel with a physical capacitance $C_p \sim 10$ pF. (b) Tuning fork signal resonance shape. Another 10 pF capacitor is added in parallel to the tuning fork drive circuit (see Fig. 3.17), and supplied with the inverted drive signal. The current running through this nulling capacitor cancels the current through C_p removing the large capacitive background of the resonance signal.

3.3.3   AFM

Our AFM system has already been described a bit at the beginning of the chapter. The fine positioning of the sample underneath the diamond probe is achieved with an xyz Attocube scanner and the sample is approached coarsely with the inner JPE piezo knobs.

The AFM sensing uses a 32 kHz tuning fork from Citizen Finetech Miyota. The resonance response of the tuning fork is described in Fig. 3.15. The tuning fork is used in a shear sensing mode, with the prongs of the fork oscillating mostly parallel to the surface of the sample (Fig. 3.16). This saves precious working distance under the objective. One prong of the fork is glued to a sapphire piece and the pulled glass is mounted on the other. After the pulled glass is attached to the tuning fork and the sapphire attached to the tip mount, the resonance frequency of the tuning fork is usually several kHz lower than the starting 32.768 kHz. The tuning fork resonance Qs are usually somewhere in the range of
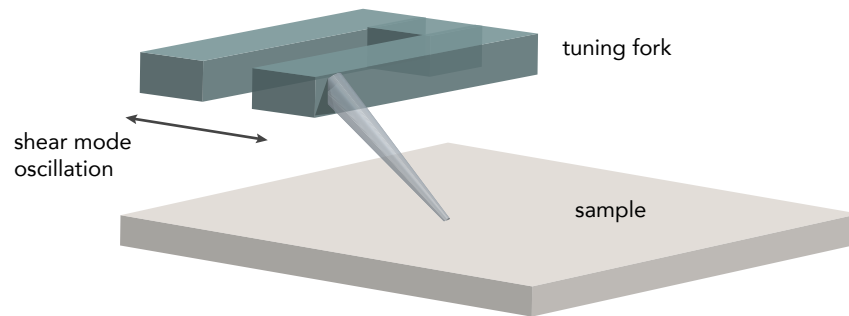
Figure 3.16: Shear mode oscillation. The tuning fork oscillates in a plane mostly parallel to the sample surface.

several hundred to 1500 after mounting. Custom coaxial wires with graphite between the insulator and shielding from Calmont Wire & Cable [79], designed for low triboelectric noise, are used inside the cryostat to prevent cyrocooler-induced mechanical vibrations of wires coupling to tuning fork signal path. We operate the AFM in amplitude mode, with a fixed drive amplitude and frequency. The piezoelectric response of the quartz tuning fork converts the electric drive into mechanical motion. When the drive frequency matches the mechanical resonance of the tuning fork, a small AC current is driven through leads that wrap around the tuning fork prongs. This AC current is amplified with a fixed-gain Femto current amplifier and mixed with the drive signal inside a lock-in amplifier. When the tip approaches the surface, the resonance amplitude decreases, the frequency shifts, and the lock-in signal decreases as a result. Figure 3.17 shows a rough schematic of the AFM circuit. The lock-in signal is used to feedback on the sample-tip shear force by adjusting the sample height to maintain a fixed tuning fork signal. Detailed circuit diagrams of the AFM electronics can be found in Appendix C.
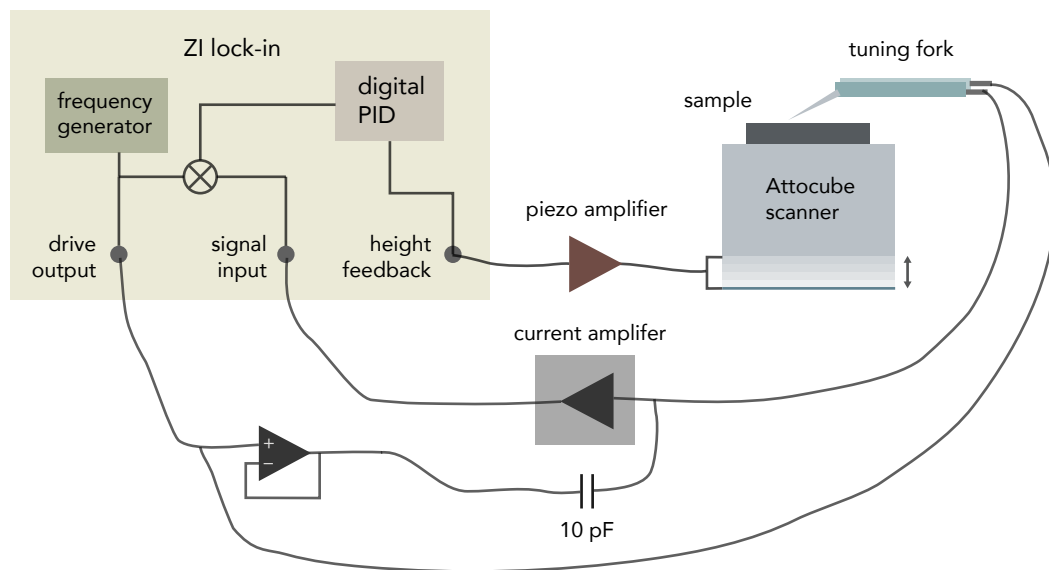
Figure 3.17: Overview of the AFM circuit. A Zurich Instruments HF2LI lock-in amplifier (ZI) drives the tuning fork. The tuning fork current is amplified by a Femto LCA-100K-50M. The tuning fork signal is sent back to the ZI lock-in and the demodulated signal is given to a digital PID controller in the ZI. The output of the PID controller is added to the sample height output of a NI DAQ channel, amplified in a Thorlabs MDT693B piezo amplifier, and sent to the z channel of the Attocube scanner.

3.3.4   Balancing optical and AFM vibrations

The thermal connections to the platform and radiation shield in the Montana Instruments Workstation are designed to minimize mechanical coupling of the cold-head vibrations, but for AFM scanning, further decoupling of these vibrations from the AFM system is required. The best way to do this is to suspend the whole JPE positioning system from very floppy (low stiffness) springs. If the natural resonance frequency of this spring system is well below the resonance frequency of the JPE/Attocube/tip-mount system, then it will act as a lowpass filter for the vibrations that would move the tip relative to the sample. Doing this, we were able to achieve sub-nm RMS tip-sample vibrations. But unfortunately, with low-k springs, the vibrations of the optical system relative to the tip were too large, up to a 100 nm or so. So we had to make a trade-off, and choose a support structure with stiffness high enough that the optical vibrations were not too severe (~ 10 nm scale), but low enough that the AFM vibrations stay under a few nm when the cryocooler is running. This support structure is shown in Fig. 3.18. It consists of three pairs of thin aluminum Ls, acting like high-k springs. The AFM vibration amplitudes are characterized using a glass tip glued to a tuning fork mounted in amplitude mode (oscillating normal to the sample plane). The tuning fork is driven hard enough that the sample-tip vibrations perturb the resonance signal linearly, and the vibration amplitude is calibrated relative to the amplitude change measured when raising the sample several nanometers with the piezo scanner.
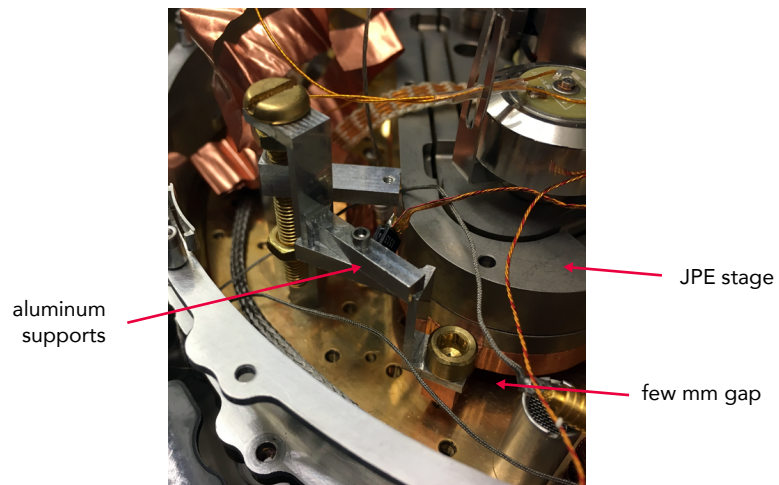
Figure 3.18: Photograph of the aluminum support "springs".

3.4 Demonstrating scanning NV magnetometry at cryogenic temperatures

After constructing this system, we demonstrated its utility in some initial tests on a magnetic hard-disk drive and a high-T_c iron pnictide superconductor. The work described in this section was one of a pair of experiments demonstrating the first cryogenic scanning NV magnetometry [32, 80] [1]. In these first experiments, we demonstrated NV scanning at 6 K with 6 nm spatial resolution (in the imaging plane) and 3 µT/$\sqrt{\text{Hz}}$ DC field sensitivity. Figure 3.19 shows contour images of bits in the HDD and vortices in a type II superconductor.
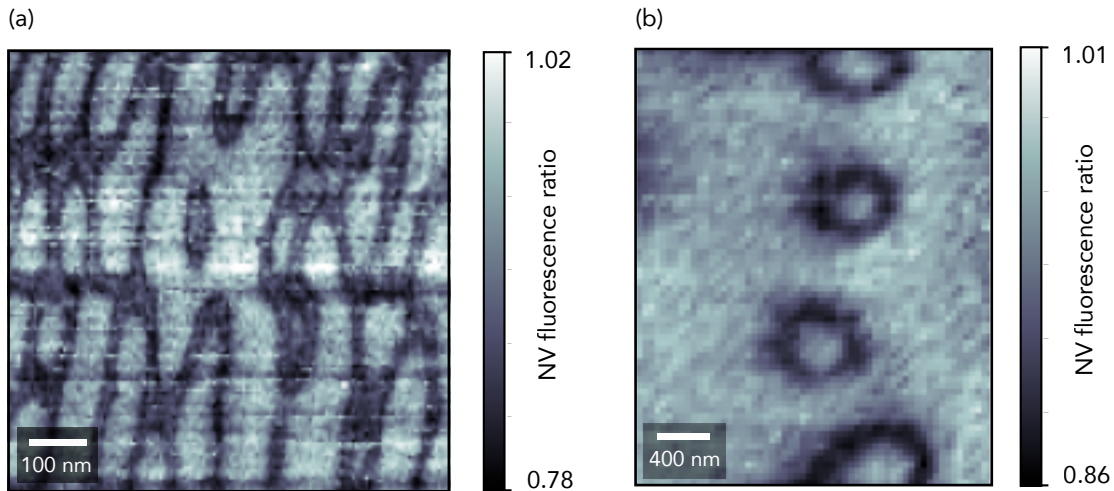

Figure 3.19: (a) NV magnetometry image of the bits of a hard disk at $T = 6$ K. The dark contours in the image correspond to locations where the stray field from the hard disk has a magnitude of 5.3 G (resonant with a 2892.7 MHz RF field) along the axis of the NV center. (b) NV magnetometry image of vortices in the superconductor BaFe$_2$(As$_{0.7}$P$_{0.3}$)$_2$ at $T = 6$ K. Analogous to b, dark features correspond to the 5.9 G magnetic field contours (2862 MHz RF field). Vortices were formed by cooling the sample through its superconducting transition ($T_c = 30$ K) in a 10 G external field.

[1]The contents of this section have partly appeared in [32]: M. Pelliccione, A. Jenkins, P. Ovartchaiyapong, C. Reetz, E. Emmanouilidou, N. Ni, and A. C. Bleszynski Jayich, Scanned probe imaging of nanoscale magnetism at cryogenic temperatures with a single-spin quantum sensor. Nature Nanotechnology, 11(8):700–705, 2016.

These first experiments used a toothbrush-style diamond probe like that shown in Fig. 3.20. These toothbrushes are nice because each probe has an abundance of NVs to choose, and it is always possible to find a pillar with a single NV with good sensitivity. They could also prove useful for sophisticated wide-FOV imaging techniques where multiple pillars are read-out simultaneously, potentially speeding up the imaging speeds significantly. The downside to this geometry is that most of the NVs are greater than several hundred nm away from the sample, even for very small tilt angles. This limits the resolution when using any NV that is not the in-contact pillar. And the in-contact pillar is not always guaranteed to have a useful NV. For this reason, we have mostly switched to using single-pillar probes in more recent work.
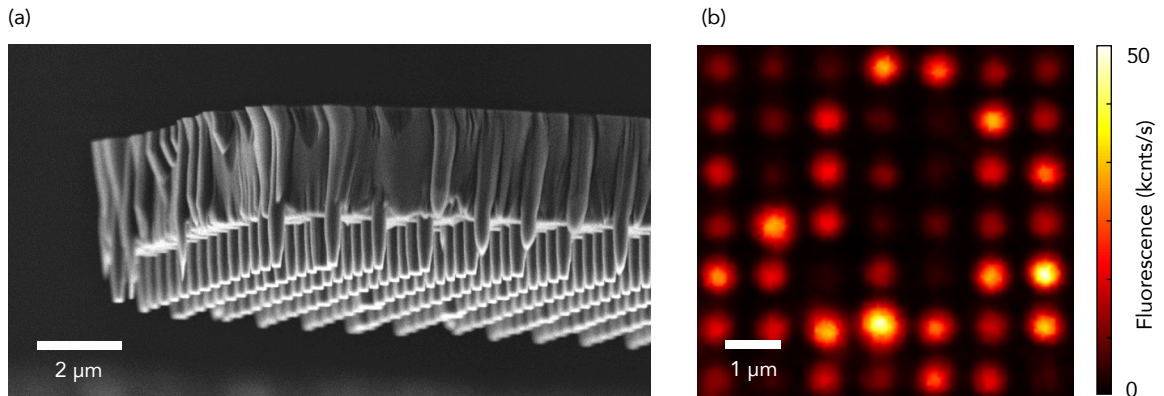

Figure 3.20: (a) SEM image of a typical diamond cantilever fabricated for magnetometry. Each full cantilever measures $150 \times 20 \times 3$ µm . On average, there is approximately one NV center per pillar. (b) Confocal microscopy image of an array of pillars on a cantilever showing NV fluorescence from a majority of pillars. A green excitation power of 30 µW was used.

Figure 3.21 demonstrates the nanoscale spatial resolution of the system. Figure 3.21a is a magnetic contour image ($B_c = 7.9$ G) of a hard disk at $T = 6$ K, with a corresponding linecut shown in Fig. 3.21b (point spacing of 6 nm). From the linecut, the magnetic field at two points separated by 6 nm is well resolved within the error of the measurement. However, this does not necessarily correspond to the smallest magnetic domain resolvable

in the scan, only the resolvable field gradient in the plane of the NV sensor. The ultimate resolution of the image in Fig. 3.21a, which clearly shows domains under 100 nm in size, will depend also on the separation of the NV center from the surface during the scan. The imaging-plane spatial resolution, δx, is ultimately determined by the magnetic field gradient $\nabla_x B_{NV}$ and the linewidth of the NV ESR transition, $\delta x \approx 1/(T_2^* \gamma \nabla_x B_{NV})$. In these measurements, $T_2^* = 250$ ns and $\nabla_x B_{NV} \approx 0.25$ G/nm at the location of the contours. Fig. 3.21 was used to confirm that mechanical vibrations and drift during the low-temperature measurements are well below 6 nm.
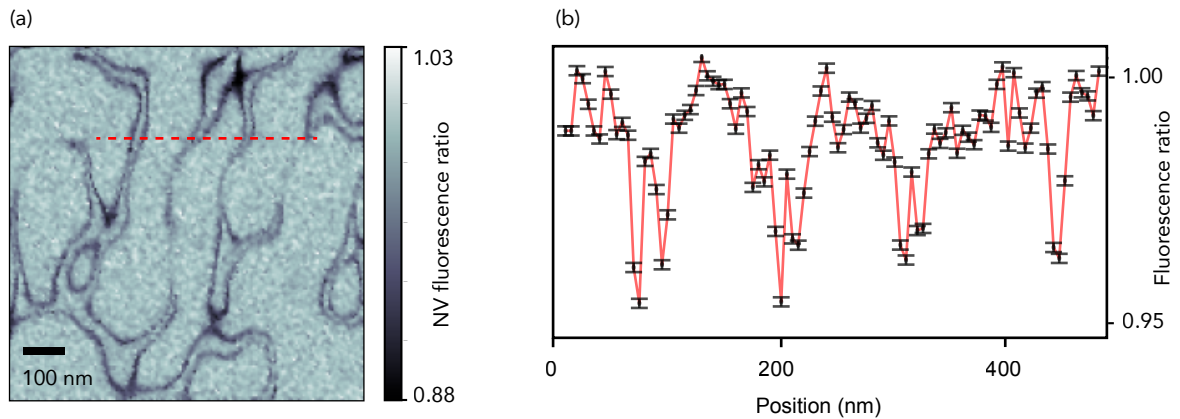

Figure 3.21: (a) Magnetic field contour image of a hard disk (7.9 G, 2900 MHz RF excitation). (b) One-dimensional line-cut along the red line in a. Features in the imaging plane are clearly resolved down to a spatial resolution of 6 nm, which is set by the point spacing in the scan. This data highlights the nanoscale spatial resolution of the NV sensor and the vibrational stability of the cryogenic imaging system. The error bars reflect one standard deviation confidence intervals due to photon counting statistics.

Magnetometry images of vortices in the iron pnictide superconductor $BaFe_2(As_{0.7}P_{0.3})_2$ at 6 K are shown in Fig. 3.22. The images were taken with the contour imaging method. The sample was cooled through its superconducting transition ($T_c = 30$ K) in a 10 G magnetic field applied perpendicular to the ab plane of the sample. The dark circular features, which correspond to field contours of 5.9 G (Fig. 3.22(a)) and 8.8 G (Fig. 3.22(b)), are due to the stray field from the two vortices in each figure. The contours

shrink in size when comparing Fig. 3.22(a,b), as the NV must be brought closer to the center of the vortex to match the higher magnetic field ESR resonance condition. The measured vortex density, estimated using the larger scan area in Fig. 3.19(c), is approximately $0.45 \pm 0.1/$µm. This value is consistent with the calculated vortex density of $(10$ G$)/\Phi \approx 0.5$ /µm assuming each vortex is associated with one magnetic flux quantum $\Phi = h/(2e)$. As another confirmation of the superconducting nature of the signal, the measured magnetic response disappears when the sample is heated above $T_c = 30$ K.
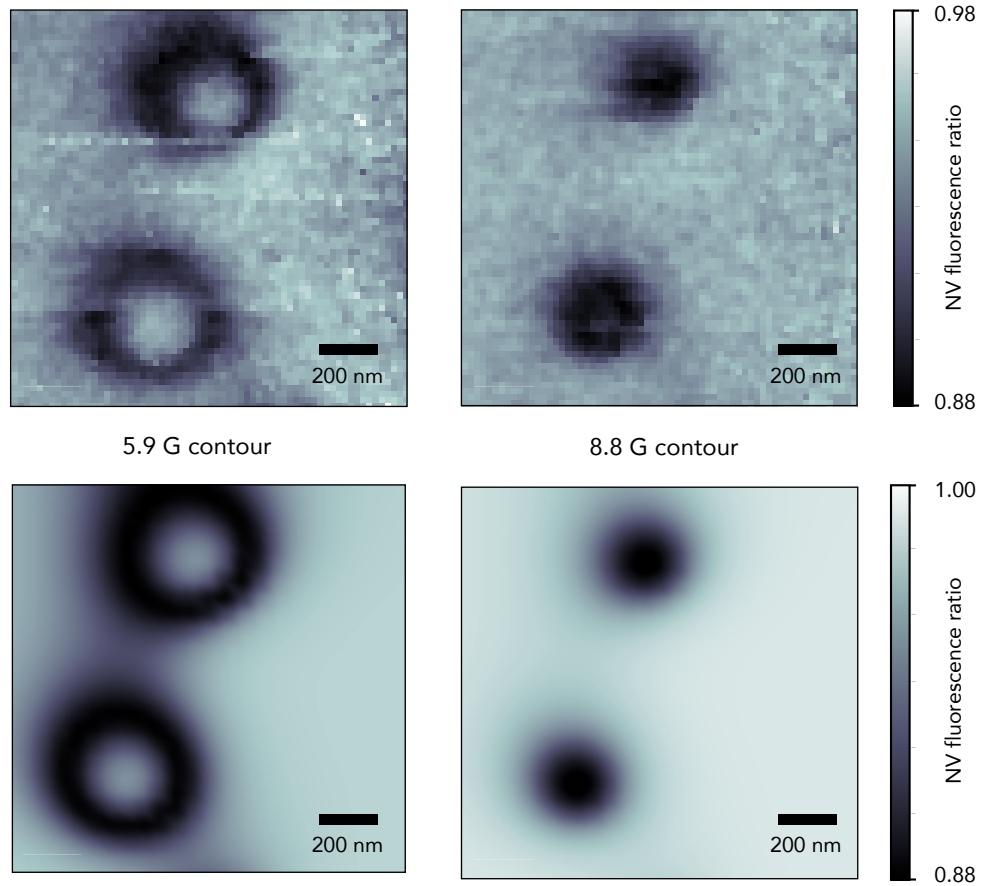
Figure 3.22: (a), (b), Magnetic images corresponding to the 5.9 G (a) and 8.8 G (b) contours of constant magnetic field. The sample was cooled in a 10 G field applied perpendicular to the sample through the superconducting transition at $T_c = 30$ K to form vortices. The dark circular features indicate the location of the vortices. (c), (d), Simulated field contours at 5.9 G (c) and 8.8 G (d) from a vortex pair as measured by an NV center located 330 nm above the surface. λ is assumed to be 200 nm in the simulation, with the NV center oriented along the $\langle 111 \rangle$ axis of the $\langle 100 \rangle$-cut diamond tip. The elongation of the vortex contours in (a) and (c) is a consequence of the stray field from adjacent vortices and the non-orthogonal orientation of the NV with respect to the sample plane.

Chapter 4

Magnetic skyrmions

In this chapter, I will highlight our work using scanning NV magnetometry to study magnetic skyrmion systems. Much of this chapter is based on these two papers [81, 82].
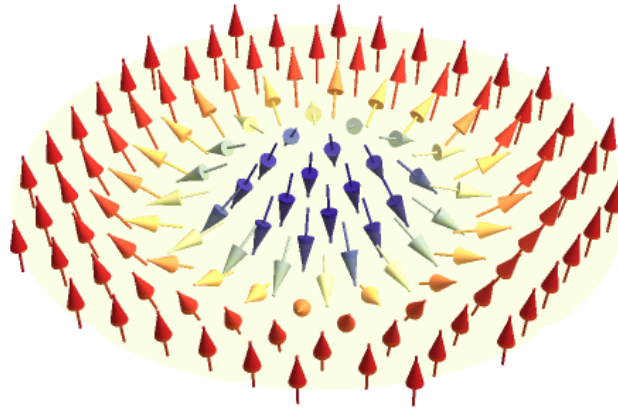

Figure 4.1: Magnetization pattern of a Néel-type skyrmion.

Magnetic skyrmions are solitonic spin textures with non-trivial topology. They were first discovered in non-centrosymmetric bulk crystals and ultrathin epitaxial magnetic layers [83–86]. The skyrmions observed in those materials had nanoscale sizes and large current-driven velocities, leading to their identification as promising candidates as carriers of information in future high-density, low-power electronics [87–90].

Magnetic skyrmions are usually comprised of a large number of spins. This is true

even of the small, sub-10 nm skyrmions, like those in single layer of Fe atoms grown on $\langle 111 \rangle$ Ir which still contain several hundred spins [91]. This means they can be well described with continuum micromagnetic models. Their topological structure can be defined in terms of an integer winding number,

$$N = \frac{1}{4\pi} \int dx \, dy \, \mathbf{m} \cdot \left(\frac{\partial \mathbf{m}}{\partial x} \times \frac{\partial \mathbf{m}}{\partial y} \right) \tag{4.1}$$

where $\mathbf{m}$ is the unit magnetization vector, $\mathbf{m}(x, y, z) = \mathbf{M}(x, y, z)/M_s(x, y, z)$. This 2D integral describes the winding number of a 2D magnetic patterns, or a slice through a magnetic pattern with translational symmetry in a direction pointing out of the $x - y$ plane, like the skyrmion tubes in bulk systems.

On the other hand, the discreteness of the magnetic pattern does have important implications for the stability of a magnetic skymrion. The stability of magnetic skyrmions results from the combination of a non-trivial topological structure and the stiffness of the magnetization field (although the topology may be less important than implied by the terminology commonly used to describe skyrmions [92]). For example, one could imagine unwinding the skyrmion shown in Fig. 4.1 by continuously deforming the structure to squeeze the skyrmion until there is a singularity of downward pointing magnetic moments at the center of the original skyrmion. At some point during this deformation, the magnetic pattern will cross over an energy barrier and the remaining downward pointing spins will prefer to flip, resulting in a saturated ferromagnetic state. The important point is that this energy barrier is finite. The energy cost to deform the magnetic structure in this way is some function of the Dzyaloshinskii-Moriya interaction (DMI) strength D, the magnetic exchange stiffness A_{ex}, and dipolar interactions integrated over the volume of the skyrmion. For a skyrmion stabilized by the DMI, the energy cost to deform the magnetic structure would depend more on the DMI strength D and the magnetic

exchange stiffness A_{ex}. For bubble skyrmions (stabilized by dipolar interactions), like those described in section 4.2, this energy barrier would depend more critically on the exchange stiffness and dipolar interactions. The energy barriers described in this way apply to the magnetic patterns in the skyrmion phase, where the external magnetic field is tuned so that the skyrmions are happy, as skyrmions can be destroyed by applying a large enough magnetic field.

4.1 Thin film heterostructures

Following the initial discovery of skyrmions in non-centrosymmetric bulk crystals, much interest has focused on the creation of related magnetic structures in sputtered thin film multilayers [93–96]. These multilayer materials are promising for making practical skyrmion devices, because of their capacity for commercial scaling and the ability to easily tune different magnetic interactions that determine the skyrmion phase temperature, field, size, and current-driven behavior. But further materials development is required to achieve the 10 nm-scale and efficient current-driven motion desired for applications [97].

In these thin film structures, an interfacial DMI arises from inversion symmetry breaking at the interface of a magnetic layer and a metallic layer with large spin-orbit coupling. The shape anisotropy of the thin film is usually overcome by including perpendicular magnetic anisotropy (PMA) in the system, for example by coupling a MgO layer to the magnetic layer. For film thicknesses much smaller than any of the magnetic length scales, these systems can be described by a micromagnetic free energy [98, 99],

$$F = t \int dx \; dy \; \left\{ A \left(\sum_i (\nabla m_i)^2 \right) - K m_z^2 - \frac{\mu_0 M_s}{2} \mathbf{m} \cdot \mathbf{H_d} \right.$$
$$\left. + D \left(m_z \left(\partial_x m_x + \partial_y m_y \right) - \left(m_x \partial_x + m_y \partial_y \right) m_z \right) \right\} \tag{4.2}$$

for a film thickness t, magnetic exchange J, normalized magnetization components $m_i = M_i/M_s$, PMA strength K, demagnetization field $\mathbf{H_d}$, and DMI strength D.

4.1.1 Ta/CoFeB/MgO

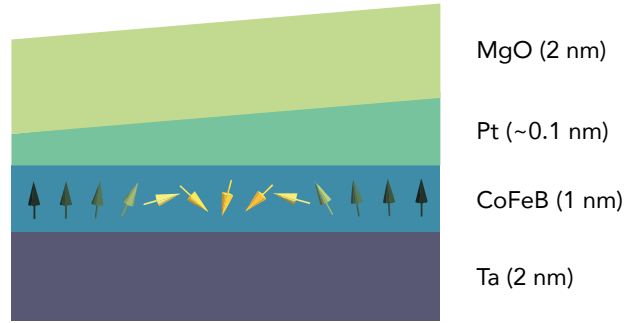MgO (2 nm)

Pt (~0.1 nm)

CoFeB (1 nm)

Ta (2 nm)

Figure 4.2: Structure of the Ta/CoFeB/MgO system.

In the Ta/CoFeB/MgO thin film system, shown in Fig. 4.2, PMA due to the CoFeB/MgO interface allows for the existence of magnetic bubbles stabilized under a small magnetic field perpendicular to the film. An interfacial DMI arising from an antisymmetric exchange coupling at the interface of the ferromagnetic CoFeB and strong spin-orbit Ta layers encourages a fixed chirality of the magnetization structure of these bubbles. A wedged sub-nm Pt insertion layer between the CoFeB and MgO tunes the PMA strength by weakening Co-O and Fe-O bonds at the MgO interface. This Pt insertion layer also induces a DMI at the top CoFeB interface, modifying the total DMI strength [100–102]. A magnetic field B_{ext} is applied perpendicular to the sample plane giving rise to isolated skyrmions in certain regions of the PMA-B_{ext} phase space [94]. The NV fluorescence images in Fig. 4.3 show the evolution of the magnetic order with B_{ext}. At $B_{ext} = 0$, magnetic order takes the form of stripe-like domains. As B_{ext} is increased, the system undergoes a first order phase transition into a skyrmion phase. In Fig. 4.3, a coexistence of skyrmion bubbles and stripes is seen already at 3 Oe, and several bubbles

persist up to $B_{ext} = 9$ Oe. At fields larger than 10 Oe, the material transitions into a ferromagnetic phase with no magnetic features in the NV images. The images in Fig. 4.3 were obtained using the contour imaging method, with the frequency of the applied microwaves fixed to the NV zero-field splitting frequency of 2.870 GHz. For the small values of B_{ext} used, the dark contours mark the approximate domain wall positions, with a small (< 100 nm) scale offset in the direction of the NV's in-plane projection (supplementary section S1). The width of the contour lines, which can be much smaller than the NV-sample separation, is determined by the width of the NV ESR dip and the magnetic field gradients near the domain walls [30].
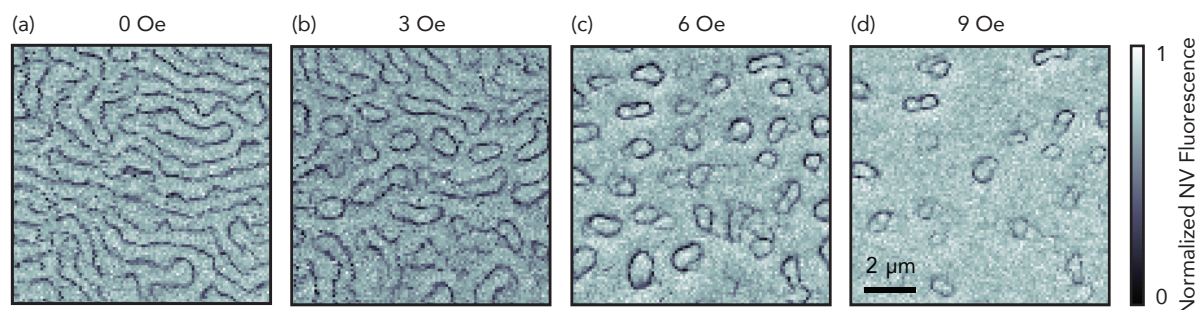

Figure 4.3: Field contour images of magnetic phases in Ta/CoFeB/MgO system acquired with the NV microscope. The applied microwave frequency is 2.870 GHz for all images. An external magnetic field applied normal to the sample plane is increased from 0-9 Oe in (a)-(d). As the field increases, the magnetic order evolves from stripes at 0 Oe (a) into a mixed skyrmion/stripe phase at 3 Oe (b) and a skyrmion phase at 6 (c) and 9 (d) Oe. At these fields, zero-field contours mark the approximate domain wall positions. The scale bar for all images is shown in (d).

4.1.2   IrMn/CoFeB/MgO

We also studied a related system, Ta (2 nm) / $Ir_{22}Mn_{78}$ (5 nm) / $Co_{20}Fe_{60}B_{20}$ (~ 1 nm wedged) / MgO (2 nm) / Ta (2 nm), in which the antiferromagnetic IrMn coupled to the ferromagnetic (FM) CoFeB layer produces an exchange bias. This interaction is thought to be caused by uncompensated, pinned spins in a small layer at antiferromagnetic-

ferromagnetic interface [103, 104]. The effect of exchange bias is to add an effective magnetic field to the ferromagnetic layer, shifting the magnetic hysteresis loop along the H-axis. In a skyrmion system, this means that a magnetic skyrmion phase can potentially be stabilized at zero external magnetic field.

Figure 4.4 shows scanning NV measurements of the IrMn/CoFeB system. In this structure the PMA is controlled with a wedged CoFeB layer instead of the wedged Pt insertion layer described above. Figure 4.4(b) shows a full-field image of the stray field emanating for an isolated magnetic bubble at zero field. Using this image, and measurements of the material parameters, the helicity angle of the magnetic structure can be extracted, as described for Ta/CoFeB/MgO in the next section. However, in this case, the sign of the DMI interaction extracted from the reconstruction (right-handed) disagrees with the sign measured by Brillioun light scattering (BLS), and that indicated by the current driven motion of the material's domain walls. The most likely culprits for this disagreement are a systematic error in the NV height measurement, or local variation in the material parameters at the strongly pinned domain walls. This highlights the fact that the magnetic structure reconstruction using NV magnetometry depends sensitively on the models and material parameters used in the reconstruction. And it further emphasizes the fact that investigating materials with complimentary techniques can reveal different information about the local vs. averaged bulk structure. The reconstruction for Ta/CoFeB/MgO in the next section gives a DMI sign that agrees with the BLS measured sign, but still has some discrepancy in the strength D, possibly due to the local vs.bulk nature of the two measurements.

Figures 4.4(c) and (d) show the zero-field magnetic order for two different magnetic histories. The image in Fig. 4.4(d) was taken after that in Fig. 4.4(c), following a cycling of the magnetic field applied along the film normal to 120 G and back to 0 G. The magnetic history prior to Fig. 4.4(c) was not carefully controlled.
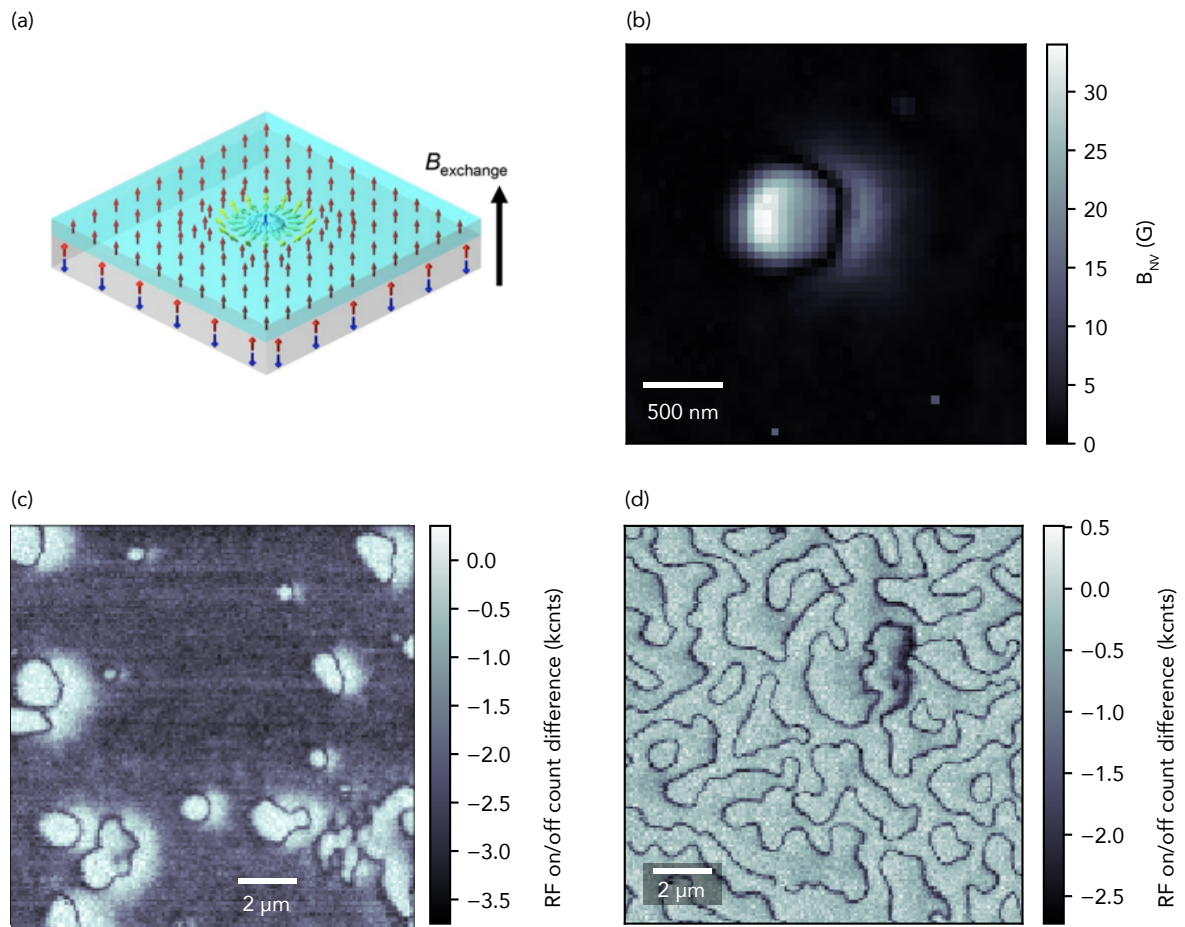
Figure 4.4: Scanning NV magnetometry of IrMn/CoFeB/MgO. (a) Exchange bias arising at interface of the antiferromangetic IrMn and ferromagnetic CoFeB creates an effective external field, stabilizing mangetic bubbles even when no external field is applied. (b) Full-field NV image of an isolated magnetic bubble at zero external field. (c), (d) Contour images of magnetic structure at zero external magnetic field. The magnetic pattern is striped or has isolated bubbles, depending on the history of the external magnetic field.

4.2   Probing structure and dynamics

Switching back to Ta/CoFeB/MgO, the high resolution of the NV center scanning microscope allows for the study of the microscopic structure of these bubble domains [28, 66]. For example, contour images of domain wall position show the effects of pinning sites on skyrmion shape (Fig. 4.5a), which induce both a static deformation of the skyrmion as well as a dynamic instability. Figures 4.3c-d and the higher resolution contour images in Fig. 4.5a-g show irregularly shaped skyrmions, whose dramatic deviation from a disorder-free, circular shape is consistent with previously reported NV-microscopy images of a similar thin film magnetic multilayer [68]. The effect of pinning sites is also manifest in the evolution of skyrmion size and shape with magnetic field, as shown in Fig. 4.5. When B_{ext} is increased from 5 to 7.5 Oe the skyrmion shrinks, as seen by comparing Fig. 4.5a and 4.5f and as predicted by micromagnetic theory [105]. Interestingly, however, this process does not happen smoothly but rather discontinuously: at intermediate fields in the range of $B_{ext} = 6.0$–7.5 Oe, the images in Fig. 4.5(b-e) show domain wall contours corresponding to both the larger and smaller diameter skyrmion. As the field is increased, the contrast of the larger diameter contour progressively decreases while the contrast of the smaller diameter contour increases. This behavior is explained by the domain wall hopping back and forth in time between two stable positions, progressively spending a larger fraction of its time in a smaller diameter configuration as the field is increased. Hopping that occurs on a timescale faster than the NV measurement leads to a reduction in the contrast of the contours because the NV fluorescence signal is averaged over its bright and dark states as the fluctuating field produced by the hopping domain wall brings the applied microwaves on and off resonance with the NV ESR transitions. Thus, although our measurement is too slow to detect the telegraph nature of the domain wall hopping in real time, we can detect time-averaged signatures of the dynamics through
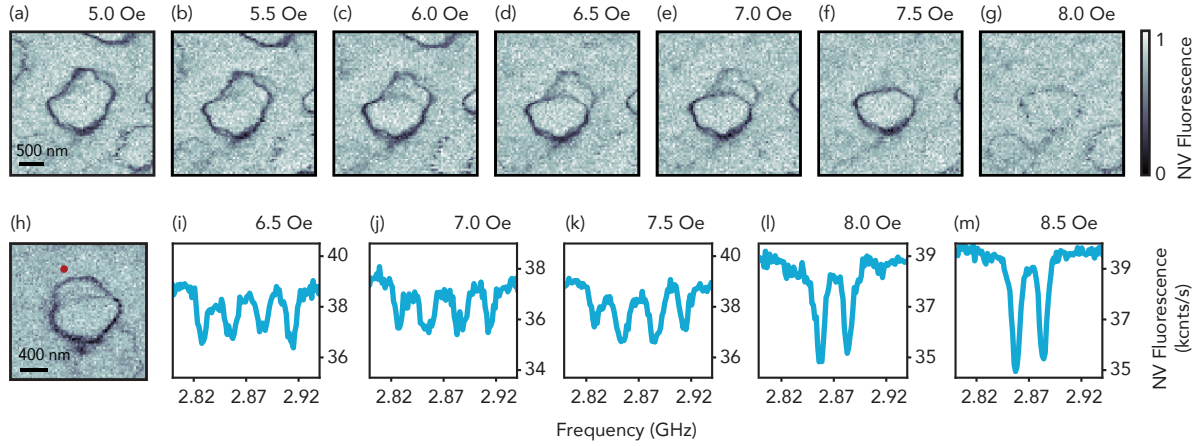
changes in contour contrast.

Figure 4.5: Domain wall fluctuations and evolution with B_{ext} imaged by NV center microscopy. (a) 2.870 GHz contour images of a skyrmion bubble, each labeled by the corresponding B_{ext} applied during that scan. As B_{ext} increases, a section of the domain wall evolves into a bistable configuration, seen most clearly in the (d) and (e) scans with 6.5 and 7.0 Oe. The scale bar for (a)-(g) is shown in (a). (h) 2.870 GHz contour images of another skyrmion bubble taken at $B_{ext} = 7.0$ G. (i)-(m) NV center ESR spectra taken with the NV fixed at the location indicated by the red dot, each labeled by B_{ext}. The multiple pairs of ESR splittings in each spectrum correspond to different positions of the domain wall.

We can confirm the time-averaged behavior of the domain wall fluctuations by fixing the NV at a location near a fluctuating domain wall while recording the ESR spectrum, as shown in Fig. 4.5(i-m). The position of the NV is indicated by the red dot in Fig. 4.5h. In the spectrum, the hopping of the domain wall appears as two dominant ESR splittings that emerge as the magnetic field is swept through the skyrmion phase. When the domain wall is near the NV, the ESR splitting is largest, given by the outer two ESR dips. The existence of other ESR dips in the spectra in Fig. 4.5 implies that the domain wall spends some time at another position, seen as the faint contour line cutting across the middle of the bubble in Fig. 4.5h. Qualitatively, the evolution of the contrast ratio between different pairs of dips in the ESR spectrum or equivalently, between domain wall branches in the contour images, gives an indication of the relative

time spent in different domain wall states. As B_{ext} is increased, the outer pair of ESR dips grows fainter as the domain wall evolves from spending more time in the larger skyrmion diameter configuration (near the NV) to spending more time in the small diameter configuration. At $B_{ext} = 8.5$ Oe, the skyrmion bubble is no longer stable and the ESR splitting is given by the NV-axis projection of B_{ext}.
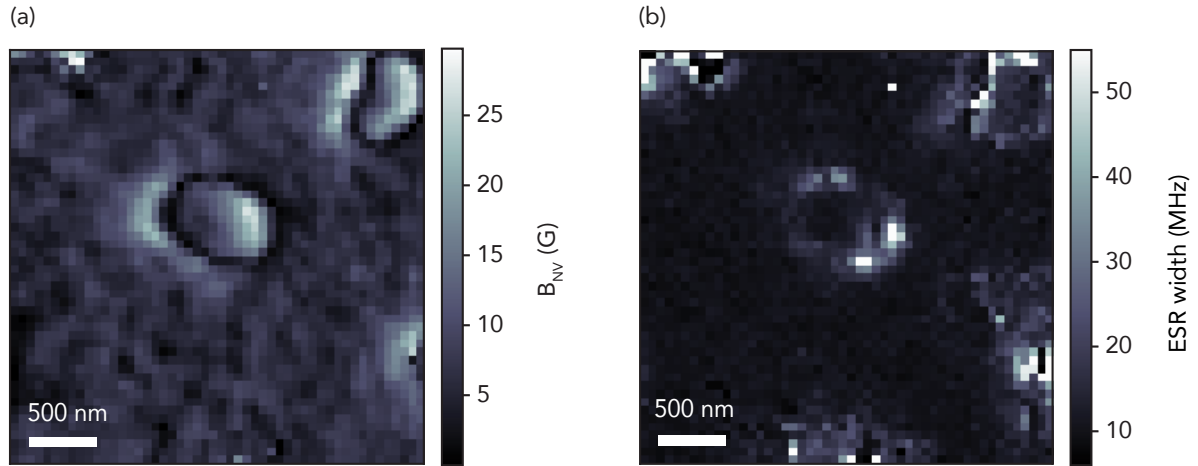

Figure 4.6:   Enhanced magnetic fluctuations near skyrmion domain walls (a) Spatial map of the magnetic field along the NV axis. The external field, $B_{ext} = 9.5$ Oe, is normal to the film plane. (b) NV ESR width averaged over both ESR dips, showing enhanced magnetic fluctuations at the skyrmion domain wall.

Importantly, our NV imaging technique allows us to glean quantitative information about the time scale of the domain wall dynamics. We estimate the average hopping rate, χ, of the domain wall in Fig. 4.5h to lie in the range of tens of Hz to tens of MHz by making the following two observations. First, telegraph switching of the NV fluorescence rate was not observed on time scales slower than 0.01 seconds, putting a lower bound on χ. In this experiment, we could not explore faster time scales because of insufficient signal to noise ratio for smaller measurement time bins. An upper limit on the characteristic hopping frequency can be set by treating the domain wall position between the two pinning sites as a quasi-1D system and assuming that the dynamics is governed

by an Arrhenius type thermal activation of hopping between two sites [106], where the number of domain wall jumps in a given time is described by a Poisson process. In this case, the NV ESR spectrum is expected to take two different forms, displaying either a single resonance line or a split pair of resonance lines for each spin transition, depending on the characteristic rate of domain wall hopping χ and the corresponding spectral shift of the NV ESR dip. Focusing on one NV spin transition, for example $|m_s = 0\rangle \rightarrow |-1\rangle$, the spectral shift can be written as $\Delta f_{ESR} = f_{DW2} - f_{DW1}$, where f_{DW1} and f_{DW2} are the NV resonance frequencies corresponding to the two domain wall positions. In the limit $\Delta f_{ESR} > \chi$, distinct resonances will be observed at f_{DW1} and f_{DW2}, whereas in the limit $\Delta f_{ESR} < \chi$, an effect similar to motional narrowing will give a spectrum with a single resonance at $(f_{DW2} + f_{DW1})/2$ if, on-average, an equal amount of time is spent in both domain wall positions [107, 108]. The distinct ESR lines shown in Fig. 4.5i indicate that the first limit applies and that the characteristic frequency of the observed domain wall hopping is limited to $\chi < 20$ MHz. This reasoning can also be applied to other observed bistable skyrmion bubble walls, for example those shown in Fig. 4.5c-e. Assuming that these domain wall branchings are due to a similar hopping mechanism as observed in Fig. 4.5h and 4.5i, the fact that two domain wall positions are observed in Fig. 4.5c-e can be used to place a rough limit on the timescale of those domain wall dynamics as well.

In addition to large jumps of domain wall position that produce a discrete set of ESR splittings, we also observe magnetic fluctuations that broaden the NV spin transitions when the NV is positioned near domain walls. Fig. 4.6b shows a spatial map of the average ESR width with corresponding stray field measurement in Fig. 4.6a. Figure 4.6b shows that magnetic fluctuations are enhanced near the skyrmion bubble walls, even in the absence of the clear bistabilities seen in Fig 4.5. We note that this broadening is not due to fluctuations in the NV-domain wall distance in regions of high magnetic fields gradient, as it is not observed near other sharp magnetic features not associated

with bubble domain walls (supplementary section S3). The emergence of these enhanced fluctuations near domain walls is not well understood and can be interpreted in a few ways. It could imply the existence of small fluctuations in the position of all domain walls, driven thermally or magnetically [109], possibly by the applied microwaves or laser light [33]. Alternatively, the spatial dependence seen in Fig. 4.6b could be the result of amplification or concentration of magnetic noise sources, such as spin waves, near the domain walls [110, 111]. We note that the increase in magnetic noise at the bottom of Fig. 4.6b is due to fluctuations of another bubble skyrmion whose dominant domain wall position is not seen in Fig. 4.6a (see supplementary section S4).

We have also observed switching dynamics between a bubble skyrmion state and a saturated ferromagnetic state, with a time scale slow enough to be observed in real time with the NV center. Figure 4.7a shows a skyrmion bubble contour ($B_{ext} = 9.2$) that becomes unstable as the field is increased to 9.5 G, as seen in Figs. 4.7b-c. Figure 4.7b shows a decrease in contour contrast due to switching between the bubble state and saturated ferromagnetic state. The switching dynamics can be directly observed as telegraph noise in the NV fluorescence time trace shown in Fig. 4.7c, obtained by fixing both the NV location (red dot in 4.7b) and the microwave frequency. High fluorescence corresponds to the ferromagnetic state and low fluorescence corresponds to the bubble state. The characteristic switching frequency can be extracted from the distributions of dwell times in each state. From a 30 second fluorescence trace, a characteristic switching frequency of 14 Hz is measured for both directions of state switching, implying that the energy of the two states is approximately equal at the applied field of $B_{ext} = 9.5$ G. The switching frequency is ultimately determined by the energy barrier between the bubble and saturated magnetic states. These energy barriers have been estimated previously for DMI-stabilized thin-film skyrmions [92], and the process of skyrmion collapse to a helical state has been explored in a bulk skyrmion system [112]. In the present case, the bubble is

dipole stabilized and the energy barrier can be estimated by a cylindrical bubble domain model [113]. Using an Arrhenius description of the switching, $f = f_0 \exp(-E_B/k_B T)$, where $E_B \simeq 240$ meV is the energy barrier in the bubble domain model, $T = 298$ K, $f = 14$ Hz is the characteristic switching frequency, the attempt frequency f_0 is determined to be $\simeq 0.35$ MHz. We note, however, that local material variations may alter the energy barrier.
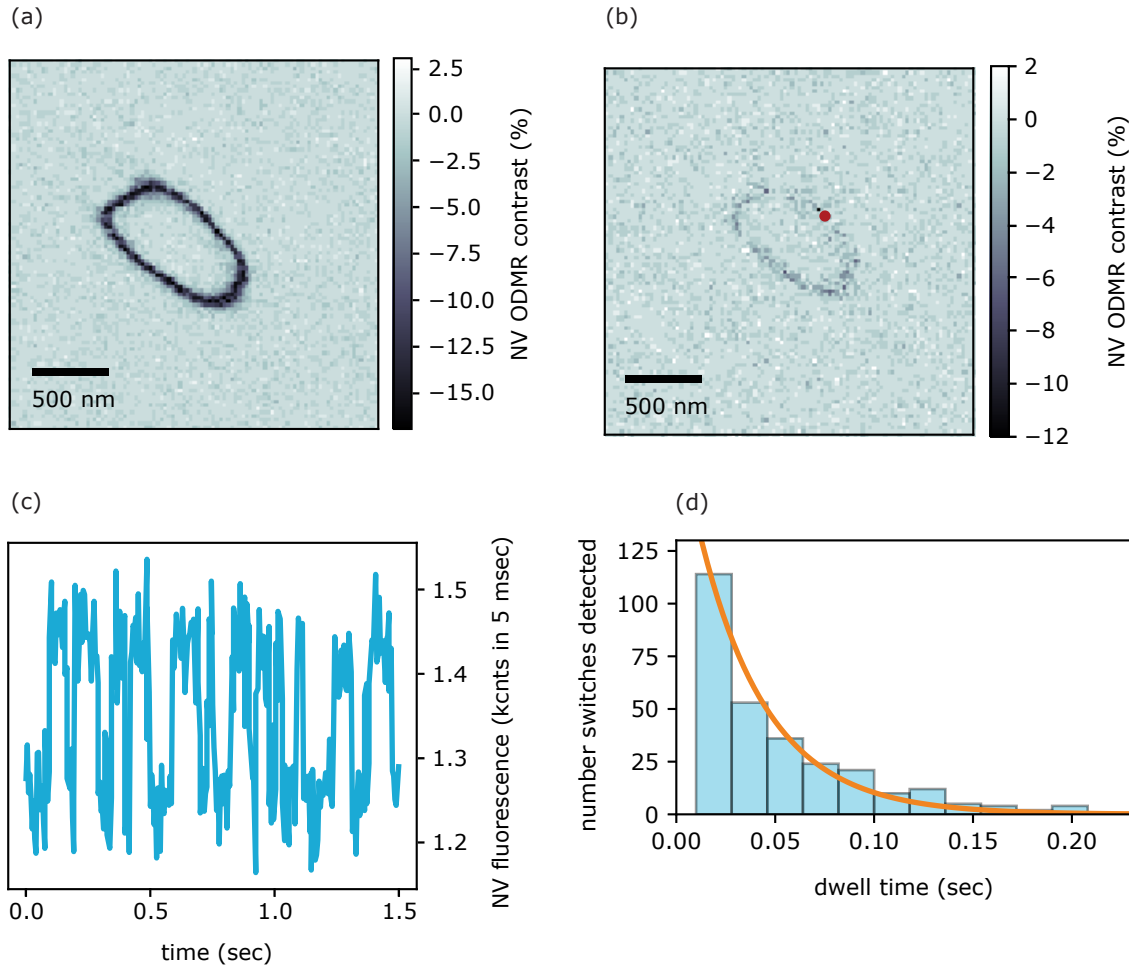
(a)

(b)

(c)

(d)

Figure 4.7: Telegraph switching of the NV fluorescence signal in the presence of a skyrmion bubble switching between a bubble and a saturated state. (a) 2.870 GHz contour image of the skyrmion bubble shown in Fig. 4.6 taken at $B_{ext} = 9.2$ G. (b) 2.870 GHz contour image of the skyrmion bubble shown in Fig. 4.6 taken at $B_{ext} = 9.5$ G. As the field is increased, the bubble state becomes unstable and switching between the saturated and bubbles states is observed as a decrease in the NV ESR contrast. (c) The ESR signal when fixing the NV position at the location indicated by the red dot in (b) with $B_{ext} = 9.5$ G. (d) The NV fluorescence collected in 5 ms bins when fixing the NV location at the position indicated by the red dot in (b), and fixing the drive microwave frequency at 2.871 GHz (the frequency indicated by the dashed red line in (c)). A characteristic hopping frequency of 14 Hz is measured over the full 30 second measurement window. (d) The distributions of dwell times in the saturated state, measured for a 30 second time trace of the NV signal in the presence of telegraph switching between the two magnetic states. The orange curves are exponential fits to the dwell time distribution, giving a characteristic time of $\sim$14 Hz. The distribution of dwell times in the bubble state is similar.

4.2.1   Magnetic structure

The magnetic structure of skyrmions has important implications for the viability and design of skyrmion-based devices because the structure determines important parameters of current-driven skyrmion motion, such as the skyrmion Hall angle and velocity [114–117]. However, probing the structure of skyrmion bubbles is difficult due to the required nanometer-scale resolution. While many techniques can be used to determine domain wall structure in principle, there are few examples of probes that are local, non-invasive, and capable of studying a wide range of skyrmion materials. Recent NV imaging studies of magnetic thin films have established scanning NV microscopy as a useful probe of magnetic structure with all these features [28, 65, 66, 118]. Starting from a map of the NV-axis stray field (Fig. 4.11a), a partial reconstruction of the magnetization structure is possible but requires knowledge of several material parameters, careful calibration of the NV scan height (Appendix D), and some structure assumptions based on micromagnetic theory.
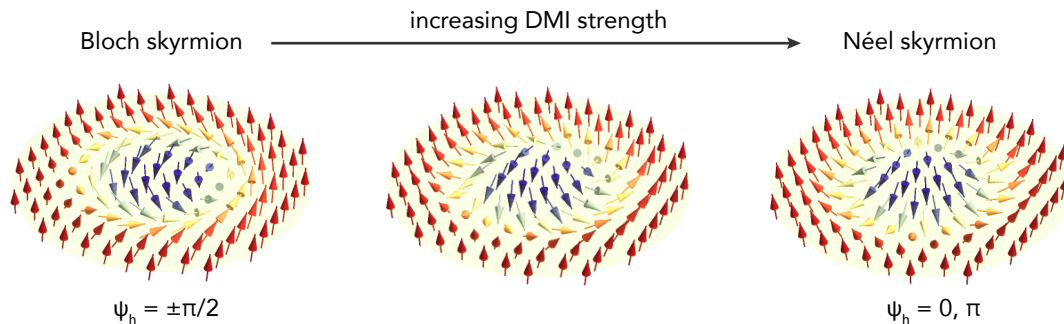

Figure 4.8: The structure of a thin-film bubble skyrmion depends on the DMI strength relative to the dipolar energy scale. For small D, the structure of domain walls will be Bloch type (left). As D is increased, the in-plane angle of magnetization inside the domain wall will evolve, approaching the domain wall normal as D approaches a critical value $D_c = 2\ln(2)\mu_0 M_s^2 t/\pi^2$.

The first step is to determine all the relevant materials parameters, leaving free only the absolute value of the domain wall helicity angle $|\psi_h|$. The helicity angle sets the

rotation direction of magnetization through a cross-section of the domain wall— here defined relative to the common domain wall types as $|\psi_h| = 0, \pi/2$, and π for right-handed Néel, Bloch, and left-handed Néel respectively (see Fig. 4.8). With this approach we can use the local, nanoscale nature of the NV probe to search for variations in the helicity angle magnitude along the skyrmion domain wall, which allows us to check for a fixed chirality of individual bubbles.

The required material parameters are M_s, t, and domain wall width Δ_{DW}, and we assume an analytic form (see section E.2) for the domain wall profile. The domain wall position is also needed and is given by the NV images. To estimate Δ_{DW}, which cannot be measured directly with our NV center for lack of spatial resolution, we combine bulk measurements of the effective magnetic anisotropy energy density K_{eff} and the magnetic surface density $I_s = M_s t$ with NV measurements of the domain wall energy density γ_w.
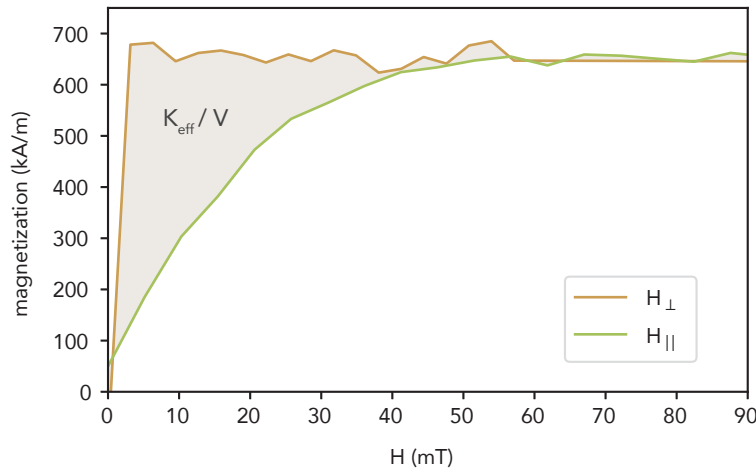

Figure 4.9: SQUID measurement of the saturation magnetization, M_s, and perpendicular magnetic anisotropy, K_{eff}. The sample magnetization is measured as a function of external magnetic field, applied normal to the film plane (orange) and parallel to the film plane (green). The total sample moment is measured, and the magnetization is calculated assuming a CoFeB thickness of 1 nm. The shaded area between the parallel and perpendicular curves is $K_{eff}/$(sample volume).

The parameters K_{eff} and M_s are calculated from hysteresis curves obtained with a

Quantum Design MPMS 5XL SQUID. The magnetic moment is measured as a function of an applied field both parallel and normal to the film plane (Fig. 4.9). After dividing the measurement magnetic moment by the thin film volume, M_s is the saturation value, while K_{eff} is given by the area between the parallel and normal curves [119]. These measurements give $I_s = (6.5 \pm 0.1) \times 10^{-4}$ A, where the uncertainty is given the standard deviation of the saturated SQUID value. This gives $M_s = 6.6 \times 10^5$ A/m and $K_{eff} = 8.3 \times 10^3$ J/m^3 for a film thickness $t = 1.0$ nm. Calculating the uncertainty in M_s and K_{eff} is trickier because their values depend on the film thickness t. The value of t used in these calculations is given by the measured deposition thickness, but we note that magnetic dead layers have been observed in CoFeB films at Ta or MgO interfaces [120,121]. A non-zero dead layer thickness would lead to different values of M_s and K_{eff} and differences in the magnetization reconstruction.

Armed with values of M_s and K_{eff}, it is possible to measure the domain wall energy density γ_w from stripe-phase NV images. The NV scan can be used to calculate the demagnetization energy and total domain wall length in the image area. The domain wall energy density is then calculated based on an energy minimization that balances variation in the demagnetization energy and domain wall length measured for a particular imaging area [122]. Starting from a zero-field stripe image, a polarity ($\pm M_s$) is assigned to the two image regions (Fig. 4.10). The demagnetization energy E_{demag} in the imaged area is calculated with OOMMF [123] using mirror symmetric boundaries. The total length of the domain walls in this image L is also measured and both values are normalized by the image area A giving $E'_{demag} = E_{demag}/A$ and $L' = L/A$. The domain wall energy density can then be obtained as in [122] by calculating the variation of E'_{demag} and L'

with respect to the characteristic stripe periodicity p,

$$\gamma_w = -\frac{\partial E'_{demag}/\partial p}{t\partial L'/\partial p} \tag{4.3}$$

These variations in demagnetization energy and domain wall length with respect to stripe periodicity can be related to variations in these parameters under small changes in the lateral scale of the magnetic pattern. This is done by calculating the demagnetization energy and domain wall length with the pixels at actual size and at a slightly larger size. In this case the actual pixel size is $a = 100$ nm, and variation in pixel size is $\Delta a = 2$ nm. The variations with respect to periodicity and pixel size are related by the following,

$$\left.\frac{\partial E'_{demag}}{\partial p}\right|_a = \frac{1}{\partial p/\partial a}\frac{\partial E'_{demag}}{\partial a} \approx \frac{1}{\partial p/\partial a}\frac{E'_{demag}(a+\Delta a) - E'_{demag}(a)}{\Delta a} \tag{4.4}$$

and for a total domain wall length $L = Ma$, and total image area N^2a^2,

$$\frac{\partial L'}{\partial p} = \frac{1}{\partial p/\partial a}\frac{\partial L'}{\partial a} = \frac{1}{\partial p/\partial a}\frac{\partial}{\partial a}\left(\frac{Ma}{N^2a^2}\right) = \frac{1}{\partial p/\partial a}\frac{\partial}{\partial a}\left(\frac{M}{N^2a}\right) = \frac{1}{\partial p/\partial a}\frac{-M}{N^2a^2} = -\frac{1}{\partial p/\partial a}\frac{L'}{a} \tag{4.5}$$

This gives a domain wall energy density,

$$\gamma_w = \frac{\partial E'_{demag}/\partial a}{tL'/a} \tag{4.6}$$

and a calculation of the demagnetization energy variation and domain wall length for the image in Fig. 4.10 gives $\gamma_w = 1.3$ mJ/m^2. The domain wall energy density can be used
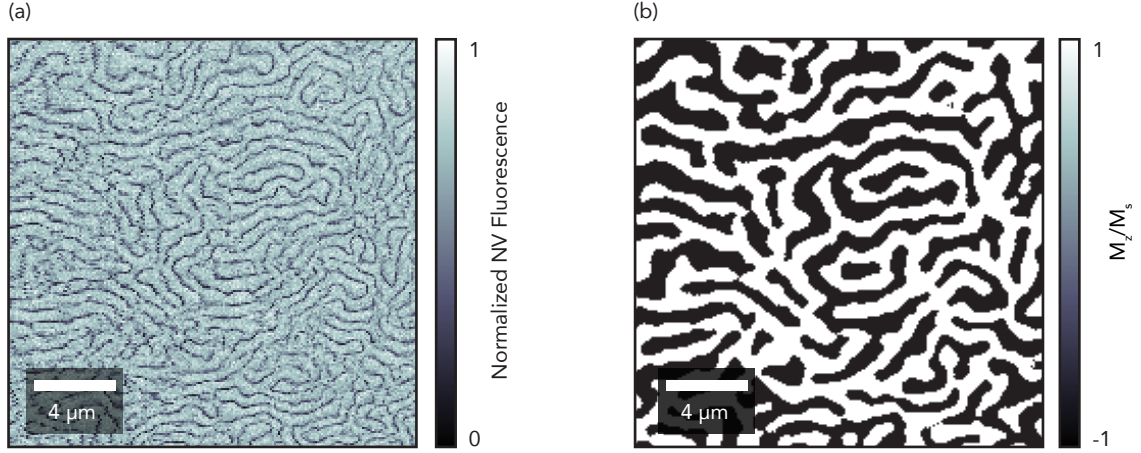
Figure 4.10: Stripe domains at zero external magnetic field. (a) Measured zero-field contours and (b) corresponding assigned magnetization used to calculate the demagnetization energy.

in turn to calculate A_{ex} and Δ_{DW}

$$A_{ex} = \frac{(\gamma_w + \pi D)^2}{16 K_{eff}} \tag{4.7}$$

$$\Delta_{DW} = \sqrt{A_{ex}/K_{eff}} \tag{4.8}$$

The DMI strength measured via Brillouin light scattering is found to be $D = 47$ µJ/m^2, giving an exchange stiffness $A_{ex} = 9$ pJ/m and domain wall width $\Delta_{DW} = 33$ nm. The extracted value of A_{ex} is in good agreement with the value measured with BLS. This method of estimating γ_w can be checked against an analytic form for parallel stripe domains [124]

$$\gamma_w = \frac{\mu_0 M_s^2 t}{\pi} \left(\ln\left(\frac{2L}{\pi t}\right) + \frac{1}{2} \right) \tag{4.9}$$

Identifying characteristic image length scale in the image Fourier decomposition, $L = 664 \pm 23$ nm. This gives a domain wall width $\Delta_{DW} = 35$ nm.

However, a non-zero dead layer thickness will alter either calibration of domain wall width. For example, assuming a dead layer thickness of 0.36 nm, similar to [120], the same analysis gives the parameters $M_s = 9.5 \times 10^5$ A/m, $K_{eff} = 1.2 \times 10^4$ J/m^3, $A_{ex} = 20$ pJ/m, and $\Delta_{DW} = 49$ nm.

4.2.2   Reconstruction

Now that we have the required material parameters, we start the magnetization reconstruction by assigning a polarity to regions of the B_{NV} map separated by zero-field contours. The polarity direction is determined by the direction of the applied external field. This signed field map can in turn be used to calculate the full vector components of the stray magnetic field [28, 125]. The z component of $\mathbf{B}$ (where $\hat{\mathbf{z}}$ is normal to the sample) at the sample surface can be extrapolated and used to estimate the domain wall position (Sec. E.2). The magnetization pattern $\mathbf{M}$ is then fully determined by the domain wall width Δ_{DW}, saturation magnetization M_s, and helicity angle magnitude $|\psi_h|$.

For NV-sample separations larger than Δ_{DW}, a direct measurement of Δ_{DW} is difficult and Δ_{DW} must be inferred from measurements of other parameters. As mentioned before, three parameters are required— M_s, PMA energy density K_{eff}, and domain wall energy density γ_{DW}. With these parameters, we can compare the expected stray field for a given helicity magnitude to that measured with the scanning NV center.

Figure 4.11b shows the best-fit simulated stray field corresponding to the measurement stray field in Fig. 4.6a. The best-fit helicity angle magnitude, $|\psi_h| = 58°$ is determined by minimizing the RMS error between the measured and simulated stray field, as a function of $|\psi_h|$, in a 1.4 μm box centered on the bubble. Values obtained for other skyrmions include $|\psi_h| = 72°$ and $75°$ (shown in Sec. E.2). To allow for the

possibility that the helicity angle can change locally along the bubble domain wall, it is instructive to compare the simulated stray field as a function of position along the domain wall. In Fig. 4.11a, linecuts across the measured and simulated field images are shown as a function of cut angle and helicity type. The skyrmion bubbles in this material consistently show a right-handed helicity angle. A constant right-handed helicity is consistent with a non-zero winding number, but it is important to note that uncertainties in sample thickness and NV height will change the measured helicity angle magnitude. The right-handed helicity observed here agrees with BLS measurements of D, but micromagnetic theory gives a smaller magnitude helicity angle based on the bulk material parameters and the measured D. This discrepancy between a bulk calculation and local measurements of the helicity angle may come from spatial fluctuations in the material parameters [126]. For example, we observe variations in the stray field measured in the saturated magnetic state (Fig. E.4), which we attribute to variations in the parameter $I_s = M_s t$. The domain wall energy density is lowered in areas where the film is thicker or M_s is larger, and the domain walls will likely be pinned in these areas. Since the helicity angle depends on M_s and t this effect will lead to a different helicity angle calculated from bulk measurements of M_s, t, and D and the helicity angle measured locally at the domain walls.
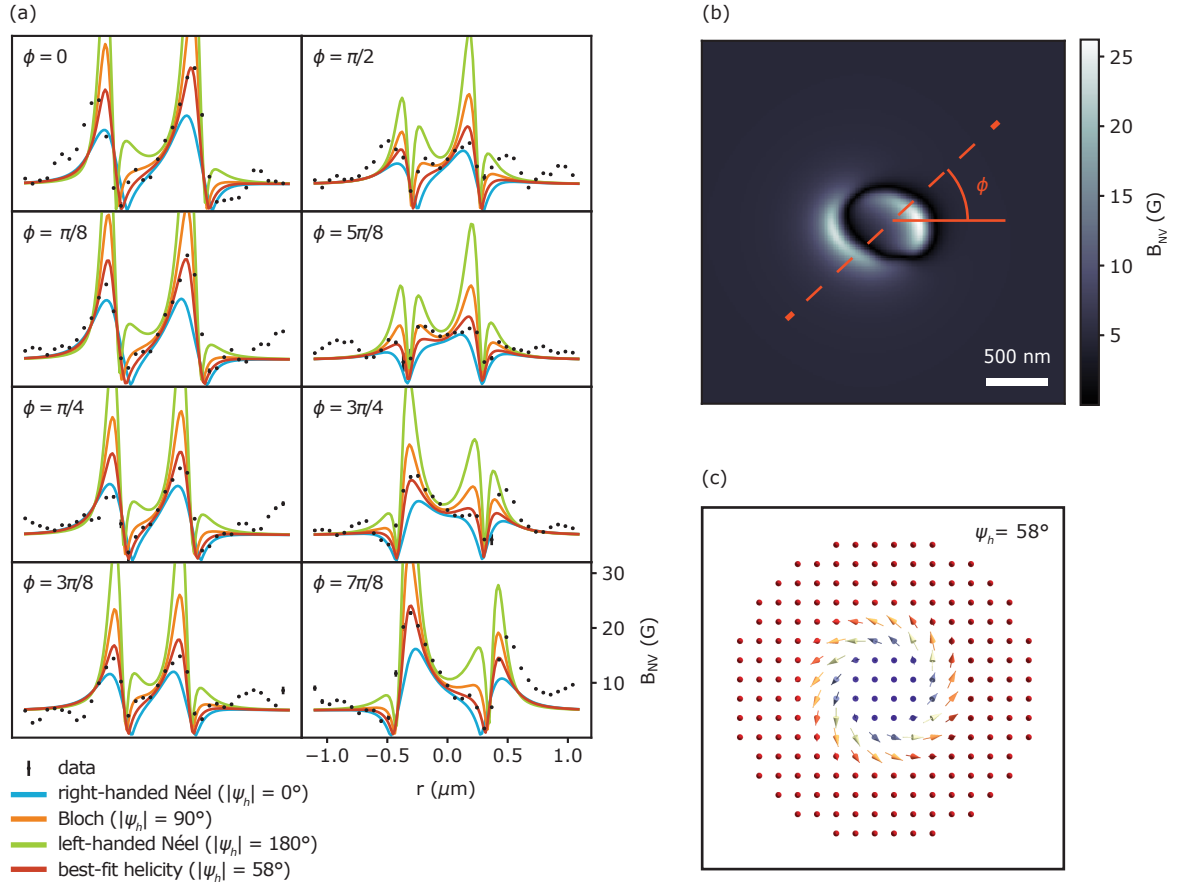
Figure 4.11: Reconstruction of helicity angle. (a) Linecuts at various angles ϕ across a magnetic bubble, comparing the measured magnetic field shown in Fig. 4.6a to the simulated field for four domain wall types— right-handed Néel, Bloch, left-handed Néel, and a domain wall with $|\psi_h| = 58°$. The NV height is calibrated to be 58 ± 5 nm using the method described in Appendix D. The NV angle relative to the film normal is measured as $60° \pm 4°$ using an external field aligned along the film normal. The in-plane NV angle is extracted from the B_{NV} bubble image by finding the direction of maximum field gradient at the domain wall and is $16° \pm 2°$ relative to the image x-axis. (b) The simulated magnetic field along the NV axis for the best fit helicity angle $58°$. (c) Schematic of the magnetization of a skyrmion bubble with a fixed helicity angle $|\psi_h| = 58°$, viewed from above. The magnetization transitions from pointing upward outside the bubble (red) to pointing downward inside (blue) with a rotation direction between that of Bloch and Néel-type domain walls.

4.3   Future studies on strain in bulk skyrmion systems

Skyrmion systems in thin film heterostructures are desirable partly for their tunability. Various magnetic interactions in these systems can be tuned by changing layer thicknesses, or interfaces, or by making meta-materials consisting of many repeated layers of alternating heavy metals and magnetic films. Bulk, single-crystal skyrmion systems, on the other hand, can display favorable properties like low depinning currents and low disorder [127]. Although bulk systems do no have the same flexibility to easily tune magnetic structure through geometric and interfacial effects, there has still been much progress in tuning the magnetic phase diagrams of bulk systems through composition and structure. Since the initial discoveries of magnetic skyrmions in MnSi and FeGe, bulk skyrmion systems have been created with skyrmion phases at or above room temperature, a desirable property for making real devices [128, 129]. One way to extend the tunability of bulk skyrmion system may be through the use of coupling between strain and magnetism. Some preliminary studies have shown that the magnetic interactions involved in producing skyrmions can be tuned through the application of mechanical deformation [130, 131]. It is possible that strain may also be able to produce magnetic structures like skyrmions or magnetic helixes by break symmetries in materials that would ordinarily not host chiral magnetic order. A local probe like an NV is ideal for studying the interaction between strain and magnetism because it can probe how the length scales of magnetic structures change in various regions of a strained sample. Figure 4.12 shows initial measurements of a magnetic helix in a $Co_8Zn_9Mn_3$ sample at room temperature. This system is expected to host skyrmions at or near room temperature, depending on the composition [129], and is good candidate for studies of coupling between magnetic interactions and strain.
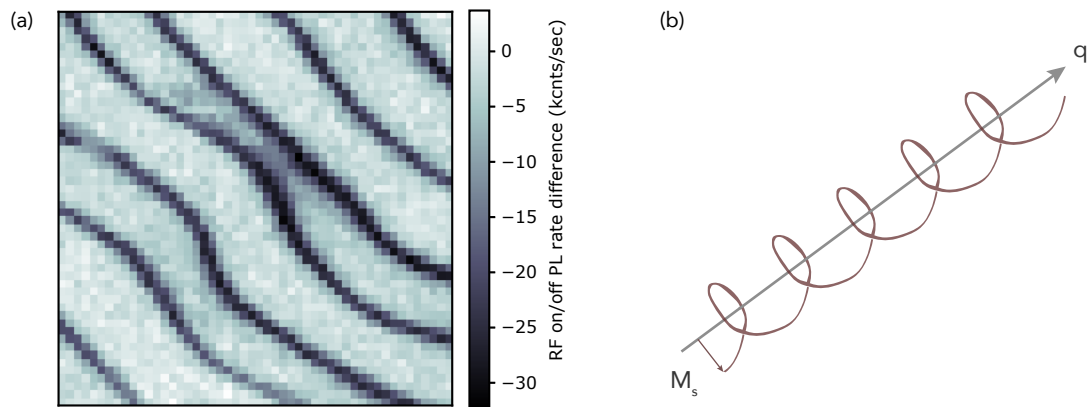
Figure 4.12: (a) Zero-field contour image of the stray field from a magnetic helix in $Co_8Zn_9Mn_3$. The microwave frequency is fixed to 2870 MHz, and the dark contours in the image correspond to zero magnetic field along the NV axis. There was no external magnetic field applied and the image was taken at 298 K. (b) Drawing of a magnetic helix. The magnetization vector rotates in a helical pattern, with a direction defined by the vector $\mathbf{q}$. In (a) $\mathbf{q}$ is pointed roughly parallel to the plane of the sample, resulting in a magnetic surface charge $\sigma \approx cos(\mathbf{q} \cdot \mathbf{r})$ for $\mathbf{r}$ on the surface.

Chapter 5

Searching for electron hydrodynamics in graphene

A hydrodynamic description is useful for understanding and describing systems containing many interacting particles. On long length scales and at long times scales (much larger than the typical interaction lengths and times of the individual particles) it is often possible to describe a many-body interacting system in terms of conserved continuum quantities like energy, momentum, and density. For strongly interacting systems with a macroscopic number of particles it makes sense to use a hydrodynamic description if we care about its behavior on those comparably long length and time scales. Historically, a hydrodynamic description hasn't been useful for electron fluids in solid-state systems. In most metallic systems, the momentum relaxing interactions of the electron fluid, due to scattering from impurities or phonons, dictate the macroscopic behavior of electron flow (ignoring exotic, low-temperature phases). In these cases, the best macroscopic description of the system is often given by Ohm's law $\mathbf{j}(\mathbf{r}) = \sigma \mathbf{E}(\mathbf{r})$ for current density $\mathbf{j}$, conductivity σ, and electric field $\mathbf{E}$. The scalar conductivity boils down all the details of the momentum relaxing interactions to a single number. At low temperatures, another well-known regime of current flow encountered in materials with high conductivity is the ballistic regime, in which the momentum relaxing scattering length scale is larger than

the sample geometry. In this regime, the current density is not locally related to the electric field through Ohm's law (on the scale of the sample geometry) and is determined by the sample geometry and the nature of scattering at the sample boundaries.

However, there do exist ultra-high conductivity electron systems, where due to low momentum relaxing scattering rates and strong electron-electron interactions, the short length scales of momentum conserving electron-electron scattering l_{ee} may play a role in determining the macroscopic behavior of the electron fluid. Some examples of these systems that have been studied experimentally are AlGaAs/GaAs heterostructures [132,133], delafossite-type crystals [134], and both mono- and bi-layer graphene [135,136]. Graphene serves as a test-bed of electron hydrodynamics, as it is a relatively simple and well-understood system that lends itself well to experimental searches of these hydrodynamic effects. A hydrodynamic description of solid-state electron systems may then find more practical utility in less tractable electron systems like strange metals [137]. The experimental probe of electron hydrodynamics described in this chapter may also prove useful in other areas, for example as a method for disentangling the electron-phonon vs. electron-electron origin of poorly understood transport signatures.

5.1   Graphene

Graphene is a 2D material made of a hexagonal lattice of carbon atoms, as shown in Fig. 5.1(a). The C atoms are bonded together with hybridized, in-plane sp^2 orbitals. This leaves one electron per atom in a p_z orbital, for z normal to the graphene plane. The electronic behavior of graphene is determined by the half-filled band formed by these p_z orbitals. It is well described by a tight binding model [138], that gives a linear dispersion relation near the corners of the Brilliouin zone [139], at the K and K' points (Fig. 5.1(b

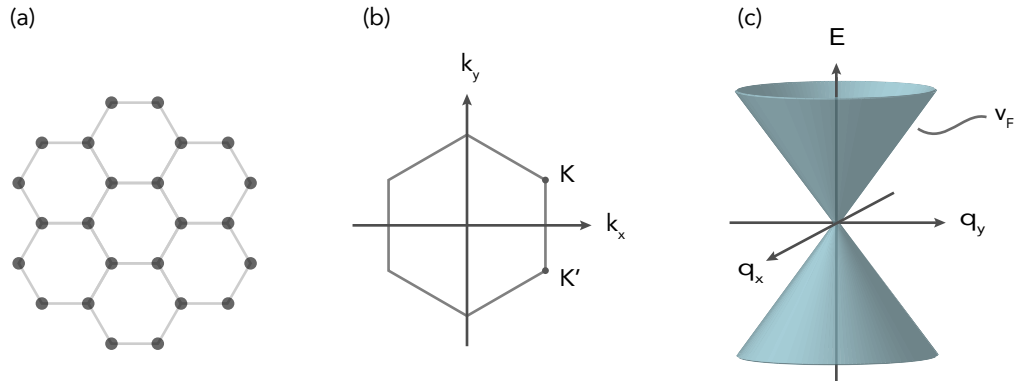(a)   (b)   (c)

Figure 5.1: (a) Graphene structure: a hexagonal lattice of carbon atoms. The C atoms are σ bonded together with overlapping sp^2 orbitals, leaving one free electron per C atom in a p orbital oriented perpendicular to graphene plane. (b) Brillouin zone of a hexagonal lattice. (c) Linear dispersion of the graphene band structure near the K and K' points of the Brillouin zone.

and c)),

$$E \simeq \pm v_F |\mathbf{q}| \tag{5.1}$$

with $\mathbf{q} = \mathbf{k} - \mathbf{K}$ being the wavevector displacement from the K or K' points. In the absence of doping or gating, the Fermi level of the half-filled band will sit at these K and K' points. At this point, the carrier density vanishes and the Fermi surface becomes a point. It is known as the charge neutrality point (CNP). The system is described by a linear dispersion over a large range of gate voltages, which are used to tune E_F in an experiment. This linear dispersion relation implies that electrons in graphene will behave like massless Dirac fermions. They have a dispersion that looks relativistic and will travel at a fixed speed $dE/dk = v_F \approx 1 \times 10^6$ m/s.

As a material for exploring electron hydrodynamics, the key aspects of graphene are its high conductivity (long l_{mr}) and strong electron-electron interactions (short l_{ee}) near the CNP. The first aspect results partly from the ease of producing many-micron scale graphene sheets with a low number of impurities or defects, starting from high-purity graphite and using tape to peel off layers until a sheet only a single atom thick

remains. Scattering from charged impurities outside the graphene itself is minimized by sandwiching the graphene between layers of hexagonal boron-nitride (hBN) [140]. The long l_{mr} in graphene are also the result of low electron-phonon scattering rates, due to the small Fermi-surface of graphene, which restricts the phase space of electron-phonon scattering, and the high stiffness of the C bonds, which gives a high Debye temperature [141, 142]. The second important aspect, low l_{ee} near the CNP, results from the relatively fast electron-electron scattering rates at low carrier densities, as the Coulomb interactions are not screened as heavily as in normal metallic systems. In the case of monolayer graphene, which we will examine here, it seems possible to separate l_{ee} and l_{mr} by a factor of about 20, in the temperature range 100–150 K. To observe hydrodynamic effects, the device geometry length scale l_{geom} should be placed somewhere between l_{ee} (a few hundred nm) and l_{mr} (several microns).

5.2   Transport signatures of electron hydrodynamics

Some consequences of electron hydrodynamics were predicted by Gurzhi in the 1960s [143], and a few initial transport signatures were detected in the 1990s in two-dimensional electron gases (2DEGs) [132, 133]. Starting around 2016, there has been a revival in interest in this topic, brought on by several experimental and theoretical papers describing transport signatures of electron hydrodynamics [134, 136, 144, 145]. These have been followed by an onslaught of new theory and transport papers over the last couple years. The transport signatures can be divided into two broad categories, the first looking at charge signatures of hydrodynamics, and the second looking at thermal transport signatures. The thermal transport measurements have involved looking for the breakdown of the Wiedemann-Franz (WF) law. This law gives a fixed ratio, known as the Lorenz number, of the product of electrical resistivity ρ and thermal conductivity κ to the temperature

T of $L_0 = \rho\kappa/T = 2.44 \times 10^{-8}$ WΩ/K^2. This relation holds (approximately) over a wide temperature for most metallic systems, where the same charged quasiparticles that carry electrical currents also contribute significantly to thermal conduction. Near the CNP of graphene (in the so-called Dirac fluid), charge currents are carried by thermally excited electrons and holes flowing in opposite directions and these charge currents are relaxed through electron-hole recombination. Thermal currents, on the other hand, are carried by electrons and holes flowing in the same direction and this difference in the behavior of charge versus thermal currents can lead to a large increase in the Lorenz number near the CNP point of graphene [144]. The WF law can also be violated in the Fermi liquid regime due to momentum conserving electron-electron interactions, as these interactions will generally decrease the thermal conductivity while leaving the charge conductivity unaffected, leading to a decreased Lorenz number [146, 147].

The charge transport measurements of electron hydrodynamics have looked for modifications to electrical resistances with a particular temperature or geometric dependence, such as negative potentials caused by vortices [136, 148], or flow through a narrow constriction or channel [134, 135, 147, 149]. Figure 5.2 describes a few of these different geometries.

The charge signatures of electron hydrodynamics are expected to be visible in the Fermi liquid regime (Fermi energy $\epsilon_F >> k_B T$). In this regime, a first-order, steady-state, hydrodynamic description of the graphene electron system gives

$$\frac{\partial_i \delta_\mu}{\mu} - \nu \partial_j^2 v_i = -\frac{v_i}{\tau_{mr}} \tag{5.2}$$

for chemical potential expanded to first order $\mu + \delta_\mu$, ν is the kinematic viscosity, v_i is the "flow" or drift velocity in direction i, and τ_{mr} is the momentum-relaxing scattering time [150]. If the further assumption of incompressible flow is made, a 2D stream function
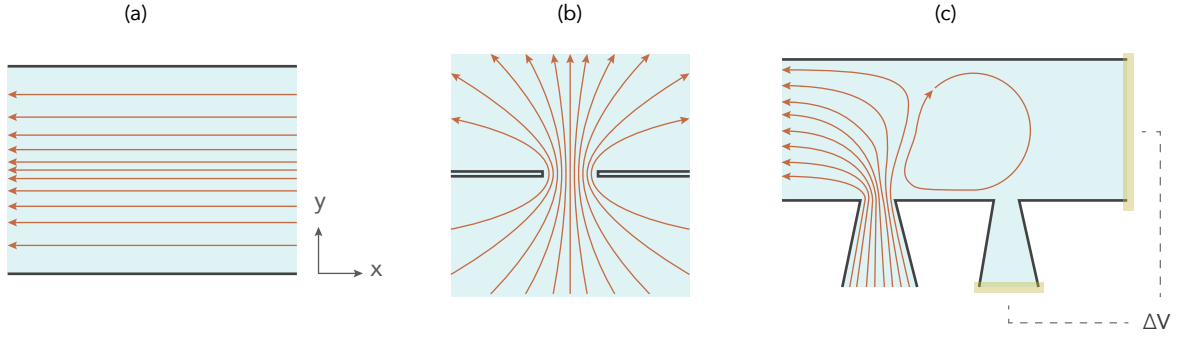
Figure 5.2: Three device geometries for studying electron hydrodynamics. (a) Channel geometry. (b) Constriction geometry. (c) "Vicinity" geometry. A non-local negative resistance measured across the two leads on the right may be indicative of eddy-like flow.

ψ can be defined using $v_x = \partial_y \psi$ and $v_y = -\partial_x \psi$. Plugging the stream function into equation 5.2, and taking the curl gives,

$$(\partial_x^2 + \partial_y^2)\left((\partial_x^2 + \partial_y^2)\psi - \frac{\psi}{\lambda^2}\right) = 0 \tag{5.3}$$

where $\lambda = \sqrt{\nu \tau_{mr}}$. The solutions can be broken into two parts $\psi = \psi_0 + \psi_\lambda$, such that $(\partial_x^2 + \partial_y^2)\psi_0 = 0$ and $\left((\partial_x^2 + \partial_y^2)\psi_\lambda - \frac{\psi_\lambda}{\lambda^2}\right) = 0$ [150]. The second equation includes a characteristic length scale λ, called the Gurzhi length, which determines the scale of flow pattern changes away from boundaries. This length scale can also be written terms of the momentum-relaxing length l_{mr} and momentum conserving length l_{ee}, $\lambda = \sqrt{l_{ee}l_{mr}/4}$ The full solution depends on the specific choice of boundary conditions. The two limiting cases are the no-slip boundary condition, given by a drift velocity $v_j = 0$ for $\hat{\boldsymbol{j}}$ pointing along the boundary edge, and the no-stress boundary condition, $\partial_i v_j = 0$ for $\hat{\boldsymbol{i}}$ pointing inward from the boundary, perpendicular to the edge.

In a channel of width w, running along the x-axis (Fig. 5.2(a)), assuming no-slip

103

boundary conditions, this gives an electron flow profile

$$v_x \propto \left(1 - \frac{\cosh\left(\frac{y}{\lambda}\right)}{\cosh\left(\frac{w}{2\lambda}\right)} \right) \tag{5.4}$$

In the limit that the Gurzhi length is long (for short l_{ee} and long l_{mr}) compared to the channel width, this flow profile approaches parabolic Poiseuille-type flow. In this case, the channel resistance is expected to scale like $R \propto w^{-3}$, compared to the w^{-1} scaling for ohmic flow [150]. In the no-stress case, the current density is constant across the channel, and the channel resistances will scale with channel width in the same way as for ohmic flow. The boundary conditions obviously play an important role in determining the current flow, but these boundary conditions are usually not well defined as they depend on the details of the device fabrication in a nontrivial way. In plasma-etch-defined graphene devices at the temperatures relevant for observing hydrodynamic effects, estimates of these slip lengths are on order of the geometry length scales [136, 151, 152].

Looking for electron hydrodynamics in a constriction may avoid some of the pitfalls of unknown boundary conditions as the flow in this geometry is determined partly by the converging and diverging of the current density. In the constriction flow, the conductance can be broken into ballistic and viscous contributions $G = G_b + G_c$, where the viscous contribution G_c is expected to scale with constriction width w like $G_c \propto w^2$ and with temperature T like $G_c \propto T^2$ in the hydrodynamic regime [135, 150]. This geometry is also nice because it might allow for three different flow regimes to be distinguished: ohmic, hydrodynamic, and ballistic [149]. The constriction geometry will be our focus in this chapter.

Although transport measurements have yielded geometric and temperature scalings consistent the expected behavior of the various transport regimes, a measurement of the local current density in the constriction geometry will be provide a more direct method of

probing these regimes. The way we will do this is obviously scanning NV magnetometry, but other techniques like scanning single electron transistors can also be used [152] and these techniques complement each other in many ways. Ideally, we would have a device that can reproduce the transport signatures seen previously, and also be used to locally probe the current density for hydrodynamics effects.

5.2.1   Narrow constriction transport

Figure 5.3(a) shows a device geometry similar to that in Ref. [135], consisting of a series of constrictions with varying widths, ∼400 nm–1µm. This device has a graphite backgate for tuning the carrier density, and is sandwiched between a 48 nm bottom hBN layer and a 23 nm top hBN layer. Sandwiching graphene between hBN and using a graphite gate (vs. a doped Si/SiO_x gate) yields graphene samples with extremely low disorder [153]. The device resistance as a function of carrier density and temperature is measured for each constriction by sweeping the back-gate and measuring the voltage drop across the constriction (Fig. 5.3).

The temperature dependence of the constriction resistances is then analyzed for consistency with a hydrodynamic model of electron flow. As mentioned above, the resistance of small (sub-µm) constrictions is expected to decrease with increasing temperature due to hydrodynamic effects, dipping below the lowest temperature, ballistic resistance. In the ballistic regime, the constriction resistance is geometric— electrons with wavevectors not pointing through the constriction are scattered off the device walls, but in the regime of short l_ee, momentum conserving scattering can effectively shield some of these electrons from seeing the device boundary, guiding them through the constriction. Figure 5.4 shows this effect, observed first in [135] and reproduced in our device. The derivative of resistance with temperature dR/dT is mapped as a function of carrier density (n) and
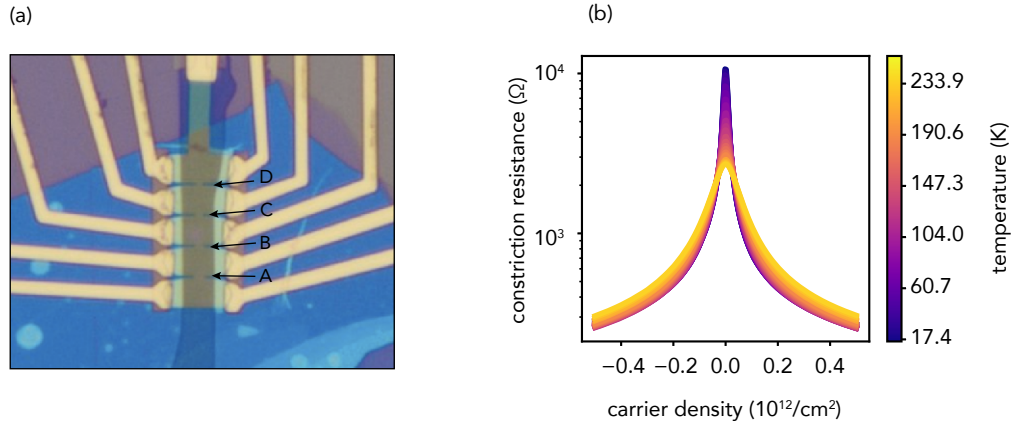
Figure 5.3: (a) Photograph of a series of constrictions etched in monolayer graphene. The widths of the constriction can be measured at low temperature by their Sharvin resistance. This gives widths of 960, 670, 580, and 390 nm for the constrictions A, B, C, and D respectively. (b) Gate sweeps of the carrier density for constriction C as a function of temperature.

temperature (T) for each constriction, showing that each constriction has some areas of temperature/carrier density space with negative dR/dT at low temperature. However, the temperature dependence is not quite as pronounced as in [135]. Figure 5.5 shows cuts through the constriction resistances along the temperature axis. The resistance minimums for these carrier densities occur over the range 100-130 K, except in the case of constriction B, whose resistance is mostly flat until it starts to increase at 75-100 K. The width dependence of the viscous conductance G_c is also shown (upper right of Fig. 5.5), but there are not really enough points to say whether the width dependence of G_c is proportional to w^2, especially since constriction B is throwing off the trend, with $dR/dT \sim 0$ at low temperature.

So while we have reproduced some of the transport signatures seen in [135], the hydrodynamic signature of negative dR/dT is not as pronounced and is not visible in all our constrictions. In terms of probing the local current density, there's a larger problem with this device, which is that while these relatively narrow constrictions $w < 1$ µm
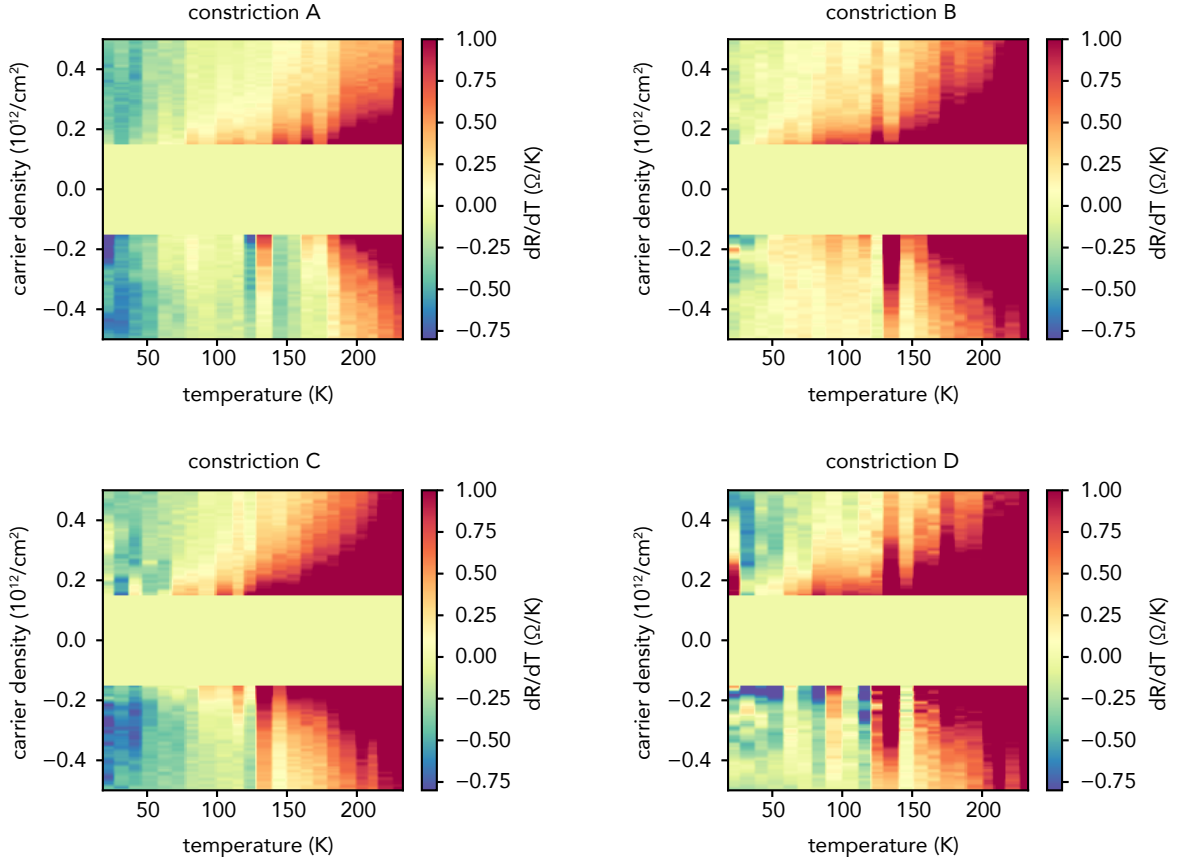
Figure 5.4: Interpolated maps of dR/dT for each constriction. The negative dR/DT slope at lower temperatures has been attributed to hydrodynamics effects [135]. The data near the CNP has been removed because it describes the Dirac fluid where the charge transport signatures of hydrodynamics are expected to disappear, and the large resistances near CN mask this dR/dT Fermi liquid behavior when plotted on the same scale.

can still show hydrodynamic effects in transport measurements, they are not ideal for locally studying the current flow within the constrictions. This difference in desired device geometry for transport versus local probe measurements arises because the local measurement is most sensitive to changes in the current pattern right at the constriction, where the current density is large, while the transport measurements are most sensitive to the larger-scale structure of the current pattern. The current profile across small constrictions with width $w < l_{ee}$ will look ballistic, but far from the constriction ($> l_{ee}$),
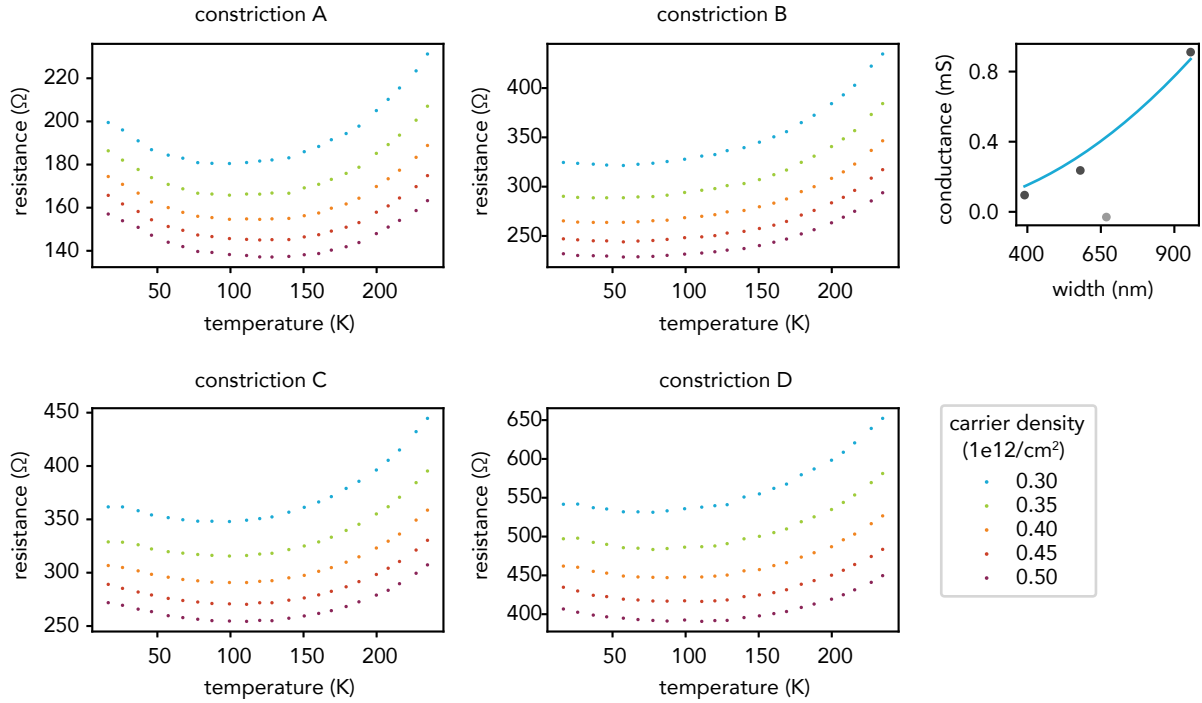
Figure 5.5: Linecuts through the resistance vs. temperature data for each constriction shown in Fig. 5.3, plotted for several carrier densities. A, C, and D show a clear negative dR/dT, while B is mostly flat at low temperature. The upper right plot shows the viscous conductance of each constriction and a fit to w^2, not including B. More width points are need to reproduce the w^2 dependence seen in [135].

the current pattern will be altered by electron-electron scattering. For example, with $w < l_{ee}$, the directivity $\mathbf{j} \cdot \hat{\mathbf{r}}$ defined around a semicircle far from the constriction, with $\hat{\mathbf{r}}$ normal to the circle, is expected to have a $sin(\theta)$ dependence in the ballistic regime and a $sin^2(\theta)$ dependence in the hydrodynamic regime [154, 155]. This motivates moving to larger constriction widths for the scanning measurements. As an added benefit of moving to a wider constriction, the ohmic regime is most visible when the constriction width is much larger than the constriction length, a condition that is more easily satisfied for wider constrictions due to limits of fabrication resolution.

5.3   Probing local current density

NV magnetometry can be used to detect the stray magnetic fields produced by flowing electric currents. As described in Appendix E, starting from a large map of the magnetic field along the NV axis, B_{NV}, it is sometimes possible to reconstruct all components of the vector magnetic field. In Chapter 4, we saw that even if you can measure the vector field above a magnetic sample, there is no way to map that field to a single magnetic pattern. For a 2D current pattern, this ambiguity doesn't exist— if you know the magnetic field in an infinite plane above the 2D current plane, you can calculate the current density everywhere (up to a constant offset). In practice the reconstruction is not perfect, as measurement noise in conjunction with the finite NV-sample separation will limit the resolution of the reconstruction, and the finite imaging area will distort the reconstructed current pattern at the image edges. The difference in the ability to map magnetic fields to 2D current versus 2D magnetic patterns is due to the presence of in-plane magnetization components. If a 2D magnetic pattern has only an out-of-plane component M_z, then the magnetic reconstruction problem is similar to the current reconstruction problem. This is apparent from the ability to map a little volume of magnetization M_z into a little current loop.

For the case of a 2D or thin-film current density, the field components B_x and B_y can be used to reconstruct the underlying current density components j_x and j_y. This procedure, outlined below, is described in detail in [156] for a SQUID magnetometer and in [157] for a single NV. Starting from the Biot-Savart law, with the current distribution confined to the $z = 0$ plane,

$$B_x(x, y, z) = \frac{\mu_0}{4\pi} z \int_{-\infty}^{\infty} dy' \int_{-\infty}^{\infty} dx' \frac{j_y(x', y')}{((x - x')^2 + (y - y')^2 + z^2)^{3/2}} \tag{5.5}$$

$$B_y(x, y, z) = \frac{\mu_0}{4\pi} z \int_{-\infty}^{\infty} dy' \int_{-\infty}^{\infty} dx' \frac{-j_x(x', y')}{((x - x')^2 + (y - y')^2 + z^2)^{3/2}} \qquad (5.6)$$

Taking the Fourier transform, and using the convolution theorem,

$$\mathcal{F}[B_x](k_x, k_y, z) = \mathcal{F}[G \star j_y] = g(k_x, k_y, z)\mathcal{F}[j_y](k_x, k_y, z) \qquad (5.7)$$

$$\mathcal{F}[B_y](k_x, k_y, z) = -\mathcal{F}[G \star j_x] = -g(k_x, k_y, z)\mathcal{F}[j_x](k_x, k_y, z) \qquad (5.8)$$

where $g(k_x, k_y, z) = \mathcal{F}[G(x - x', y - y', z)] = (\mu_0/2)e^{-kz}$ is the Fourier transform of the Laplacian Green's function. These equations can be inverted to solve for the current densities in terms of the stray field,

$$\mathcal{F}[j_y] = \frac{\mathcal{F}[B_x]}{g} \qquad (5.9)$$

$$\mathcal{F}[j_x] = \frac{-\mathcal{F}[B_y]}{g} \qquad (5.10)$$

This shows that the field components B_x and B_y, reconstructed from B_{NV} as above, can then be used to reconstruct the current distribution confined to a 2D plane. The caveat given above, that constant values B_x and B_y are lost in the reconstruction, here implies that any uniform component of the current density will be lost in the reconstruction. This means that each component of the reconstructed current density will be shifted by a constant value, if the mean of that component is not zero. We can remove this offset by shifting the reconstructed components by their values in an area of the image where we know the current density is zero (e.g. in the etched areas next to the slit).

Carrying out this reconstruction from measured field data comes with a few potential issues, along with the finite image artifacts mentioned above. First, the factor $1/g =$

$(2/\mu_0)e^{kz}$ becomes large for $z > (1/k)$. If the field is sampled with a resolution $\Delta x < z$, and the SNR is not too impressive, then the reconstructed current density will be dominated by noise at the frequency $1/\Delta x$, which is amplified by $1/g$. On the other hand, if $\Delta x \gg z$, then sharp changes in the stray field may end up getting aliased. However, aliasing is more likely to occur in magnetic samples with sharp changes in magnetization than in the present case where the stray field is given by a convolution over an extended current distribution. An example of this reconstruction procedure is given for simulated data in Appendix E.

As opposed to magnetic samples, where the stray magnetic fields can be detrimentally large for NV sensing, the stray fields produced by µA-scale currents flowing in µm-scale devices can push the limits of single-NV sensitivity ($\sim \mathrm{nT}/\sqrt{\mathrm{Hz}}$). For graphene samples, one way to quantify the NV sensitivity to currents, is to examine the limit of a current sheet, where the NV-graphene separation is much smaller than features in the current density. For a sheet of current with current density $\mathbf{J} = J\hat{\mathbf{y}}$, the in-plane stray field is $B_x = (1/2)\mu_0 J$ above the sample. And a DC magnetic field sensitivity of $2\,\mathrm{\mu T}/\sqrt{\mathrm{Hz}}$ gives a DC current sheet sensitivity of $\sim 3\,\mathrm{A/m}/\sqrt{\mathrm{Hz}}$. Detecting µA/m-scale current density variations in the current profile µm scale constrictions requires measuring for seconds.

5.4   Imaging the ohmic to non-ohmic transition

A local probe of the current density near a constriction can, in principle, be used to distinguish three different regimes of current flow— ohmic, hydrodynamic, and ballistic, assuming the constriction width is chosen correctly. If a fixed carrier density is also chosen judiciously, then the current density patterns should transition from ohmic at room temperature, through hydrodynamic as the temperature is decreased, and finally to ballistic at low temperature (Fig. 5.6).

As discussed above, it may not be possible to be deep in the hydrodynamic regime ($l_{ee} \ll l_{geom} \ll l_{mr}$) in monolayer graphene. This means that disentangling the effects of electron-electron interactions on the flow profiles through a constriction can be a subtle business. In order to understand the kind of current profiles expected in these different regimes and choose an ideal geometry for observing hydrodynamic effects, a Boltzmann transport simulation can be used to calculate the current flow patterns for arbitrary l_{mr} and l_{ee} lengths. Using simulations[1] based on [149], some examples of current flow profiles across a $w = 2.7$ µm channel are plotted in Fig. 5.6. At high temperature, l_{mr} and l_{ee} are both expected to be short compared to this w and the flow profile should have the ohmic "ears" at the constriction edges, seen in the left profile. This shape arises as a solution to Laplace's equation for the electric potential, as governed by Ohm's law.

The temperature dependence of electron-phonon scattering rates in graphene is set by the Bloch-Gruneisen temperature $\Theta_{BG} = 2\hbar v_s k_F / k_B$ where v_s is the phonon sound velocity and k_F is the Fermi wavevector. These scattering rates scale as $\Gamma_{ep} \propto T^4$ (T) for temperatures T below (above) Θ_{BG} respectively [141]. For the low carrier densities ($<$1e12/cm^2) the temperatures of our scanning measurements ($>$75 K) are above Θ_{BG}, where the phonon contribution to τ_{mr} is expected to scale linearly with T. The electron-electron scattering rate, on the other hand, is expected to scale with temperature like

$$\Gamma_{ee} \approx \frac{E_F}{2\pi\hbar}\left(\frac{k_B T}{E_F}\right)^2 ln\left(\frac{2E_F}{k_B T}\right) \tag{5.11}$$

in the Fermi liquid regime [135, 158]. At intermediate temperatures, around $T = 100 - 150K$, l_{mr} and l_{ee} will both increase from their room temperature values, but l_{mr} is expected to increase more quickly, while changes in l_{ee} are expected to be smaller [135]. This can lead to the condition $l_{ee} < w < l_{ep}$, and a rounded current density profile (center

---

[1]Boltzmann simulations written by Andrew Lucas

of Fig. 5.6). Indeed, in the hydrodynamic regime with no slip boundary conditions the current profile inside the constriction is expected to be semi-circular [149]

$$j_y \propto \sqrt{\frac{w^2}{4} - x^2} \tag{5.12}$$

As the temperature is lowered further, the flow is expected to become ballistic as l_{ee} and l_{mr} become larger than the constriction width, with a profile that is flat across the constriction. Even before this point, if $l_{ee} > 0.5w$, the profile becomes pretty flat (right side of Fig. 5.6).
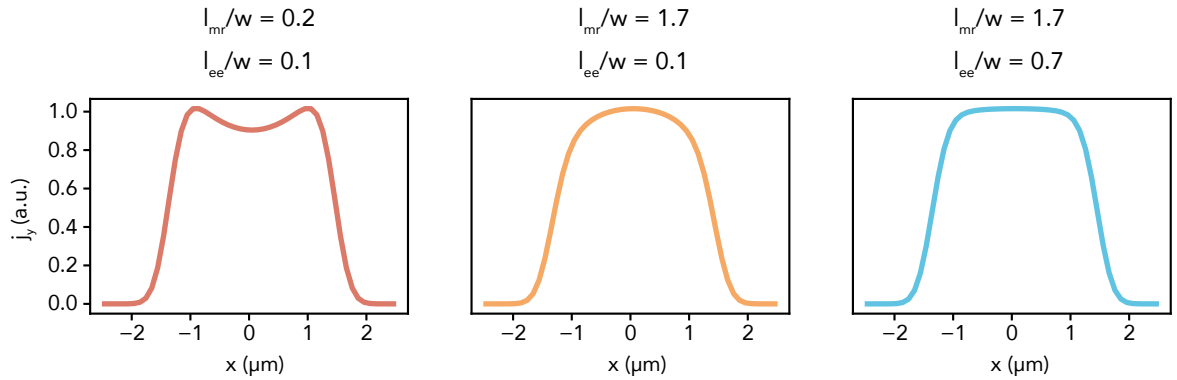
Figure 5.6: Simulations of the current flow profile in a linecut across the constriction. The constriction width in the simulation is 2.7 µm. The l_{mr} and l_{ee} label each plot. These values roughly approximate those that could be expected at room temperature (left), intermediate temperatures 100-150 K (center), and low temperature <50 K (right). The simulations are gaussian filtered at the NV height z_{NV}, because the NV measurement reconstruction would be expected to yield profiles similarly filtered.

The constriction geometry used for scanning measurements is shown in Fig. 5.7(c). The constriction width is $w = 2.72$ µm and the length is $l = 375$ nm, as measured by SEM on a similar device (Fig. 5.7(a,b)). The actual width of the constriction may differ slightly from the SEM-measured width due to damage or doping at the device edges. Fig. 5.7(c) shows a photograph of the device used for the following scanning measurements.
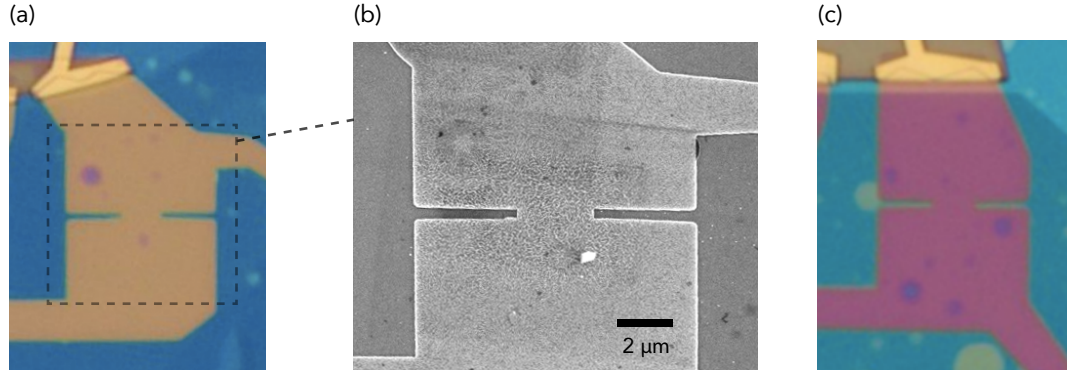
Figure 5.7: Constriction geometry for scanning measurements. (a) Optical image. (b) SEM image. The SEM image is used to measure the constriction geometry, giving width $w = 2.72$ µm and length $l = 375$ nm. (c) Optical image of the device used for the following measurements.

5.4.1   Current density reconstruction near the CNP at room temperature

Starting at room temperature, ohmic flow is probed by tuning the back-gate near the CNP. The frequency of one of the NV spin transitions is measured using the frequency modulation sweep described in section 2.2.2. The measurement at each pixel is performed for alternating current direction $\pm I$, and the field is calculated from the difference of the measured frequencies $(f_{+I} - f_{-I})/2$. This differential measurement removes shifts in the NV resonance due to sources other than the current flow, like static electric fields near the graphene/gate edges (see Appendix F) or long-term drifts of the external magnetic field. As described in Sec. 5.3, measurement of the field far from the constriction is required because the discontinuities present when wrapping the image boundaries will distort the reconstructed current density. The measurement points are spread sparsely in the areas far from the slit and are spaced more finely near the slit, where the good stuff is happening, in order to save time. Still, a single scan is typically several hours, taking several seconds at each pixel to measure the field with sub-µT error. Figure 5.8(a) shows

the measurement of NV frequency over the sparse and fine regions and Fig. 5.8(b) shows the frequency map with the sparse areas linearly interpolated.

The NV transition frequency is converted to a magnetic field along the NV axis and the data is averaged over the approximate point spread function of the measurement, given by the NV height z_{NV}. This averaged data is then used to reconstruct the field components (B_x, B_y, B_z), using the procedure described in Appendix . The result is shown in Fig. 5.8(c-f). The reconstructed B_x and B_y are then used to calculate the current density, using Eqn. 5.9 and 5.10. Figure 5.9 shows the reconstructed current density components j_x and j_y, as well as the magnitude $|j|$, and a linecut of j_y across the slit. The peaks in current density at the slit edges are consistent with the expected current density profile from ohmic flow $(l_{mr} < w)$.
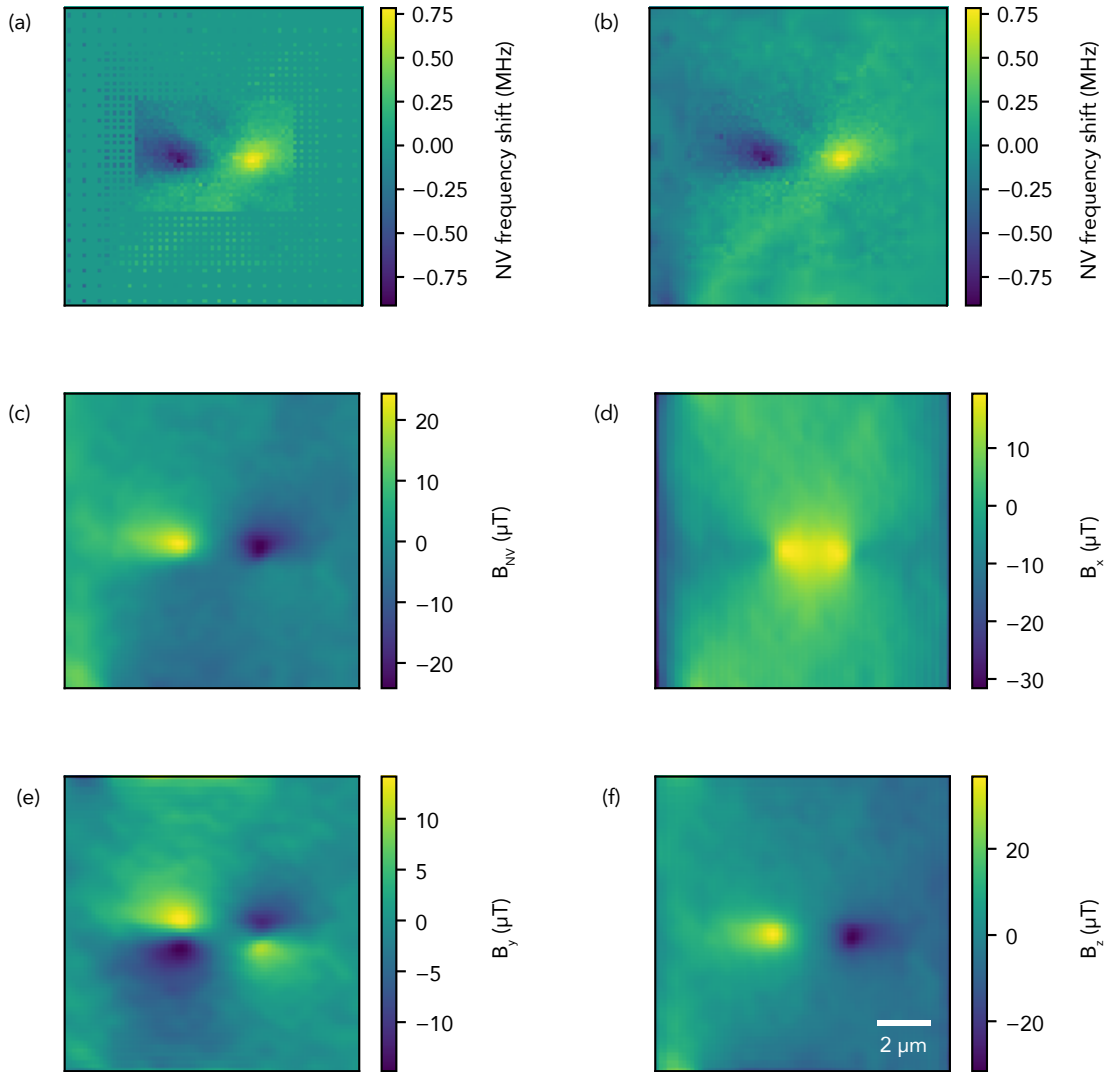
Figure 5.8: Measurement of NV spin transition frequency in an imaging area over the slit. (a) The data measured in grids with different spacing depending on distance from the slit. A measurement like this typically takes 6-12 hours. (b) The NV measurement with linear interpolation between the sparsely sampled points. (c) The magnetic field along the NV axis. (d-f) The reconstructed components of the magnetic field.
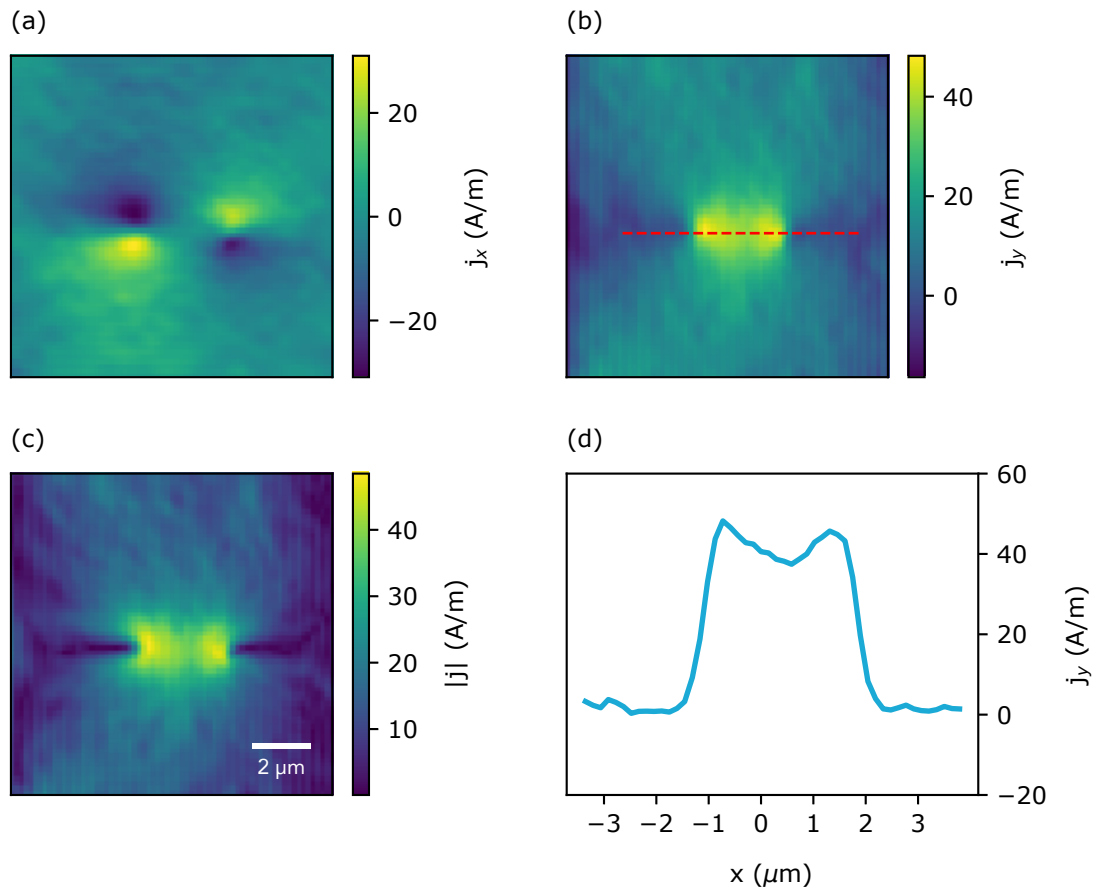
Figure 5.9: Reconstructed current density. (a) j_x, (b) j_y, (c) $|j| = \sqrt{j_x^2 + j_y^2}$, (d) linecut across reconstructed j_y at the position indicated by red dashed line in (b).

5.4.2   Temperature dependence of the current profile

The measurement of current density in the constriction was repeated at different sample temperatures. Figure 5.10 shows the j_y current density component in a linecut across the constriction at several temperatures for a fixed carrier density $n = 7 \times 10^{11}/\mathrm{cm}^2$. At room temperature, 298 K, the current profile has large ohmic ears indicating that $l_{mr} < w$. As the temperature is lowered, these ears disappear, but a strong semi-circular shape doesn't emerge. Instead the current profile flattens out on top.
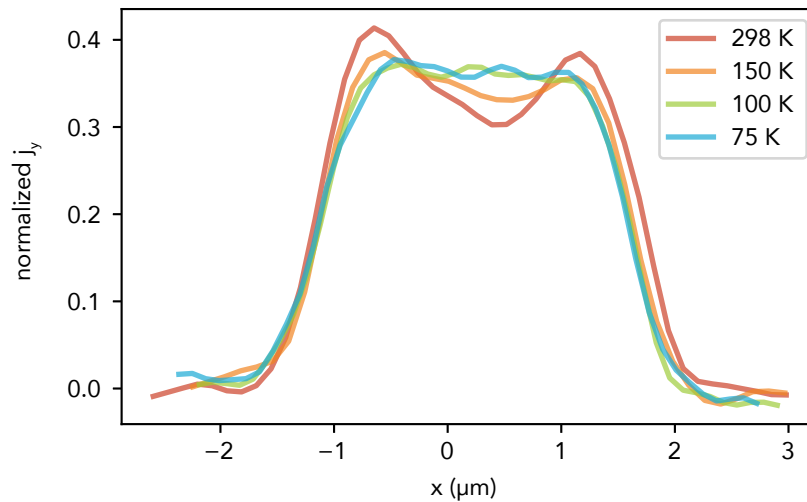

Figure 5.10: Reconstructed j_y linecuts across the constriction over a wide temperature range for a fixed carrier density $n = 7 \times 10^{11}/\mathrm{cm}^2$. The current density is normalized by the integrated current density over the constriction.

Using simulations of current flow through the constriction, it is possible to make error maps, comparing the simulated data for various l_{mr} and l_{ee} to the measured profiles. It is preferable to use data near the constriction for this comparison (Sec. 5.4.5). Figure 5.11 shows these error maps for $n = 7 \times 10^{11}/\mathrm{cm}^2$ at four different temperatures. The extracted value of l_{mr} increases with decreasing temperature, as expected, but l_{ee} is not well constrained at higher temperatures. The values of l_{mr} are also lower than expected [159]. At lower temperatures, l_{ee} is better constrained by the error maps, but

the extracted values ($<$ 200 nm) are shorter than expected [135]. Likely the bubbles discussed in section 5.4.5 are playing a role in determining the current profiles inside the constriction and ultimately changing the landscape of these error maps.
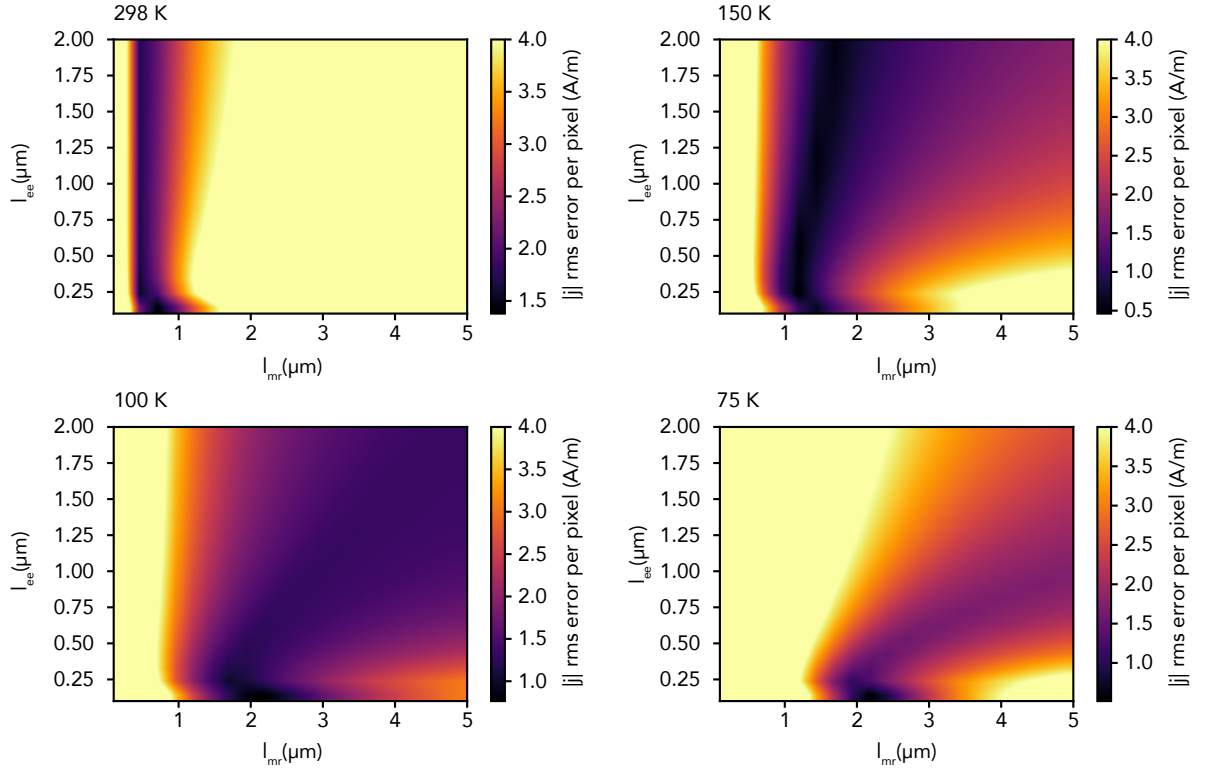

Figure 5.11: Error maps of l_{ee}–l_{mr} space comparing simulations to the measured current densities in three scan lines centered on the constriction. Each plot is labeled by temperature. The error is plotted in terms of the RMS current density error per pixel.

5.4.3   Carrier density dependence of the current profile

At a fixed temperature, it is also possible to change the current flow regime by tuning the carrier density. Figure 5.12 shows the current profiles at 100 K as the carrier density is tuned close to and away from the CNP. The flow becomes more ohmic near the CNP, resembling the room temperature flow profiles. Since we are applying a not-insignificant voltage bias to drive 150 µA through the constriction and contacts, the voltage at the

constriction due to the source bias will lead to in-equivalent potential differences between the constriction and the gate for positive vs. negative currents. This means that the CNP voltage will effectively move as we change from positive to negative currents. We are therefore measuring an averaged current flow pattern for carrier densities near the CNP. At 100 K the resistance peak of the CNP, seen in transport measurements, is sharper than at room temperature, making this effect more significant than for the image in Fig. 5.9.
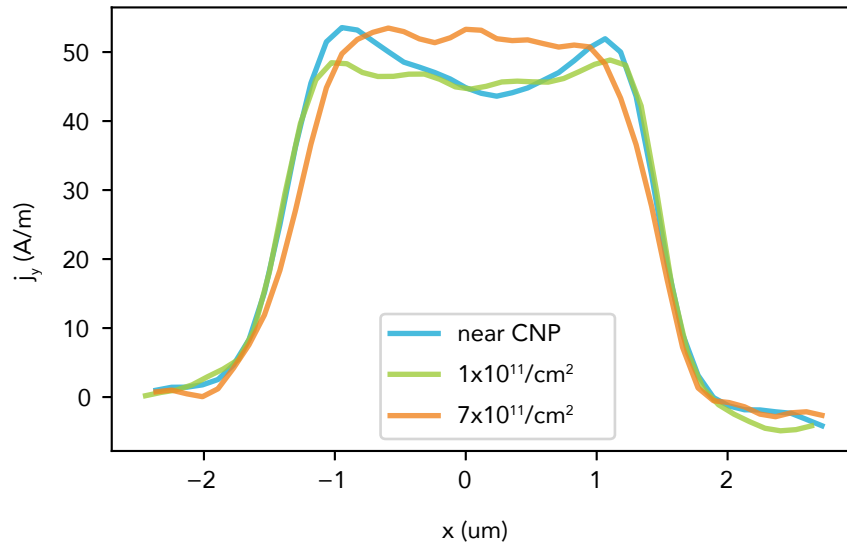

Figure 5.12: Reconstructed j_y linecuts across the constriction at 100 K for different carrier densities.

5.4.4   Transport measurements of l_{mr}

Measurements of the sample resistivity can be used to estimate l_{mr}, allowing for a comparison with values of l_{mr} extracted from the reconstructed current profile. In the diffusive regime ($l_{mr} < l_{geom}$) the momentum relaxing mean free path is given by,

$$l_{mr} = \frac{h}{2e^2 \rho \sqrt{\pi n}}$$

(5.13)

in terms of resistivity ρ and carrier density n. In another area of the graphene device shown in Fig. 5.7, the resistivity was measured and the mean free path calculated as a function of carrier density and temperature (Fig. 5.13). Note that the diffusive condition is not expected to be met in this device at lower temperatures, where l_{mr} is expected to be many µm. The breakdown of Eqn. 5.13 at low temperatures may explain the small measured values of l_{mr} and the saturation at 75–100 K, as ballistic effects are likely important in this geometry at those temperatures. It is also possible that a bubble in the probed transport area, seen below the V- lead in Fig. 5.13(b), is increasing the device resistance and lowering the extracted values of l_{mr}. See the next section for a discussion of bubbles.   Transport measurements are also useful for probing the linearity of the
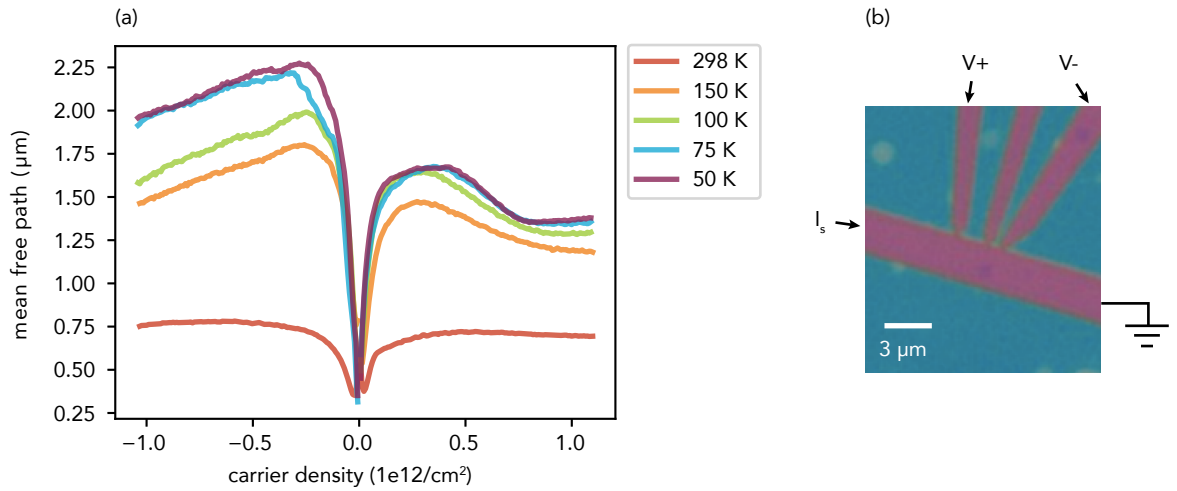

Figure 5.13: (a) Transport measurements of mean free path (l_{mr}) as a function of carrier density and gate voltage. The resistivity was measured with a 1 µA excitation at 79 Hz. (b) Device area showing the lead configuration of the transport measurements.

system under the excitation of the large currents used in scanning measurements. Figure 5.14 shows a measurement of device linearity for currents up to the scanning current of 150 µA.
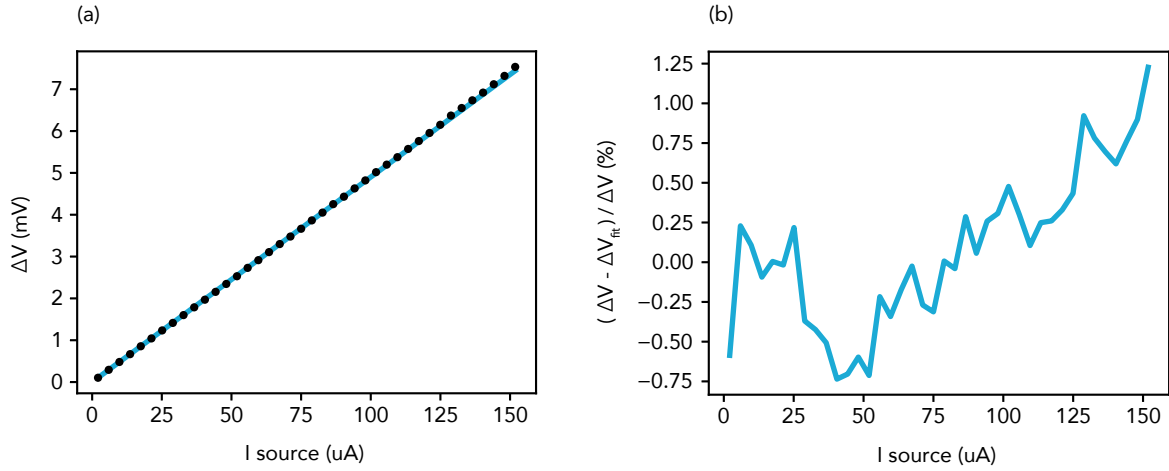
Figure 5.14: (a) Device voltage measured in the configuration shown in Fig. 5.13, as a function of the excitation current. (b) Linearity ratio, showing the (small) deviations of the measured voltage from a linear fit to the low current (<20 µA) data.

5.4.5   Discrepancies in l_{ee} and l_{mr}

Previous transport measurements of l_{mr} have found mean free path of many microns below 150 K [159] and measurements of l_{ee} have found values of several hundred nm below 150 K [135]. The discrepancy between these predicted values of l_{mr} and l_{ee} and the values we extract from current profiles can potentially be explained by bubble defects in the graphene near the constriction. These bubbles can be seen in optical photographs and the areas with bubbles display decreased current densities, especially at negative gate voltages. Figure 5.15 highlights the effect of these bubbles on the current flow. The two holes in the current density magnitude just above the constriction coincide with two bubbles visible in optical images of the device. These holes are visible at any carrier density and temperature, except when tuning the back-gate near the CNP. The asymmetric dependence on gate voltage is likely caused the by the particular sign of doping present in the bubble areas.
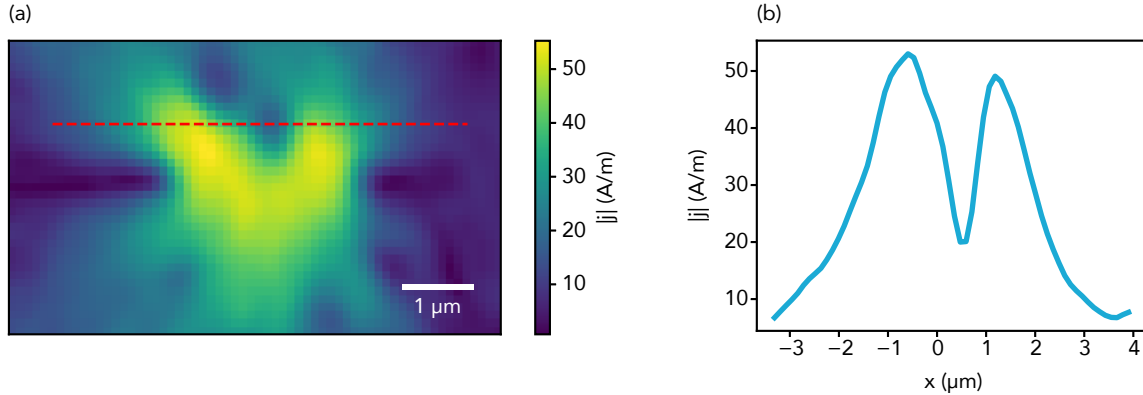
Figure 5.15: (a) Current density reconstruction at 100 K and $n = 1.7 \times 10^{12}/\text{cm}^2$. At large negative gate voltages the effect of bubbles in the graphene devices is pronounced. (b) Linecut through one of the bubble regions, showing decreased current density near the bubble.

5.4.6   Future graphene experiments

In monolayer graphene, this experiment should be repeated without bubbles near the constriction in order to disentangle the current density in the slit from the effects of these high resistivity areas. But there are also many other interesting NV magnetometry experiments that can be performed with similar systems. These include looking for electron whirlpools in a vicinity type geometry [160] or performing experimental jiu jitsu on the bubbles and using them to look for hydrodynamic effects in the surrounding patterns of current flow. In the more distant future, electron hydrodynamics experiments will benefit from a bilayer graphene system, where the electron viscosity is more readily tuned with carrier density ($l_{ee} \propto n^{3/2}$ for AB bilayer graphene with a parabolic-dispersion, compared to $l_{ee} \propto n^{1/2}$ in monolayer graphene) [148]. The techniques demonstrated in this Chapter may also prove useful more generally for distinguishing the effects of electron-electron interactions versus electron-phonon interactions in twisted bilayer graphene systems [161].

Appendix A

Probe fabrication

Figure A.1 shows the general fabrication flow for our diamond probes. Each numbered step is described below:

1. HSQ Transfer

   - clean a double-side polished 280 μm Si piece, solvents and nanostrip
   - clean another Si piece and electrostatically bond diamond with NV side down
   - everything needs to be very clean, tergitol can help remove particles
   - Fox-16 (or 6%) HSQ spin-on: 3 krmp / 30 sec
   - flip diamond + Si transfer onto HSQ
   - press backside of transfer Si with Q-tip on hotplate at 160 C / 2 min
   - remove transfer Si and double-check sample orientation (NVs up)
   - remove HSQ surrounding diamond with IPA and Q-tips

2. HSQ Bond in Suss

   - place clean 70 micron Si piece on top of diamond and a graphite plate on top of this
   - 420 C, 80 mbar, 1.5 hours in Suss wafer bonder
   - During bonding 70 micron Si piece will shatter, and some pieces may be

bonded to any remaining HSQ surrounding the diamond. These pieces should
be chipped off, carefully, as they will complicate the later contact lithography
step used to define the cantilevers.

3. E-Beam Lithorgraphy

   - deposit 5 nm Cr in thermal evaporator #1
   - Fox-16 HSQ spin-on: 3 krmp / 30 sec
   - bake 90 C / 4 min
   - Aquasave spin-on: 4 krpm/30 sec
   - bake 90 C / 15 sec

4. HSQ develop

   - dip in DI water for ~15 sec to remove aquasave
   - ~70 seconds develop time in 25% TMAH

5. Oxygen descum in Technics PEII

   - O_2, 300 mT, 100 W, ~ 30 sec

6. Dry etch Cr sticking layer in ICP #1 or ICP #2

   - Cl_2/O_2 flow rate: 26/4 sccm
   - pressure: 1 Pa
   - ICP/bias powers: 400/15 W
   - ICP #1 etch rate is 22 nm/min

7. Dry etch diamond pillars in ICP #2

   - O_2/Ar flow rate: 40/10 sccm
   - pressure: 0.7 Pa

- ICP/bias powers: 700/70 W (adjust bias/ICP power to change sidewall angle)

- ICP #1 etch rate $\sim$ 100 nm/min

- seems best to etch in 2 min intervals, checking for grass formation and mask erosion frequently in the SEM

8. HSQ/Cr strip

   - remove HSQ and Cr with BHF and Cr wet etchant 1020

9. BCB planarize

   - solvent clean, DI rinse

   - BCB adhesion promoter AP3000, drop-on, wait 30 sec, spin 3 krpm/30 sec

   - BCB 3022-46: spin 500 rpm / 10 sec, then spin 2krpm / 40 sec

   - bake 90 C / 90 sec

   - Blue oven hard cure 250 C / 1 hr w/ N2 flowing

10. AZ5214 cantilever lithography

    - solvent clean

    - bake 110 C / 2 min

    - AZ5214 spin 6krpm / 30 sec

    - bake 95 C / 60 sec

    - 5 sec mask exposure

    - 110 C / 60 sec

    - 60 sec flood exposure

    - develop in AZ 300 MIF / 50 sec

11. Cantilever mask deposit

- deposit Ti(10 nm)/Al(400 nm maybe more depending on diamond thickness) in e-beam #3

- deposit straight-on, using the sample tilt stage at $\sim 22°$

12. Metal mask lift-off

   - strip AZ5214 in NMP @ 80° C for several hours

   - agitate with eyedropper if necessary

13. BCB dry etch in ICP #2

   - O_2/CF_4 flow rates: 30/4 sccm

   - pressure: 0.7 Pa

   - ICP/bias powers: 400/70 W

   - ICP #1 etch rate $\sim$300 nm/min

14. diamond cantilever dry etch in ICP #2

   - O_2/Ar flow rates: 40/10 sccm (CF_4 will help if sputtered BCB is micromasking the etch, but watch out for mask erosion)

   - pressure: 0.7 Pa

   - ICP/bias powers: 700/150 W

   - ICP #1 etch rate ~ 200 nm/min

   - Check mask erosion and grass formation frequently, and stop etching if metal mask is getting thin

15. planarize and protect frontside with thick photoresist layer

   - solvent clean / dehydrate

   - SPR-220-7 spin-on: 400 rpm / 10 sec, 1.5 krpm / 45 sec

- remove wide swaths of PR at the edges (need to make good thermal contact to the Si wafer during the deep etch to prevent bubbling)

- bake 115 C ∼1 hr

16. backside lithography in Suss MA-6

    - make sure there is no HSQ, BCB, other residue on the backside

    - SPR-220-3 spin: 4 krpm / 30 sec

    - bake 115 C 2 min

    - 10.4 sec mask exposure using the backside alignment mode of the MA-6

    - develop in AZ300MIF for ∼ 70 sec

    - wait 30 minutes

    - post-exposure bake @ 115 C for ∼30 min

    - O_2 descum, 10 sec

17. deep Si etch on DSEIII PlasmaTherm

    - use the tool's standard Bosch Si etch with alternating C_4F_8 and SF_6 steps

    - check the etch initially for grass formation and do a short SiOx etch in an ICP or O_2 descum if there's grass formation inside the trenches

    - etch all the way through the Si wafer, exposing the HSQ.

18. dry etch HSQ

    - use standard SiOx etch on ICP #1 or ICP #2

19. dry etch remaining diamond (if any) to release cantilevers, ICP #1 or ICP #2

    - Ar/Cl_2 flow rates: 25/40 sccm

    - pressure: 0.7 Pa

    - ICP/bias powers: 700/250

- ICP #1 etch rate < 50 nm/min for diamond buried in deep trenches

- etch until all cantilevers are released

20. strip plasma hardened PR

  - PR will be hardened due to exposure of fluorine plasma in deep-Si etch

  - O_2 descum, 1 min

  - solvent strip

21. strip BCB and metal cantilever mask

  - HNO_3 at room temperature should remove the BCB

  - heating the HNO_3 in the presence of BCB is not advised as it can result in quite vigorous reactions at high temperature, and, for example blow a covering watch-glass lid off the acid container, spilling hot HNO_3 on the acid bench. Maybe best to close the bench sash during this step.

22. oxygen treat the diamond surface

  - 1:1 HNO_3 : H_2SO_4 at 200° C for 1 hour
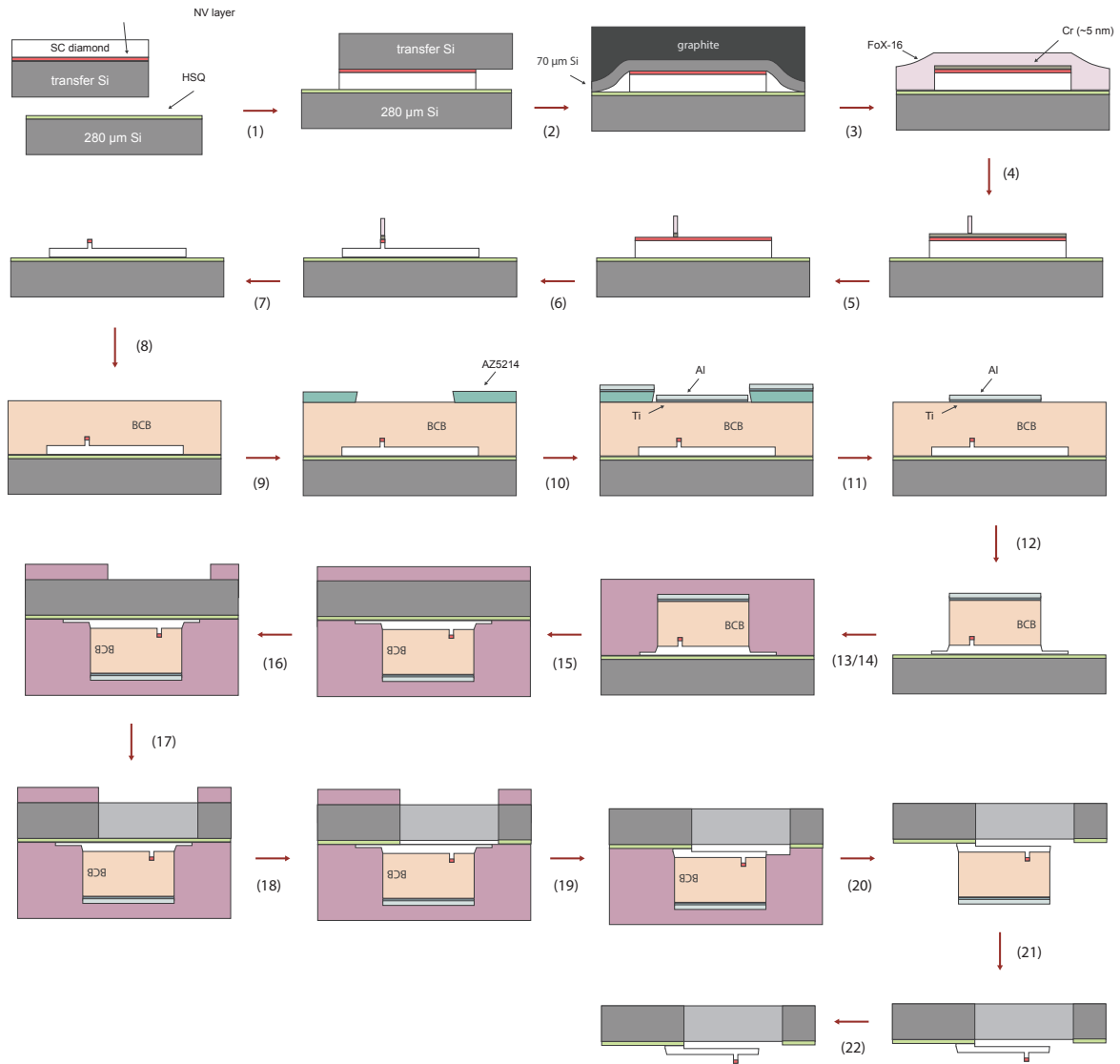
  - O_2 anneal at 450° C for 2 hours

Figure A.1: Overview of the probe fabrication process.

Appendix B

JPE positioning and maintenance

B.1 JPE volume

The positioning volume of a triangular JPE stage is shown in Fig. B.1, in terms of the height of the sample above the JPE stage and radius of the triangular stage. The sample position and tilt as a function of the displacement of the three screws z_1, z_2, and z_3, can be described with a transformation matrix as follows,

$$\begin{pmatrix} x \\ y \\ z \\ R_x \\ R_y \end{pmatrix} = \frac{1}{3R} \begin{pmatrix} -h\sqrt{3} & 0 & h\sqrt{3} \\ h & -2h & h \\ R & R & R \\ -1 & 2 & -1 \\ -\sqrt{3} & 0 & \sqrt{3} \end{pmatrix} \begin{pmatrix} z_1 \\ z_2 \\ z_3 \end{pmatrix} \tag{B.1}$$

where R is the radius of the circle running through all three knobs, h is the height of the sample above the positioning plate, x, y, and z are the Cartesian positions, and R_x and R_y are the respective tilts in the x and y directions. Since the x-y depends on the vertical position of the sample, it is best to arrange the tip and sample separation, when the sample is at the bottom of the vertical range, to be less than 0.6 mm. This usually

131

ensures that the probe will be able to be positioned appropriately to any part of the sample within a lateral displacement of 1–2 mm. Ideally, the tip and sample will be mounted so that the probe is directly above the area of interest of the sample when the inner JPE is center in x and y.
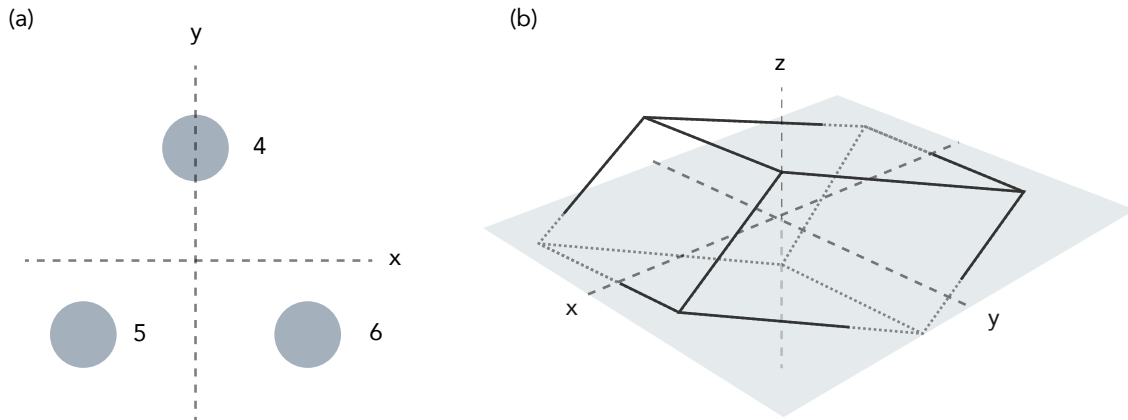

Figure B.1: (a) Outer JPE knobs coordinate system. (b) JPE stage positioning volume. The x-y range is largest if the stage is centered in the z-range.

B.2   JPE knob maintenance

[1] We have seen that the the JPE piezo knobs tend to produce metal debris after a couple years of use. This debris can get stuck in the thread of the spindles making the knobs difficult/slow to turn. This debris can also short the electrical connections to the piezos. To fix these problems, the top PCB board of the knob needs to be removed and the contact pads and spindle cleaned. The cleaning procedure is as follows:

1. **Remove the PCB board on top of the piezo knob**

   In order to do that one has to carefully push the small copper clamp back (this

---

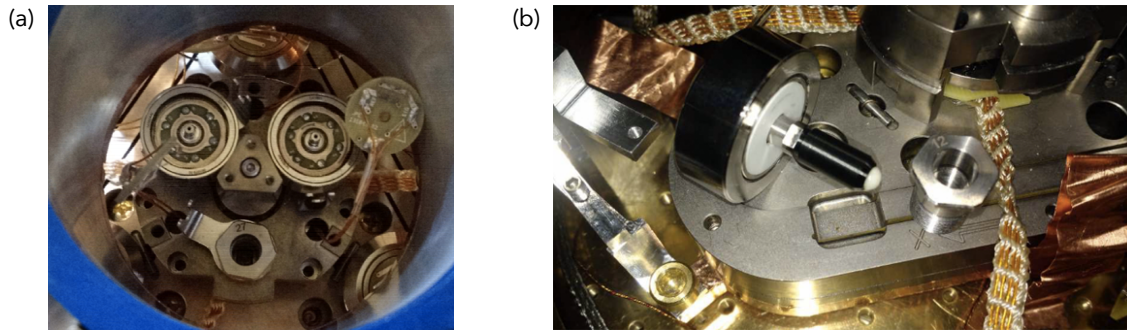[1]Maintenance notes are courtesy of Susanne Baumann

Figure B.2: (a) Inner JPE knobs with PCB boards and one spindle removed. (b) JPE spindle removed from its housing nut.

piece is tiny and might fly off). It works best to two pairs of tweezers, one to push gently down on the PCB board, at the same time also use one end of this tweezers to stop the copper clamp from rotating. With a second pair of tweezers one can then slide the copper piece off. Then remove the metal or ceramic washer holding the PCB board down. Finally, flip the PCB board out of the way. Figure B.2 shows knobs with their PCB boards removed and one knob with the spindle removed.

2. **Clean PCB board and the exposed contacts with a drop of IPA on a Q-tip**

   Metal filings will be build up between the grounded center pin and the other pads

3. **Remove spindle**

   Removing the spindle can either be done by using a very small spanner wrench (we have a customized tool in the drawer), see red arrow in the schematic drawing, or one can simply rotate the spindle out by hand. Be aware that this spindle has very fine threads, so one has to rotate forever to get it out.

4. **Clean the threads**

   Now one can clean the metal debris from threads of the spindle and also from the nut. We have seen most debris in the nut itself. In the image above, the nut was
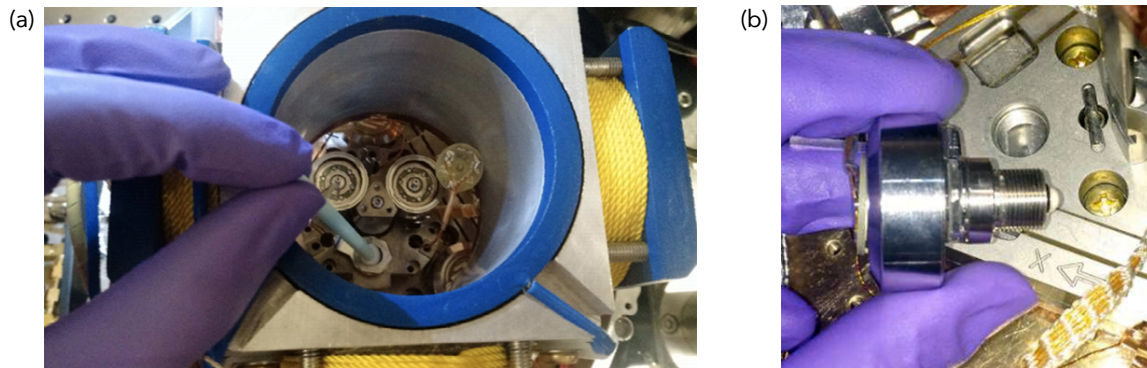
Figure B.3: (a) Cleaning the spindle nut in-place. (b) JPE spindle and nut reassembled.

also removed and is sitting on top of our piezo stage. Alternatively, one can actually leave the nut in place and clean it out from there (see Fig. B.3).

Appendix C
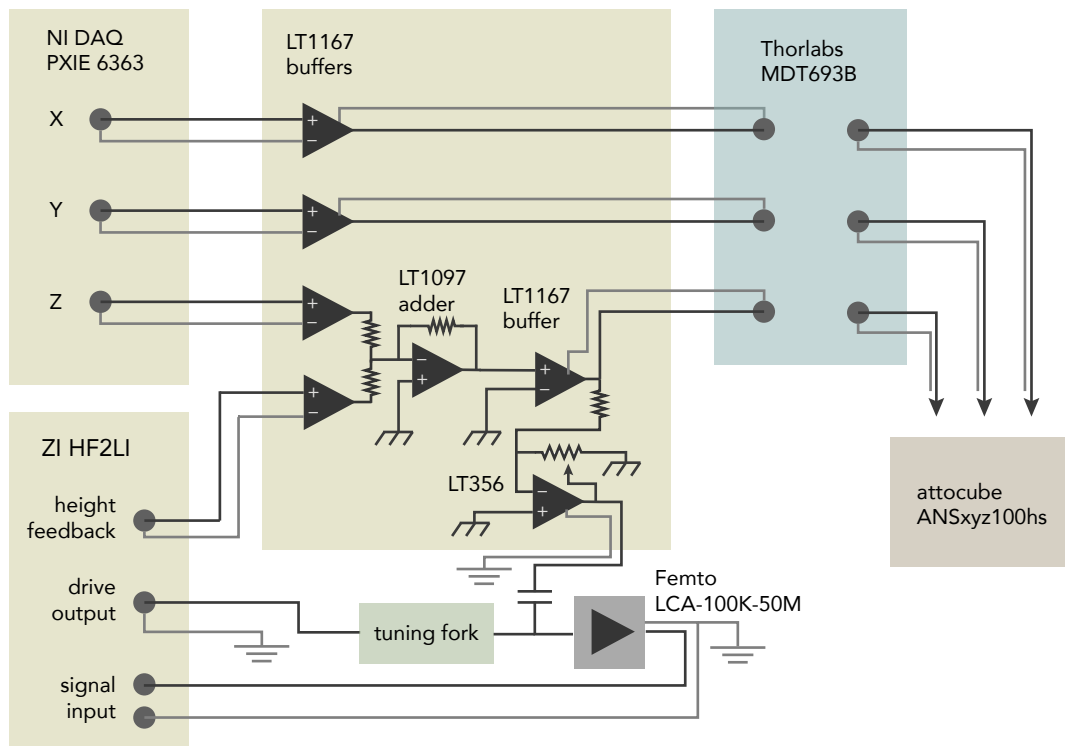
AFM and AOM driver circuits

C.1   AFM circuits

Figure C.1: AFM circuit overview.

Figure C.1 has an overview of AFM's analog circuit boards. The full PCB schematics[1]
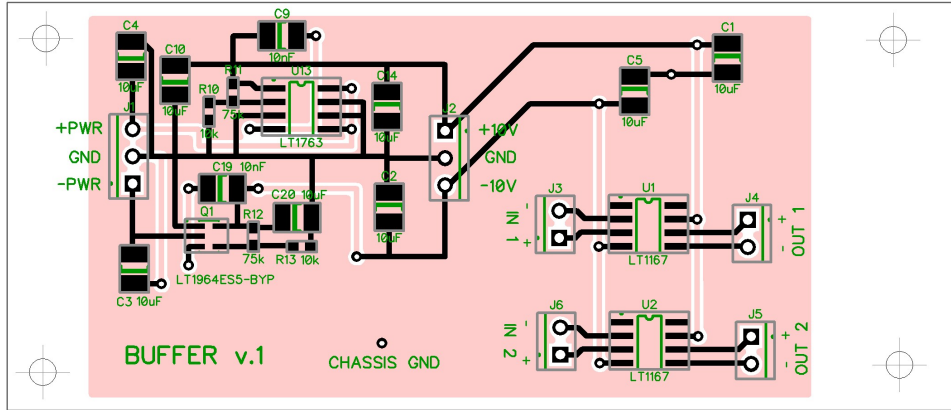
are shown in Fig. C.1, C.3, and C.4.

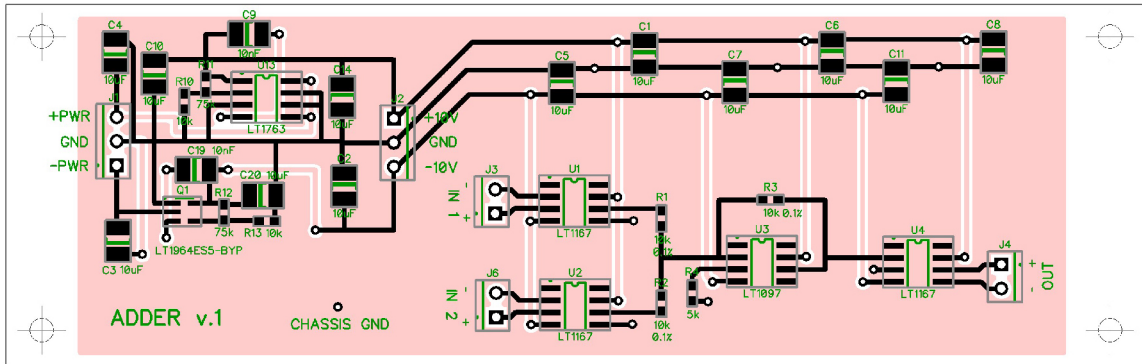Figure C.2: Schematic of buffer boards for the X, Y scanner channels.

Figure C.3: Schematic of adder board for combining AFM PID signal with the NI Z output.

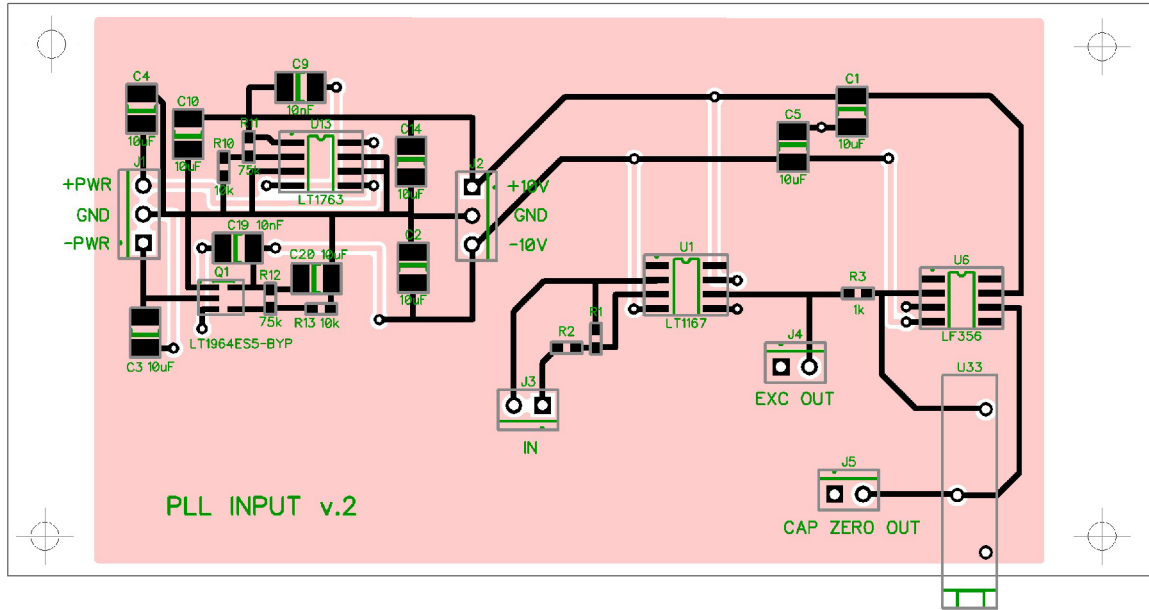[1]Designed by Wizard Matt Pelliccione

Figure C.4: Schematic of the Z buffer and capacitive offset board. EXC OUT goes to the piezo amplifier and CAP ZERO OUT goes to the 10 pF capacitor just before the Femto current amplifier. The board is used for amplitude feedback, despite its name.

C.2   AOM driver circuits

Figure C.5 has an overview of the AOM driver, used to turn the excitation beam on and off. Figures C.6 and C.7 show the schematics for analog boards used to power the Mini-Circuits RF parts and adjust the RF frequency and power going to the AOM.
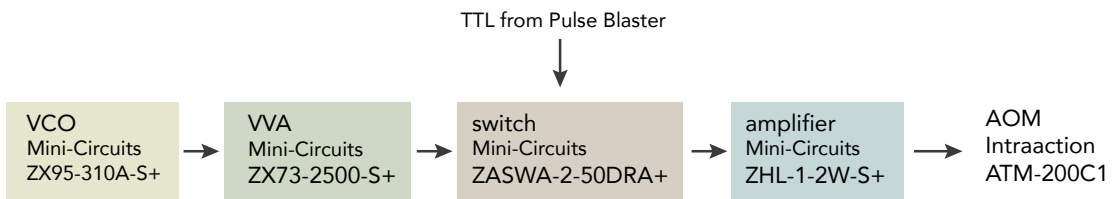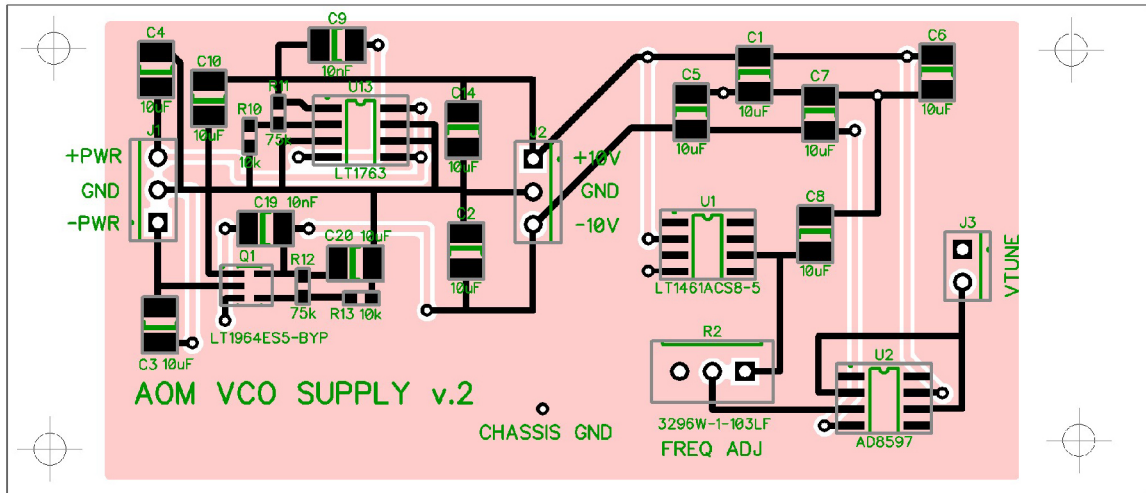

Figure C.5: Overview of the AOM driver circuit.

Figure C.6: Schematic of board for voltage controlled oscillator (VCO) power supply and frequency adjustment.
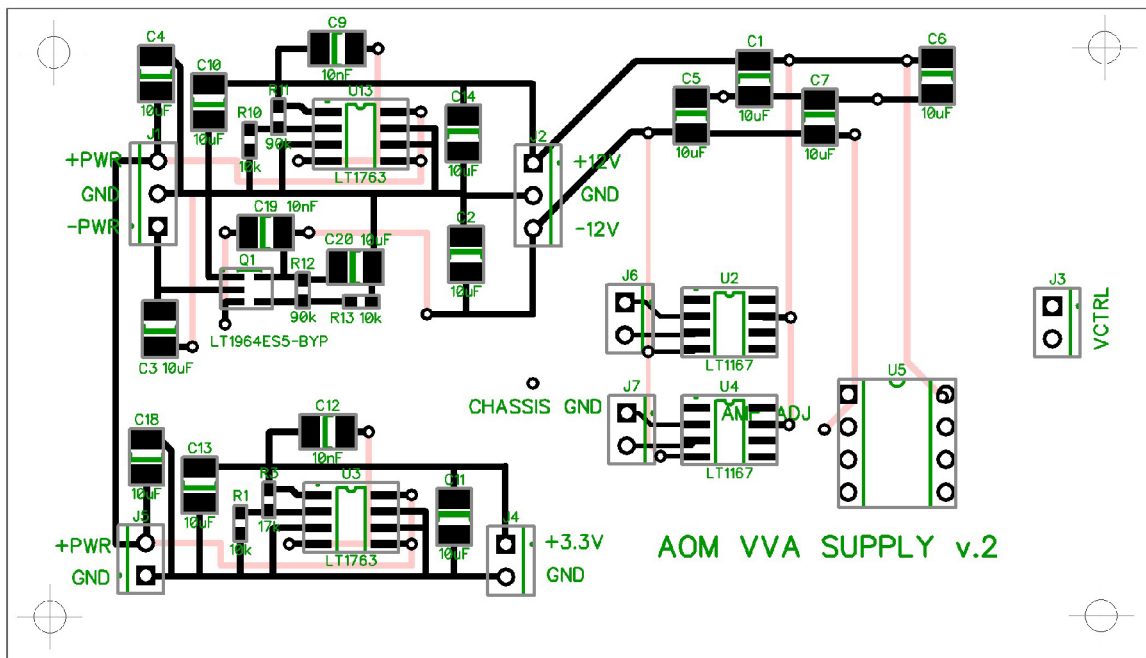
Figure C.7: Schematic of board for voltage variable attenuator (VVA) power supply and attenuation adjustement.

Appendix D

NV height calibration

The NV scan height above the magnetic CoFeB layer determines the spatial resolution of the NV imaging technique and this height an important parameter in reconstructing the magnetization. The NV height is calibrated by scanning the NV across a step edge that has been etched through the magnetic layer [65, 118]. The step edge is defined with electron beam lithography and the thin-film stack is etched with Ar ion milling. An external magnetic field is applied to saturate the film and the stray field is measured as a function of position from the step edge. Assuming a sharp step edge, with a magnetic layer thickness t much less than the NV height h, the stray field profile is given by

$$B_x = \frac{\mu_0 M_s t}{2\pi} \frac{h}{(x - x_0)^2 + h^2} \tag{D.1}$$

$$B_z = -\frac{\mu_0 M_s t}{2\pi} \frac{x}{(x - x_0)^2 + h^2} + B_{z,0} \tag{D.2}$$

where $B_{z,0}$ is the external magnetic field and the step edge runs along the line $x = x_0$.

In the presence of non-zero DMI, the magnetization rotates at the step edge [65]. This rotation angle at the edge is given by [99]

$$\theta_0 = \arcsin\left(\frac{2\Delta_{DW} D}{A_{ex}}\right) \tag{D.3}$$
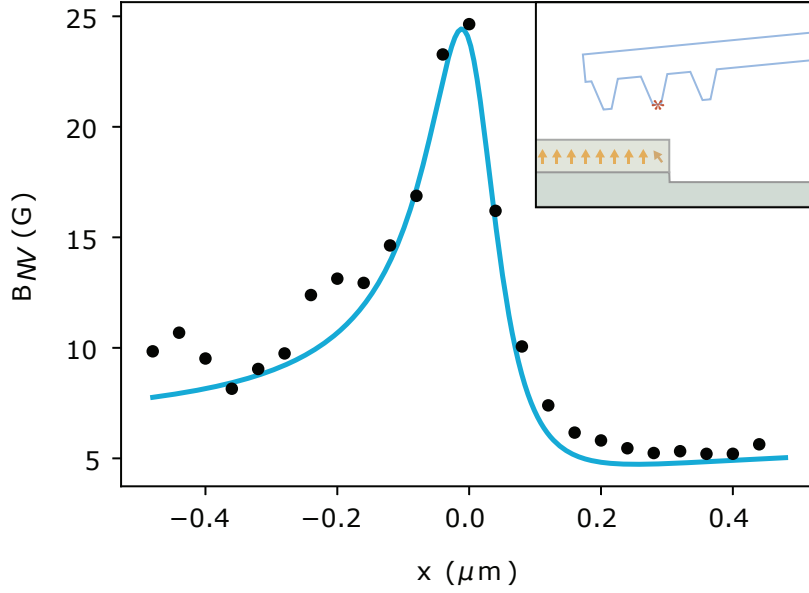
FigureD.1: NV height calibration curve example. B_{NV} is measured as a function of position across a domain wall (black). Only two parameters, NV height and lateral domain wall position, are left free in the fit (blue). (inset) NV height calibration diagram. NV scan height is determined by tip-sample tilt and location of the NV in a small array of pillars (typically 3x3 or 7x7 pillars, with 2 μm separation).

and is described by

$$\left(\frac{d\theta}{dx}\right)^2 = \frac{C + \sin^2(\theta)}{\Delta_{DW}^2} \tag{D.4}$$

which for small values of D gives,

$$\theta \approx \theta_0 e^{-|x|/\Delta_{DW}} \tag{D.5}$$

$$M_x \approx M_s \frac{2\Delta_{DW}D}{A_{ex}} e^{-|x|/\Delta_{DW}} \tag{D.6}$$

$$M_z = \sqrt{M_s^2 - M_x^2} \tag{D.7}$$

Taking this rotation into account, the stray field can be calculated as

$$B_x = -\frac{\mu_0 t}{2\pi} \int_{-\infty}^{0} dx_0 \left\{ \frac{M_x}{(x-x_0)^2+h^2} - \frac{2(x-x_0)(M_x(x-x_0)+M_z h)}{((x-x_0)^2+h^2)^2} \right\} \quad \text{(D.8)}$$

$$B_z = -\frac{\mu_0 t}{2\pi} \int_{-\infty}^{0} dx_0 \left\{ \frac{M_x}{(x-x_0)^2+h^2} - \frac{2h(M_x(x-x_0)+M_z h)}{((x-x_0)^2+h^2)^2} \right\} \quad \text{(D.9)}$$

For the low DMI Ta/CoFeB structure studied here, this magnetization rotation at the step edge gives only a few nm correction to the NV height calibration. The NV height above the CoFeB layer is extracted by fitting the stray field given by these expressions to the measured field along the NV axis. The magnetic moment density $M_s t$ is measured separately with SQUID (see Sec. S4.9). An example of one of the calibration curves is shown in Fig. SD.1. Twenty of these linecuts were taken at different points along a 2 μm length of the step edge. The measured NV height = 58$\pm$5 nm is used in for magnetization reconstruction.

The angles of the NV axis with respect to the edge and sample normal are calibrated separately using an external magnetic field. The NV height calibration depends critically on the profile of the magnetization at the etched edge. Any redeposition of magnetic material or damage to the magnetic structure at the edge induced by ion milling will lead to systematic errors in the NV height.

Appendix E

Vector field, magnetization, and current reconstruction

E.1 Reconstructing the vector magnetic field

For a magnetostatic problem (static magnetic distribution, or constant current):

$$\nabla \cdot \mathbf{B} = 0 \qquad\qquad\qquad (E.1)$$

$$\nabla \times \mathbf{B} = \mu_0 \mathbf{J} \qquad\qquad\qquad (E.2)$$

In the volume above the sample, away from any currents, $\nabla \times \mathbf{B} = 0$, and we can define a scalar potential in this volume, $\mathbf{B} = -\nabla \psi_m$. The magnetic scalar potential is a multivalued function (imagine integrating the magnetic field over a loop around a current carrying wire), but we can restrict our scalar potential to the upper volume given by a cut through the plane of the device, with $\psi_m(\mathbf{r} \to \infty) = 0$. The first Maxwell's eqn. above gives,

$$\nabla^2 \psi_m = 0 \qquad\qquad\qquad (E.3)$$

Taking the 2D Fourier transform (imaging in the x-y plane, $z = z_{NV}$),

$$\mathcal{F}[\nabla^2 \psi_m] = \frac{1}{2\pi} \int \int dx \ dy \ e^{-ik_x x} e^{-ik_y y} (\partial_x^2 + \partial_y^2 + \partial_z^2) \psi_m \tag{E.4}$$

Integrating by parts twice and throwing out the boundary terms,

$$\mathcal{F}[\nabla^2 \psi_m] = \frac{1}{2\pi} \int \int dx \ dy \ e^{-ik_x x} e^{-ik_y y} (-k_x^2 - k_y^2 + \partial_z^2) \psi_m$$
$$= (-k_x^2 - k_y^2 + \partial_z^2) \tilde{\psi}_m$$

Ignoring the boundary terms is valid as we are defining the scalar potential and the following relationship between Fourier field components in a continuous, infinite space above the device plane. Finite imaging area/boundary effects will show up when we take the discrete Fourier transform of a finite image.

A set of solutions to Laplace's equation in the upper volume are

$$\tilde{\psi}_m(k_x, k_y, z) = \tilde{\psi}_{m,0}(k_x, k_y) e^{-kz} \tag{E.5}$$

where $k = \sqrt{k_x^2 + k_y^2}$. The magnetic field components can then all be related in Fourier space. The definition of the scalar potential, $(B_x = -\partial_x \psi_m, \ B_y = -\partial_y \psi_m, \ B_z = -\partial_z \psi_m)$ gives,

$$\tilde{B}_x(k_x, k_y, z) = -ik_x \ \tilde{\psi}_m(k_x, k_y, z)$$
$$\tilde{B}_y(k_x, k_y, z) = -ik_y \ \tilde{\psi}_m(k_x, k_y, z)$$
$$\tilde{B}_z(k_x, k_y, z) = k \ \tilde{\psi}_m(k_x, k_y, z)$$

143

and the magnetic field components are related by

$$\tilde{B}_x(k_x, k_y, z) = -\frac{ik_x}{k}\tilde{B}_z(k_x, k_y, z) \tag{E.6}$$

$$\tilde{B}_y(k_x, k_y, z) = -\frac{ik_y}{k}\tilde{B}_z(k_x, k_y, z) \tag{E.7}$$

For an image of the field along the NV axis, $B_{NV} = B_x sin(\theta)cos(\phi) + B_y sin(\theta)sin(\phi) + B_z cos(\theta)$, or in Fourier space,

$$\tilde{B}_{NV} = \left(-\frac{ik_x}{k}sin(\theta)cos(\phi) - \frac{ik_y}{k}sin(\theta)sin(\phi) + cos(\theta)\right)\tilde{B}_z \tag{E.8}$$

and the Fourier components of B_z field can be calculated from the components of $\tilde{B}_{NV}$,

$$\tilde{B}_z = \frac{\tilde{B}_{NV}}{-\frac{ik_x}{k}sin(\theta)cos(\phi) - \frac{ik_y}{k}sin(\theta)sin(\phi) + cos(\theta)} \tag{E.9}$$

Using the relations between $\tilde{B}_z$, $\tilde{B}_x$, and $\tilde{B}_y$, the other vector field Fourier components be calculated. However, there is a singularity at $k = 0$, so the $k = 0$ component is set to zero in the reconstruction. This means that any constant components of the magnetic field will be lost.

In the vector field reconstruction from measured field data, these components are calculated in terms of a discrete Fourier transform of B_{NV}, which implicitly assumes periodic boundary conditions. If a large enough image is taken, so that the field is constant around the border and its gradients are zero at the image edges, then the DFT will not adversely affect the reconstruction. On the other hand, if the field is different on opposite sides of the image or the field gradients are large at the image edges, the DFT of B_{NV} will contain high frequency artifacts due to any mismatch in opposite border fields and lower frequency artifacts components due to the any mismatch in the field gradients

on opposite images edges. These artifacts will distort the reconstructed field components when transforming back into real space, most significantly at the edges of the image.

E.2   Reconstructing helicity angle

Constructing the underlying magnetization pattern from a stray field measurement is not trivial. The mapping from magnetization to stray field is not one-to-one and cannot be inverted. In order to say anything about the magnetization pattern given the measured stray field, we must measure several materials parameters and make further assumptions based on micromagnetic theory. Recent studies dealing with these issues have taken two main approaches: assume a domain wall profile based on micromagnetic theory [65, 66], or fix a local magnetization gauge or helicity angle ψ_h [28]. The first method has the advantage that the local helicity angle can be extracted and need not be assumed as fixed along the entire length of a domain wall, but the second method has the nice property that it does not rely on an analytic form of the domain wall profile (DMI will lead to deviations in domain wall shape [162]). In this work we use the reconstruction methods described in [28] to estimate the domain wall position in the Bloch magnetization gauge ($|\psi_h| = 0$), but then fix the magnetization pattern using the analytic form of a thin film domain wall to calculate the stray magnetic field as a function of helicity angle magnitude.

For the low external fields used in these measurements, the stray field along the NV axis changes sign at different points in the imaging plane. Since the NV measures only the absolute value of the stray field, estimation of the domain wall position requires us to assign a polarity to regions of the image separated by zero-field contours. Reconstruction of the full vector magnetic field can then proceed as described in [28, 125] and above in E.1. The M_z component of magnetization is easily calculated in the Bloch gauge by

projecting Fourier components of the stray field $\tilde{B}_z(\mathbf{k}, z)$ down to the sample surface using a stray field transfer function $\alpha(\mathbf{k}, z, t)$, similar to [163],

$$\alpha(\mathbf{k}, z, t) \equiv \frac{1}{2} e^{-kz} \left(1 - e^{-kt} \right) \tag{E.10}$$

$$\tilde{M}_z(\mathbf{k}) = \frac{\tilde{B}_z(\mathbf{k}, z)}{k\alpha(\mathbf{k}, z, t)} \tag{E.11}$$

In our case, this procedure leads to amplification of image noise because of the somewhat large NV scan height. M_z is then used to find the position of the domain wall, but is not used to simulate the stray field. The magnetization components calculated relative to the domain wall position are

$$M_z = M_s \tanh \left(\frac{x_\perp}{\Delta_{DW}} \right) \tag{E.12}$$

$$M_\perp = M_s \cos(\psi_h) \operatorname{sech} \left(\frac{x_\perp}{\Delta_{DW}} \right) \tag{E.13}$$

$$M_\parallel = M_s \sin(\psi_h) \operatorname{sech} \left(\frac{x_\perp}{\Delta_{DW}} \right) \tag{E.14}$$

$$|\psi_h| = \begin{cases} 0, & D > D_c \\ \arccos\left(\frac{D}{D_c} \right), & |D| < D_c \\ \pi, & D < -D_c \end{cases} \tag{E.15}$$

where $D_c = 2\ln(2)\mu_0 M_s^2 t/\pi^2$. Using the BLS value of D, the expected helicity angle is $|\psi_h| \simeq 53°$. Assuming a fixed helicity angle, the best fit helicity magnitudes given by the images in Figure 6, SE.1, and SE.2 are 58°, 75°, and 72° respectively. The best fit helicity magnitudes correspond to the angles that minimize the RMS error between the measured

and simulated stray field in a 1.4 μm box around each bubble. Figure SE.3 shows the average RMS error per pixel over the whole range of helicity angle magnitude for the three bubbles. The best fit helicity values depend on the extracted material parameters described in section 4.2.1, and as such, the main source of uncertainty in determining these values is due to a possible systematic error caused by an unknown magnetic dead layer thickness. Using the material parameters extracted for the case of the 0.36 nm thick magnetic dead layer described in section 4.2.1, the best fit helicity magnitudes for the skyrmion bubbles in Figure 6, SE.1, and SE.2 are 73°, 86°, and 85° respectively.

Another source of error in the extraction of helicity angle magnitude comes from static fluctuations in the stray field due to variations in the magnetic surface density I_s. These fluctuations can be seen in a stray field measurement of the saturated state. Figure SE.4 shows these stray field fluctuations in the same imaging area as shown in Fig. 6 of the main text, but at larger external field $B_{ext} = 12$ G. In other works these fluctuations have been attributed to fluctuations in local magnetization magnitude or film thickness [68, 164].

Figure E.1: Magnetization reconstruction example. (a) Measured absolute value of the magnetic field along the NV axis. (b) The simulated magnetic field along the NV axis for the best fit helicity angle 75°. (c) Linecuts at various angles ϕ across the magnetic bubble, comparing the measured magnetic field shown in (a) to the simulated field for four domain wall types— right-handed Néel, Bloch, left-handed Néel, and a domain wall with $|\psi_h| = 75°$. The NV height is calibrated to be 77 ± 4 nm. The NV angle relative to the film normal is measured as $61° \pm 4°$ using an external field aligned along the film normal. The in-plane NV angle is extracted from the B_{NV} bubble image by finding the direction of maximum field gradient at the domain wall and is $-4° \pm 1°$ relative to the image x-axis.
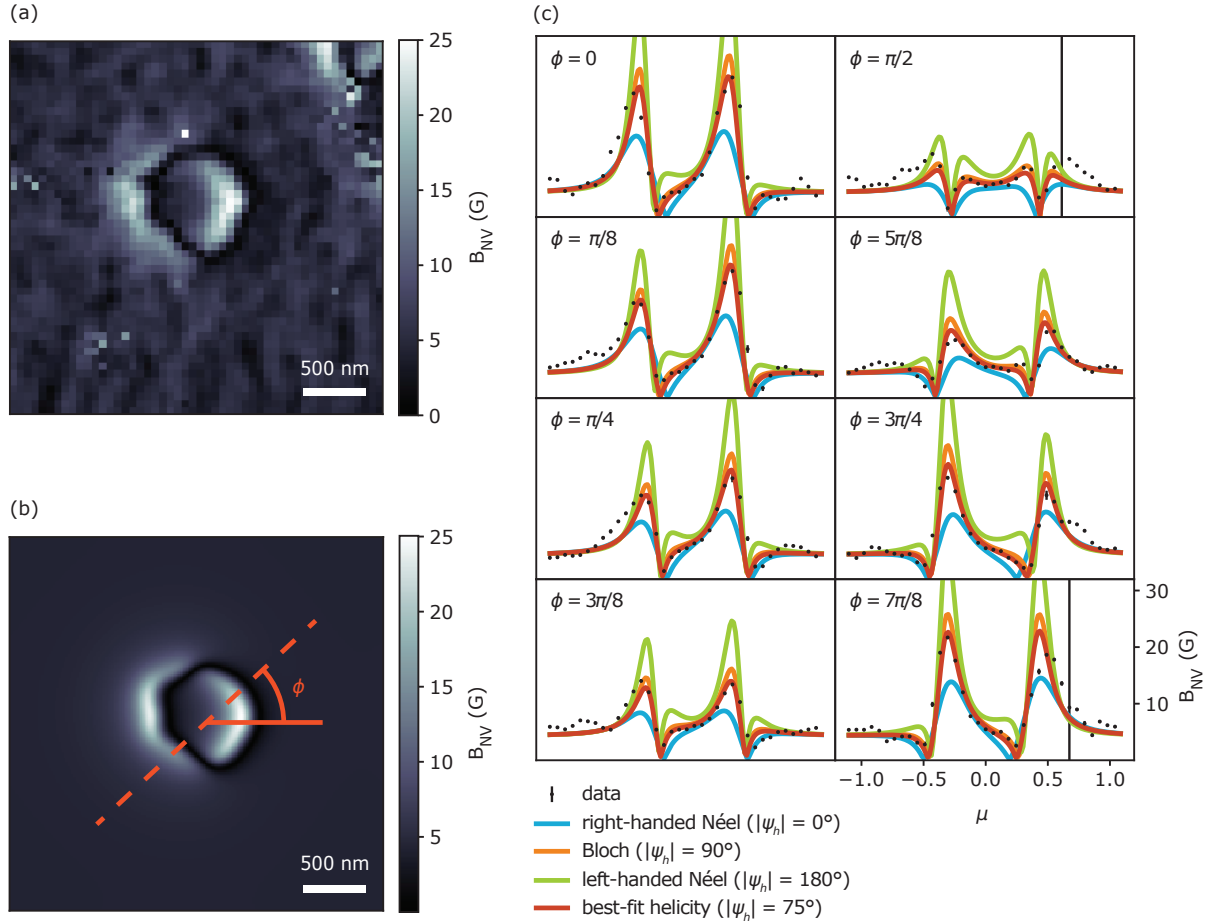
148
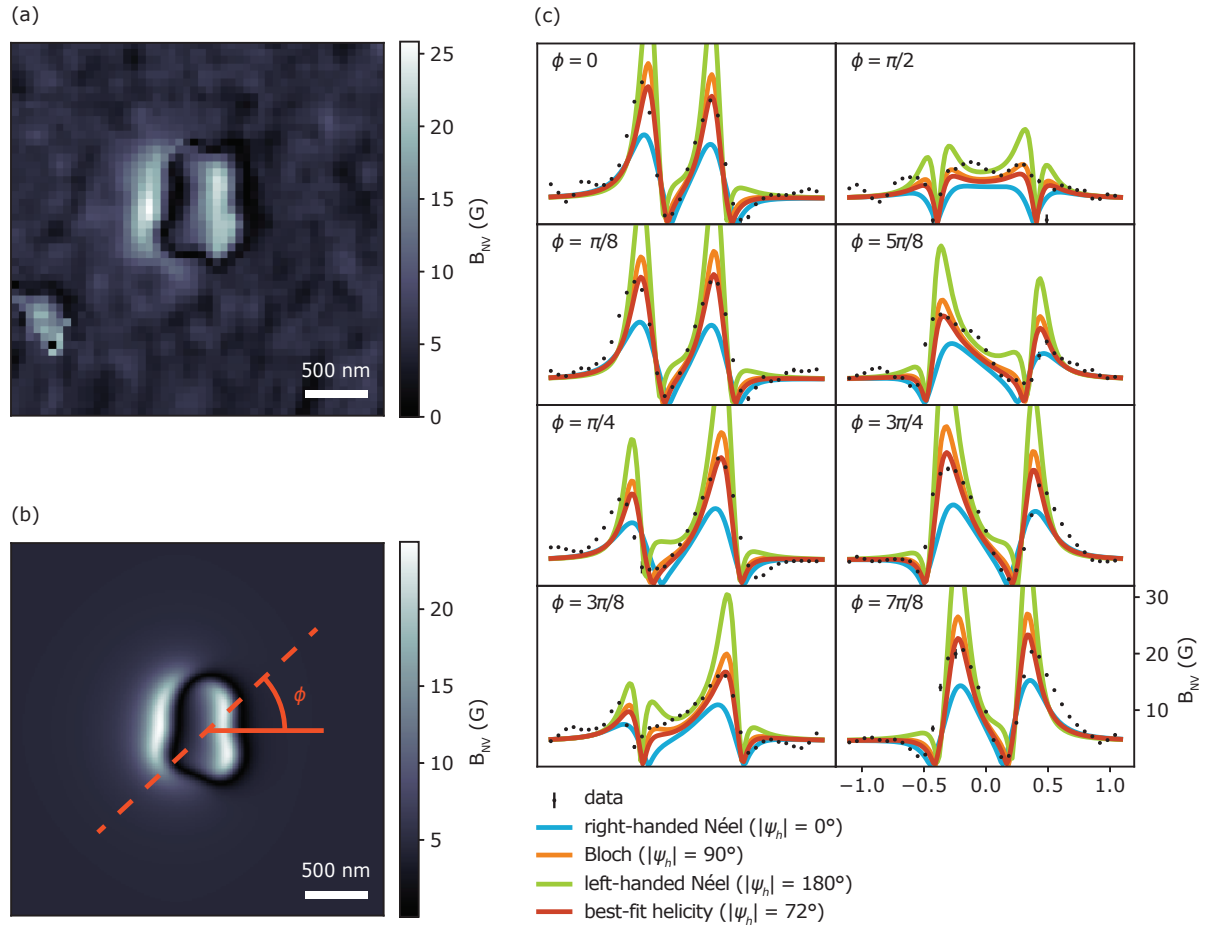
Figure E.2: Magnetization reconstruction example. (a) Measured absolute value of the magnetic field along the NV axis. (b) The simulated magnetic field along the NV axis for the best fit helicity angle 72°. (c) Linecuts at various angles ϕ across the magnetic bubble, comparing the measured magnetic field shown in (a) to the simulated field for four domain wall types— right-handed Néel, Bloch, left-handed Néel, and a domain wall with $|\psi_h| = 72°$. The same NV is used as in Fig. SE.1, with parameters, angle relative to the film normal = $61° \pm 4°$, in-plane NV angle = $-4° \pm 1°$ relative to the image x-axis, NV height = 77 ± 4 nm.
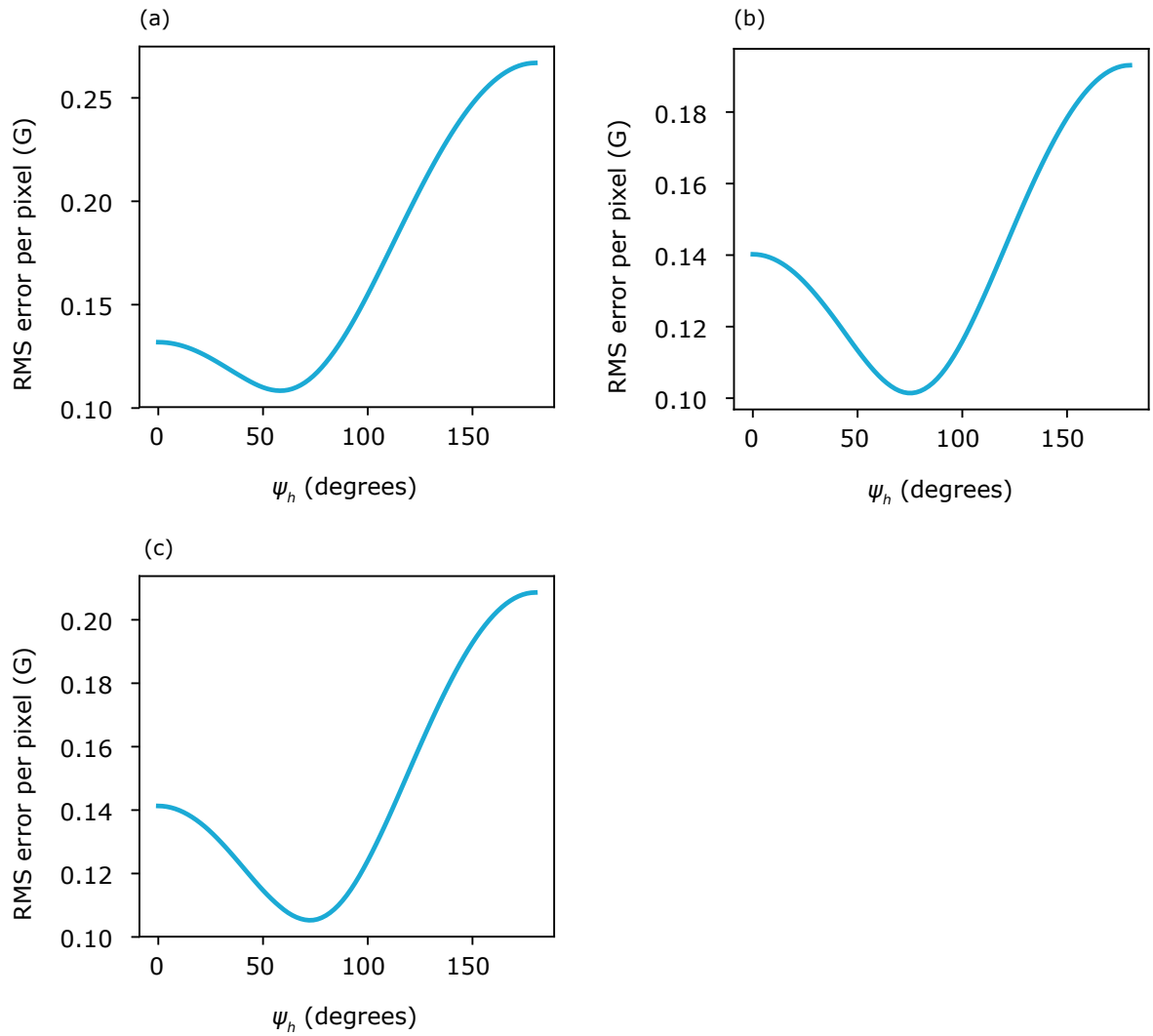
Figure E.3: RMS differences in measured vs. simulated stray field as a function of the helicity angle in a 1.4 μm box centered on each bubble. (a) skymion bubble in Fig. 6, (b) skymion bubble in Fig. SE.1, (c) skymion bubble in Fig. SE.2.
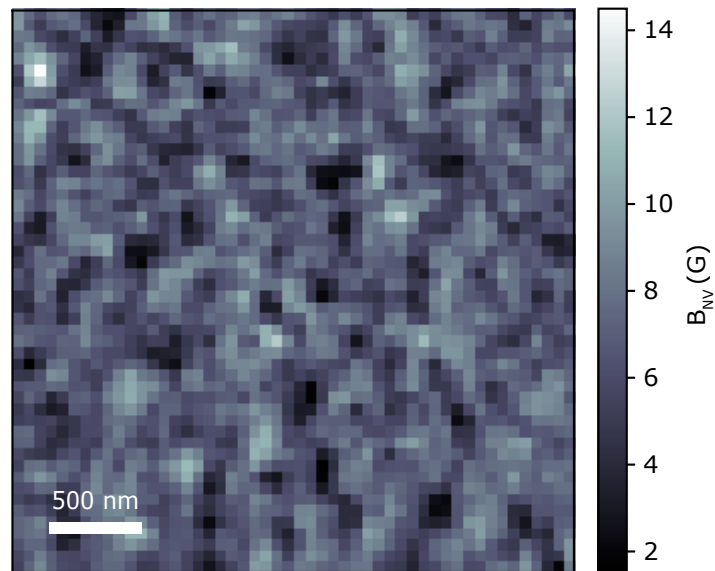
Figure E.4: Measured magnetic field along NV axis for saturated magnetic state at $B_{ext} = 12$ G in the same image are as that of Fig. 6 of the main text. Fluctuations in the measured stray field are static and are attributed to fluctuations in the parameter $I_s = M_s t$, coming from either fluctuations in the film thickness or local magnetic saturation.

E.3   Current reconstruction

(a)

(b)
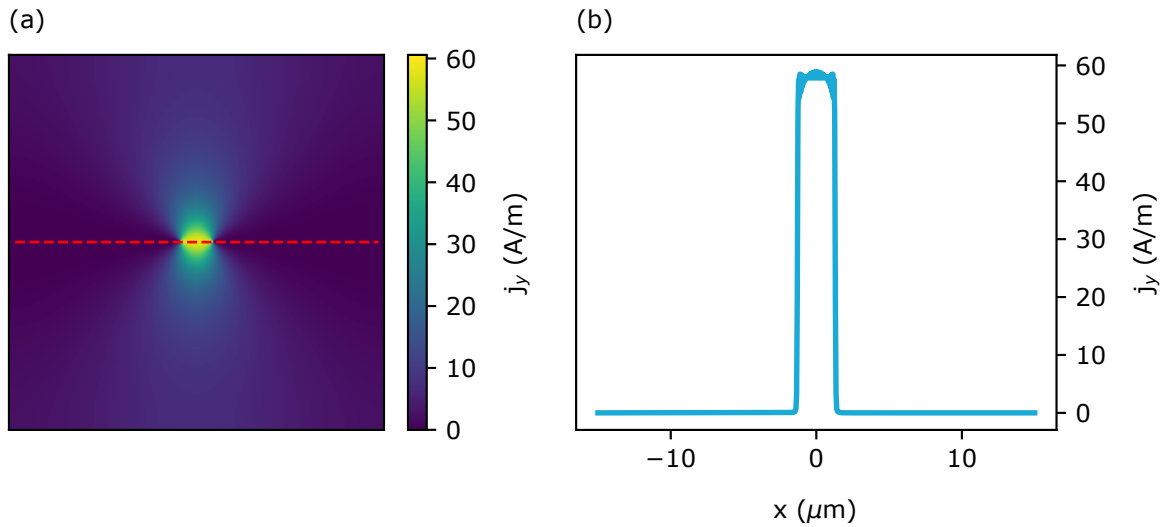
Figure E.5: (a) Simulated j_y with w=2.7 μm, $l_{ee} = 10$ μm, and $l_{mr} = 25$ μm. (b) Linecut across the simulated j_y at the position of the slit, given by the dashed red line in (a).

An example of the reconstruction procedure will be given below for simulated stray field data from a ballistic flow profile through a slit and for measured stray field data for current flow through our slit near CN at room temperature. The current density is calculated using the algorithm[1], taken from [149]. The algorithm calculates the 2D current density for a slit of width w, in an area of size L_x by L_y with periodic boundary conditions. If L_x and L_y are large, then the current distribution will be a good approximation to a single slit embedded in a device with dimensions much larger than the slit width. The depth of the slit is assumed to be much smaller than the width. The simulation also takes the electron-electron scattering length l_{ee} and momentum relaxing scattering length l_{mr} as input parameters. Different regimes can be be simulated by varying these parameters relative to each other and relative to the slit width w. Below we take w=2.7 μm, $l_{ee} = 10$ μm, and $l_{mr} = 25$ μm to simulate the regime of ballistic flow. This regime

---

[1]provided by Andrew Lucas

is chosen because the artifacts of the reconstruction process are especially clear when reconstructing the square, ballistic current density profile in the slit.

The resulting current distribution is used to calculate the stray magnetic field at a height of $z = 129$ nm. The components of the stray magnetic field are shown in Fig. E.6, along with the field along the NV axis. The reconstruction is then performed on the simulated B_{NV} data. First the B_x and B_z components of the field are reconstructed from B_{NV}. Figure E.7 gives a comparison between the initial B_x and B_y and the reconstructed components. The finite image artifacts discussed above are visible, particularly in the reconstructed B_x, which has a constant offset and also large deviations from the starting B_x at the left and right image edges.

The current density is then calculated from the reconstructed B_x and B_y. When calculating the current density, a Gaussian filter is applied in k-space with width given by the NV height. This smooths the current density over the length scale of the NV height, but it also controls the amplification of higher frequency noise. The resulting reconstructed current distribution is shown in Fig. E.8.
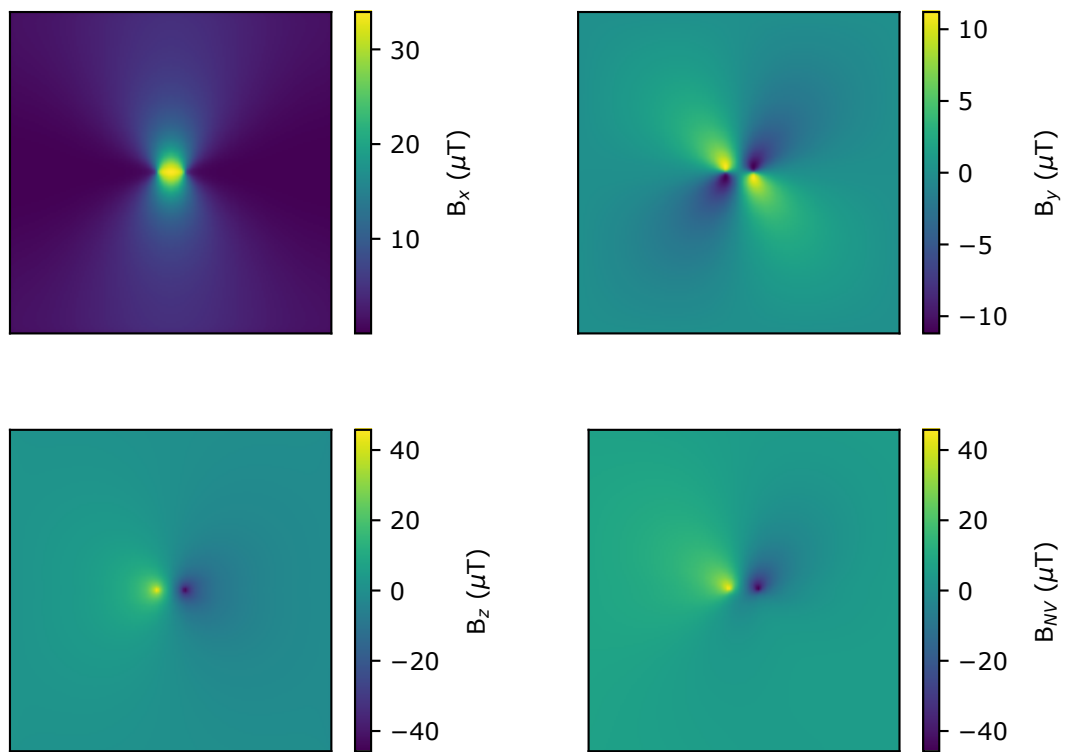
Figure E.6: Simulated magnetic field components for the ballistic current distribution.
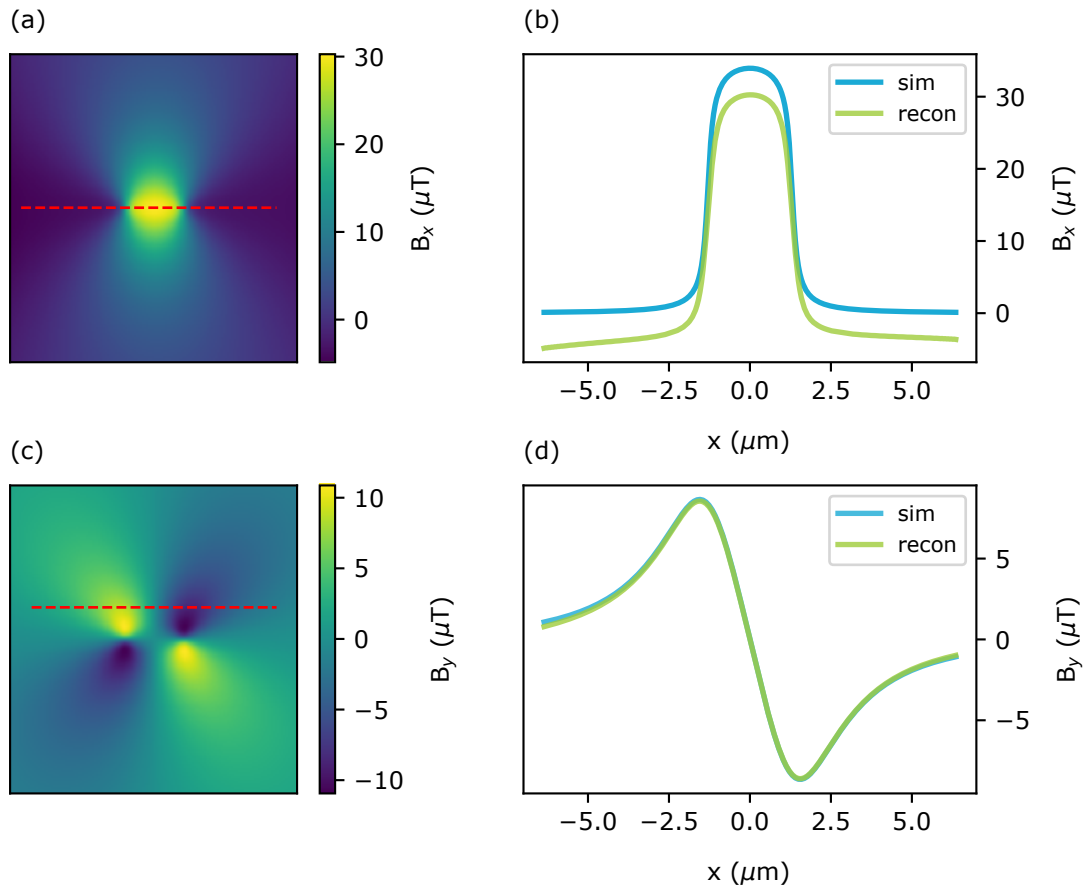
Figure E.7: Comparison between the initial and reconstructed B_x and B_y fields. (a)B_x reconstructed. (b) Comparison of initial and reconstructed linecuts across B_x at the position of the slit, given by the dashed red line in (a). (c)B_y reconstructed. (d) Comparison of initial and reconstructed linecuts across B_y at the position given by the dashed red line in (a).
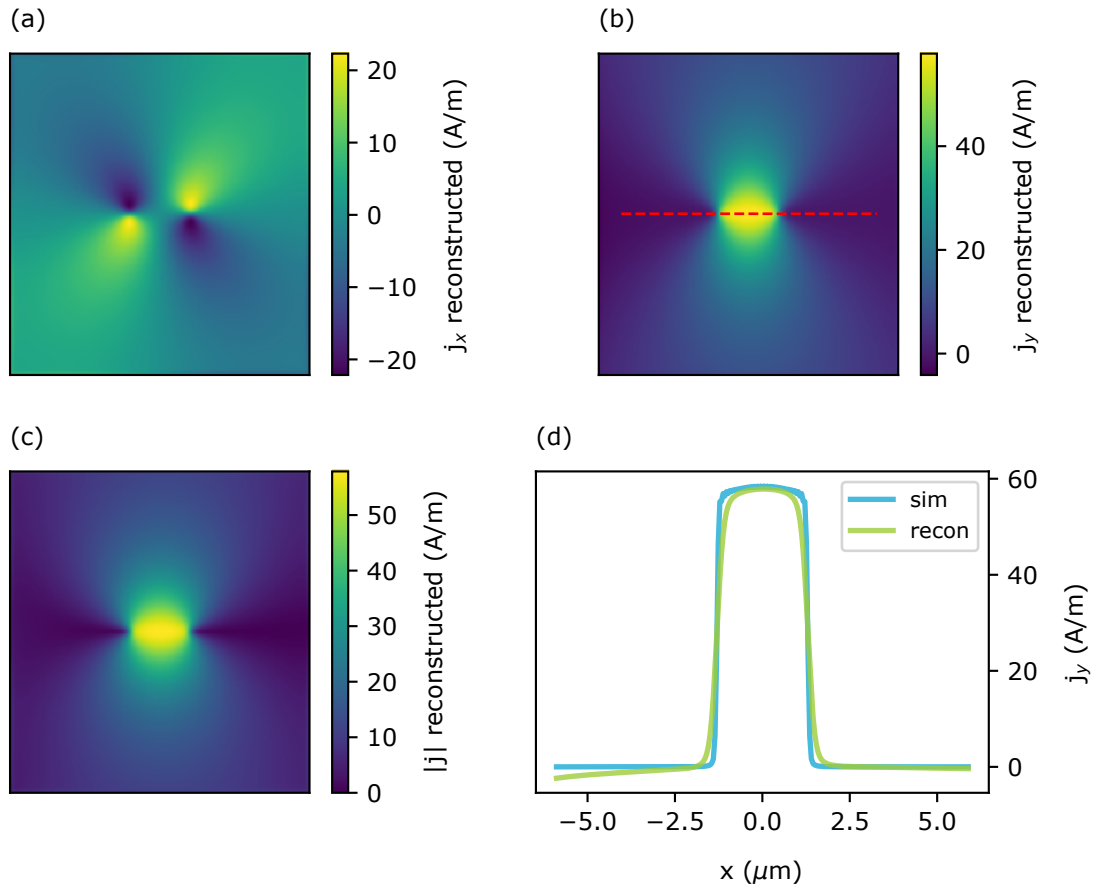
Figure E.8: Current density reconstructed from the simulated B_{NV}. The j_x (a), j_y (b) components give current density magnitude $|j|$ in (c). A comparison between the starting and reconstructed components j_y is shown in the linecut in (d). The cut is taken across the slit, given by the dashed red line in (b). The k-space filter leads to the slight rounding of the current density at the edges of the slit. The finite image, edge effect of the vector field reconstruction shows up in the left and right edges of the reconstructed j_y

.
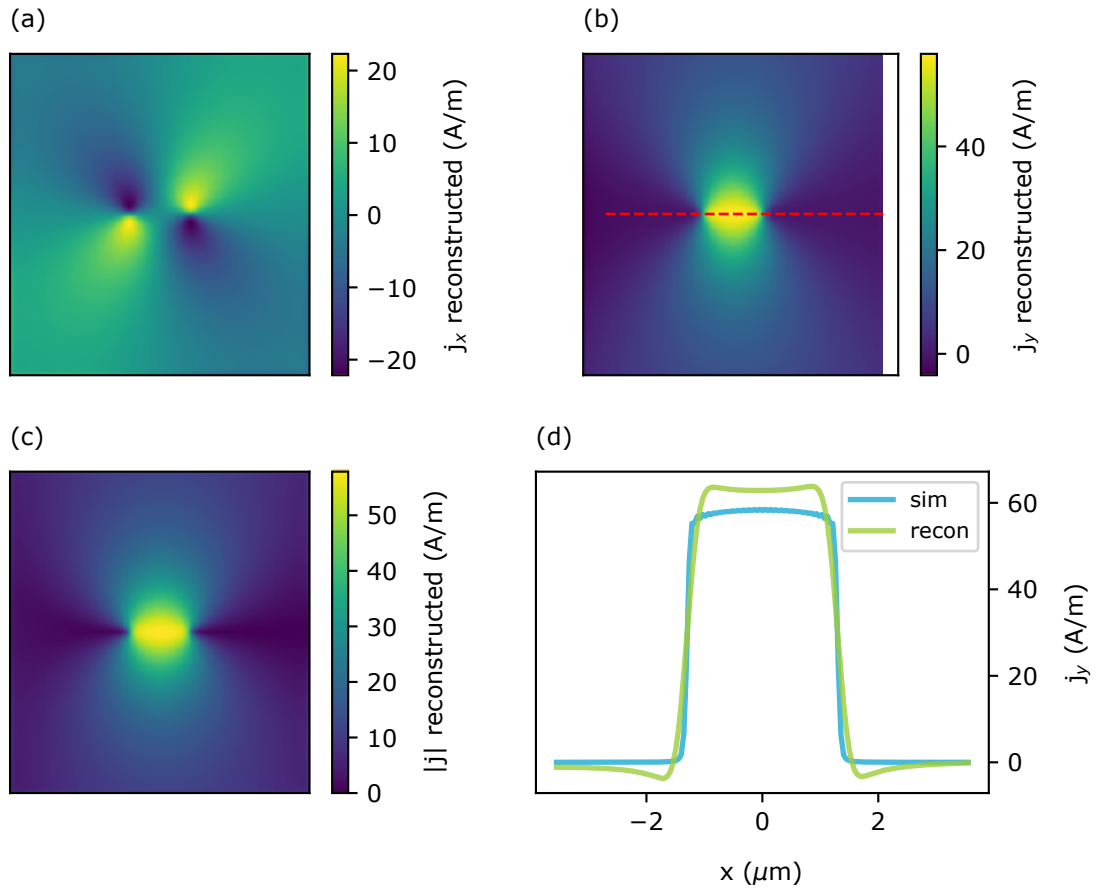
Figure E.9: Current density reconstructed from the simulated B_{NV}, using the incorrect NV height $z_{NV} = 200$ nm, starting from simulated field data at $z = 138$ nm. Using a height in the reconstruction that is greater than the measurement height leads to over sharpening of the current density at the slit edges, giving slight Ohmic peaks even when starting from a ballistic profile.

Appendix F

Stray electric field effects

The NV spin levels are sensitive to electric fields through spin-spin and spin-orbit coupling. Treating the effect of strain as an effective local electric field $\boldsymbol{\sigma}$, combined with an external electric field $\mathbf{E}$, NV transition frequencies shift in the presence of an external electric field as [165],

$$
\Delta f_{+/-} = d_{\parallel}\Pi_z \pm \left\{ \sqrt{\gamma^2 B_z^2 + d_{\perp}^2 \Pi_{\perp}^2 - \frac{\gamma^2 B_{\perp}^2 d_{\perp}\Pi_{\perp}}{D}cos\left(2\phi_B + \phi_{\Pi}\right) + \frac{\gamma^4 B_{\perp}^2}{4D^2}} \right.
$$
$$
\left. - \sqrt{\gamma^2 B_z^2 + d_{\perp}^2 \sigma_{\perp}^2 - \frac{\gamma^2 B_{\perp}^2 d_{\perp}\sigma_{\perp}}{D}cos\left(2\phi_B + \phi_{\sigma}\right) + \frac{\gamma^4 B_{\perp}^2}{4D^2}} \right\}
$$

where $\boldsymbol{\Pi} = \boldsymbol{\sigma} + \mathbf{E}$, $\phi_B = \arctan(B_y/B_x)$, $\phi_{\Pi} = \arctan(\Pi_y/\Pi_x)$. The parallel and perpendicular coupling parameters are $d_{\parallel} = 0.35$ Hz cm/V and $d_{\perp} = 17$ Hz cm/V [166]. In our scanning graphene measurements, the strain is small, $B_{\perp} \ll D$, $B_{\perp} \lessgtr B_z$, $d_{\perp}E_{\perp}/\gamma B_z \ll 1$, and the shift in transition frequencies due to an external electric field become

$$
\Delta f_{+/-} \simeq d_{\parallel}E_z \pm \frac{\left(d_{\perp}E_{\perp}\right)^2}{\gamma|B_z|} \tag{F.1}
$$

In our scanning measurements, measure the shift due to magnetic fields by measuring the NV transition frequencies with current $\pm I$ and take the frequency difference to subtract off the shifts in the NV frequency due to static electric fields. This works well if the

electric field due to the gate-sample potential difference V_{gs} is constant, but in the case where the source voltage bias V_s is large, the stray electric field will change when changing the current flow direction. In this case, the differential frequency measurement using $\pm I$ will not completely cancel the shifts in the NV frequency due to the electric field. Let $\boldsymbol{\alpha}$ be the stray electric field above the sample normalized by the gate-sample voltage, $\mathbf{E} = \boldsymbol{\alpha}V_{gs} = \boldsymbol{\alpha}(V_g - V_s)$, where V_g is the voltage applied to the gate relative to ground. After performing the differential frequency measurement, the remaining shifts due to the parallel and perpendicular electric fields are

$$\Delta f_{||} \approx 2d_{||}\alpha_{NV}V_s \tag{F.2}$$

$$\Delta f_{\perp} \approx 4\frac{\alpha_{\perp}^2 d_{\perp}^2}{\gamma|B_{NV}|}V_g V_s \tag{F.3}$$

F.1 Stray electric fields from graphene devices
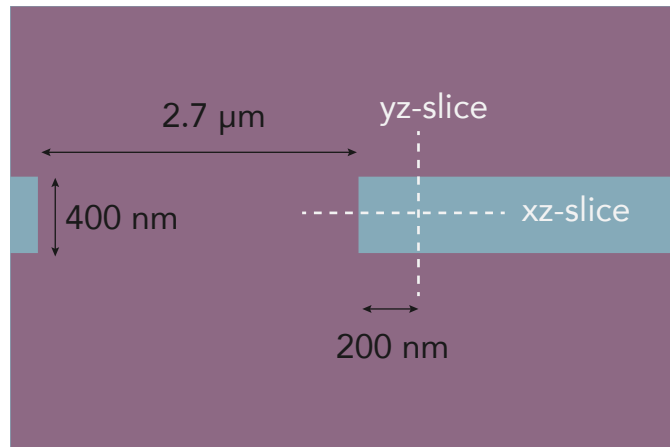
Figure F.1: Diagram of the simulation dimensions of the graphene constriction. The graphene area is purple. The dashed white lines indicate the xz and yz cut planes electric field slices shown in Fig. F.2 and Fig. F.3.

The stray electric field above the graphene device can be simulated using Comsol.

159

Figure F.2 shows a cut through the magnitude of the stray electric field in a slice through the graphene device, normalized by the gate-graphene potential difference, in the yz-plane, 200 nm from the side of the constriction. Figure F.3 shows a cut through the magnitude of the stray electric field in a slice through the graphene device, normalized by the gate-graphene potential difference, in the xz-plane, centered on the middle of the constriction. Figure F.4 shows 1D linecuts through the simulated electric field magnitude in the minimum-height NV scan plane. The relative permittivity of the hBN layers is taken to be $\epsilon_r = 3.0$ in these simulations.
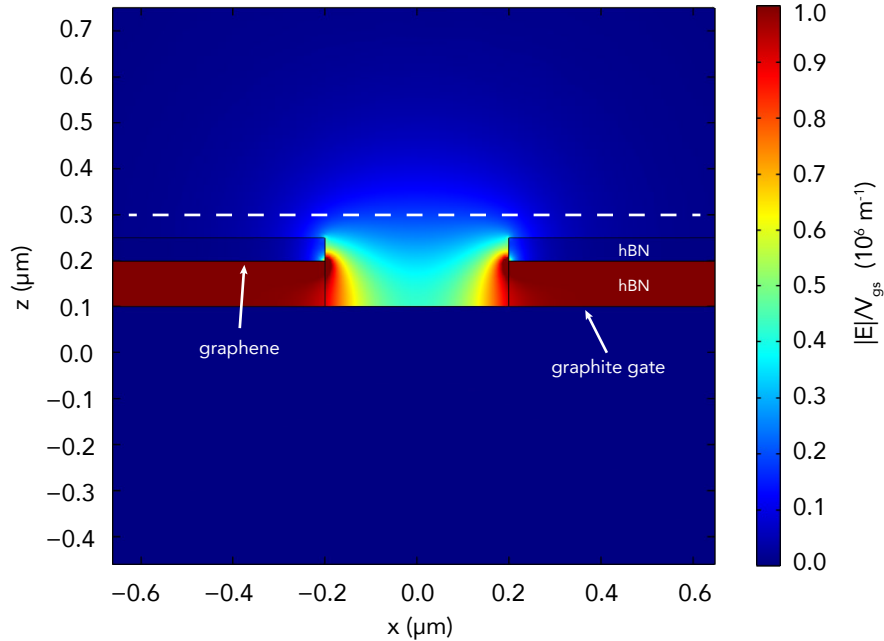
Figure F.2: Magnitude of the electric field, normalized by the gate-graphene potential difference V_{gs}, in a yz-plane slice through the graphene device 200 nm from the side of the constriction. The white dashed line indicates the minimum scan height of the NV. The black lines outline the hBN layers.

This minimum-height electric field magnitude can be used to calculate the worst-case frequency shifts in the differential NV signal. For a the measured contact resistances of a couple kΩs, and carrier densities $> 5 \times 10^{11}/\text{cm}^2$, the bias-induced potential at
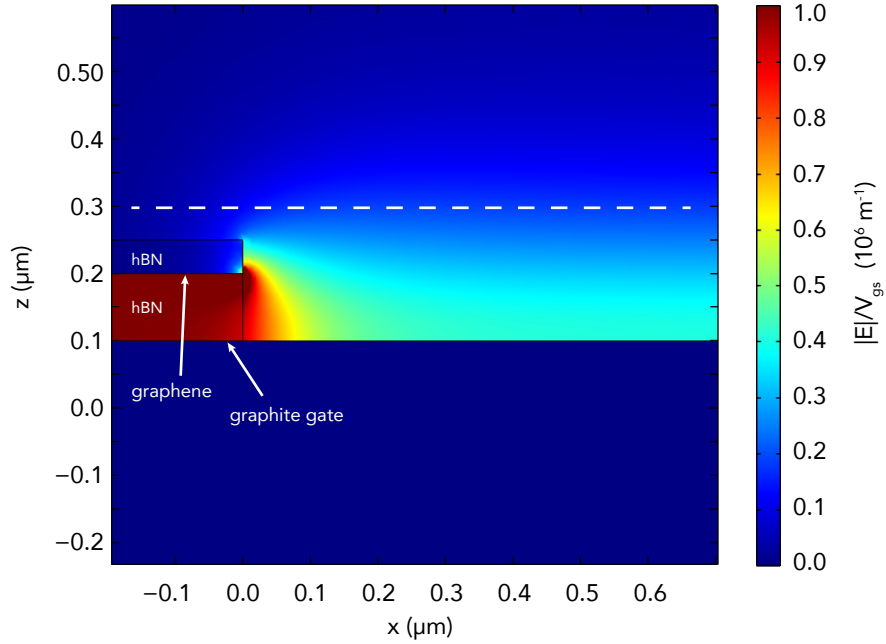
Figure F.3: Magnitude of the electric field, normalized by the gate-graphene potential difference V_{gs}, in an xz-plane slice through the graphene device center on the middle of the constriction. The white dashed line indicates the minimum scan height of the NV. The black lines outline the hBN layers.

the constriction is dominated by the contact resistance and this potential can be a few hundred mV. Taking a worst-case $V_s = 0.3$ V, and using the maximum, normalized electric field magnitude 2×10^6 m^{-1}, the maximum shifts in the NV frequency that are not canceled by the differential measurement are calculated from Eqns. F.2 and F.3. As Eqn. F.3 indicates, the shift due to a perpendicular electric field can be suppressed by applying a magnetic field along the NV axis. For example, for $B_{NV} = 10$ G, the magnetic field suppresses the differential-remnant frequency shift from this worst-case electric field to ∼12 kHz. The parallel electric shift is not suppressed by the external magnetic field, but coupling parameter $d_{\parallel}$ is smaller and the remnant shifts due to a worst-case parallel electric field is roughly 4 kHz. For comparison, the typical photon-collection noise in these 2D graphene scanning measurements is ∼ 1 μT, or a frequency shift of 28 kHz.
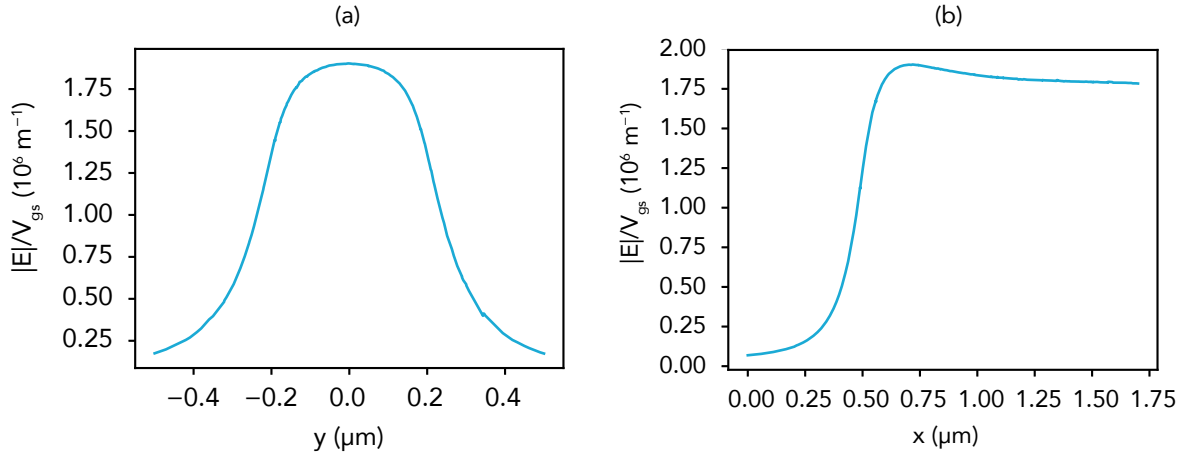
Figure F.4: (a) Linecut through the normalized electric field magnitude at $x = 200$ nm from the constriction side and $z = 100$ nm above the graphene (the minimum NV scan height). (b) Linecut through the normalized electric field magnitude at $y = 0$ (constriction center) and $z = 100$ nm above the graphene (the minimum NV scan height).

This implies that the stray electric field is not causing large systematic errors in NV measurement of stray magnetic field. However, the static shifts in the NV frequency due to the the stray electric field in the large gate voltage regime can be quite large. For the same external magnetic field $B_{NV} = 10$ G, a gate voltage of $V_g = 6$ V can give worst-case shifts due to the perpendicular electric field of ~ 0.5 MHz. These shifts are not negligible on the scale of the magnetic 10 µT scale fields we are detecting due to the current flow, but the differential measurement using $\pm I$ cancels most of this stray electric field effect.

Despite this calculation showing that the stray electric fields are likely not giving rise to systematic errors in the measured stray magnetic field, there is an unresolved and possibly electric-field-related measurement effect near the edges of the graphene device constrictions or near some graphene device edges. In some scans, a decrease in the NV sensitivity is observed at a particular corner of the constriction, and the corner that this occurs at depends on the orientation of the NV. The effect seems to be accompanied by an increase in the Rabi time and an increase in the asymmetry in the depth of the

162

two NV spin state transitions. These effects could be also result from the coupling of microwaves to currents inside the graphene device, which could produce large, phase-shifted microwave fields near narrow, high-current density areas of the device.

Bibliography

[1] J. H.N. Loubser and J. A. Van Wyk. Electron spin resonance in the study of diamond. *Reports on Progress in Physics*, 41(8):1201–1248, 1978.

[2] A. Lenef and S. C. Rand. Electronic structure of the N- V center in diamond: Theory. *Physical Review B*, 53(20):13441–13455, 1996.

[3] A Gruber, A. Dräbenstedt, C Tietz, L Fleury, J Wrachtrup, and C. Von Borczyskowski. Scanning confocal optical microscopy and magnetic resonance on single defect centers. *Science*, 276(5321):2012–2014, 1997.

[4] P Neumann, R Kolesov, V Jacques, J Beck, J Tisler, A Batalov, L Rogers, N B Manson, G Balasubramanian, F Jelezko, and J Wrachtrup. Excited-state spectroscopy of single NV defects in diamond using optically detected magnetic resonance. *New Journal of Physics*, 11(1):013017, 2009.

[5] Yuchen Ma, Michael Rohlfing, and Adam Gali. Excited states of the negatively charged nitrogen-vacancy color center in diamond. *Physical Review B - Condensed Matter and Materials Physics*, 81(4):041204, 2010.

[6] Jeronimo Rios Maze. *Quantum manipulation of nitrogen-vacancy centers in diamond: from basic properties to applications*. PhD thesis, Harvard, 2010.

[7] J R Maze, A Gali, E Togan, Y Chu, A Trifonov, E Kaxiras, and M D Lukin. Properties of nitrogen-vacancy centers in diamond: The group theoretic approach. *New Journal of Physics*, 13(2):025025, 2011.

[8] Marcus W. Doherty, Neil B. Manson, Paul Delaney, Fedor Jelezko, Jörg Wrachtrup, and Lloyd C.L. Hollenberg. The nitrogen-vacancy colour centre in diamond. *Physics Reports*, 528(1):1–45, 2013.

[9] L J Rogers, S Armstrong, M J Sellars, and N B Manson. Infrared emission of the NV centre in diamond: Zeeman and uniaxial stress studies. *New Journal of Physics*, 10(10):103024, 2008.

[10] V. M. Acosta, A. Jarmola, E. Bauch, and D. Budker. Optical properties of the nitrogen-vacancy singlet levels in diamond. *Physical Review B - Condensed Matter and Materials Physics*, 82(20):201202, 2010.

[11] Michael Tinkham. *Group Theory and Quantum Mechanics.* Dover Publications, 1992.

[12] Kenneth William Lee. *Coherent dynamics of a hybrid quantum spin-mechanical oscillator system.* PhD thesis, University of California, Santa Barbara, 2017.

[13] N. B. Manson, J. P. Harrison, and M. J. Sellars. Nitrogen-vacancy center in diamond: Model of the electronic structure and associated dynamics. *Physical Review B - Condensed Matter and Materials Physics*, 74(10):104303, 2006.

[14] M. L. Goldman, A. Sipahigil, M. W. Doherty, N. Y. Yao, S. D. Bennett, M. Markham, D. J. Twitchen, N. B. Manson, A. Kubanek, and M. D. Lukin. Phonon-induced population dynamics and intersystem crossing in nitrogen-vacancy centers. *Physical Review Letters*, 114(14):145502, 2015.

[15] L J Rogers, R L McMurtrie, M J Sellars, and N B Manson. Time-averaging within the excited state of the nitrogen-vacancy centre in diamond. *New Journal of Physics*, 11(6):063007, 2009.

[16] J. P. Tetienne, L Rondin, P Spinicelli, M Chipaux, T Debuisschert, J. F. Roch, and V Jacques. Magnetic-field-dependent photodynamics of single NV defects in diamond: An application to qualitative all-optical magnetic imaging. *New Journal of Physics*, 14(15pp):103033, 2012.

[17] Martin Berthel, Oriane Mollet, Géraldine Dantelle, Thierry Gacoin, Serge Huant, and Aurélien Drezet. Photophysics of single nitrogen-vacancy centers in diamond nanocrystals. *Physical Review B - Condensed Matter and Materials Physics*, 91(3):035308, 2015.

[18] Dolev Bluvstein, Zhiran Zhang, and Ania C.Bleszynski Jayich. Identifying and Mitigating Charge Instabilities in Shallow Diamond Nitrogen-Vacancy Centers. *Physical Review Letters*, 122(7), 2019.

[19] S. K. Sekatskii and V. S. Letokhov. Nanometer-resolution scanning optical microscope with resonance excitation of the fluorescence of the samples from a single-atom excited center. *Journal of Experimental and Theoretical Physics Letters*, 63(5):319–323, 2002.

[20] Boris M. Chernobrod and Gennady P. Berman. Spin microscope based on optically detected magnetic resonance. *Journal of Applied Physics*, 97(1):014903, 2005.

[21] C. L. Degen. Scanning magnetic field microscope with a diamond single-spin sensor. *Applied Physics Letters*, 92(24):243111, 2008.

[22] J. M. Taylor, P. Cappellaro, L. Childress, L. Jiang, D. Budker, P. R. Hemmer, A. Yacoby, R. Walsworth, and M. D. Lukin. High-sensitivity diamond magnetometer with nanoscale resolution. *Nature Physics*, 4(10):810–816, 2008.

[23] Gopalakrishnan Balasubramanian, I. Y. Chan, Roman Kolesov, Mohannad Al-Hmoud, Julia Tisler, Chang Shin, Changdong Kim, Aleksander Wojcik, Philip R. Hemmer, Anke Krueger, Tobias Hanke, Alfred Leitenstorfer, Rudolf Bratschitsch, Fedor Jelezko, and Jörg Wrachtrup. Nanoscale imaging magnetometry with diamond spins under ambient conditions. *Nature*, 455(7213):648–651, 2008.

[24] A Dréau, M Lesik, L Rondin, P Spinicelli, O Arcizet, J. F. Roch, and V Jacques. Avoiding power broadening in optically detected magnetic resonance of single NV defects for enhanced dc magnetic field sensitivity. *Physical Review B - Condensed Matter and Materials Physics*, 84(19):195204, 2011.

[25] B. J. Shields, Q. P. Unterreithmeier, N. P. De Leon, H. Park, and M. D. Lukin. Efficient Readout of a Single Spin State in Diamond via Spin-to-Charge Conversion. *Physical Review Letters*, 114(13):136402, 2015.

[26] Rolf Simon Schoenfeld and Wolfgang Harneit. Real time magnetic field sensing and imaging using a single spin in diamond. *Physical Review Letters*, 106(3), 2011.

[27] Kartiek Agarwal, Richard Schmidt, Bertrand Halperin, Vadim Oganesyan, Gergely Zaránd, Mikhail D. Lukin, and Eugene Demler. Magnetic noise spectroscopy as a probe of local electronic correlations in two-dimensional systems. *Physical Review B*, 95(15):155107, 2017.

[28] Y. Dovzhenko, F. Casola, S. Schlotter, T. X. Zhou, F. Büttner, R. L. Walsworth, G. S. D. Beach, and A. Yacoby. Magnetostatic twists in room-temperature skyrmions explored by nitrogen-vacancy center spin texture reconstruction. *Nature Communications*, 9(1):2712, 2018.

[29] B A Myers, A Ariyaratne, and A. C.Bleszynski Jayich. Double-Quantum Spin-Relaxation Limits to Coherence of Near-Surface Nitrogen-Vacancy Centers. *Physical Review Letters*, 118(19), 2017.

[30] B. A. Myers, A. Das, M. C. Dartiailh, K. Ohno, D. D. Awschalom, and A. C. Bleszynski Jayich. Probing surface noise with depth-calibrated spins in diamond. *Physical Review Letters*, 113(2):027602, 2014.

[31] M Pelliccione, B A Myers, L. M.A. Pascal, A Das, and A. C. Bleszynski Jayich. Two-dimensional nanoscale imaging of gadolinium spins via scanning probe relaxometry with a single spin in diamond. *Physical Review Applied*, 2(5), 2014.

[32] Matthew Pelliccione, Alec Jenkins, Preeti Ovartchaiyapong, Christopher Reetz, Eve Emmanouilidou, Ni Ni, and Ania C Bleszynski Jayich. Scanned probe imaging of nanoscale magnetism at cryogenic temperatures with a single-spin quantum sensor. *Nature Nanotechnology*, 11(8):700–705, 2016.

[33] J. P. Tetienne, T Hingant, J. V. Kim, L. Herrera Diez, J. P. Adam, K Garcia, J. F. Roch, S Rohart, A Thiaville, D Ravelosona, and V Jacques. Nanoscale imaging and control of domain-wall hopping with a nitrogen-vacancy center microscope. *Science*, 344(6190):1366–1369, 2014.

[34] Toeno van der Sar, Francesco Casola, Ronald Walsworth, and Amir Yacoby. Nanometre-scale probing of spin waves using single electron spins. *Nature Communications*, 6(1):7886, 2015.

[35] M. S. Grinolds, S. Hong, P. Maletinsky, L. Luan, M. D. Lukin, R. L. Walsworth, and A. Yacoby. Nanoscale magnetic imaging of a single electron spin under ambient conditions. *Nature Physics*, 9(4):215–219, 2013.

[36] K. Arai, C. Belthangady, H. Zhang, N. Bar-Gill, S. J. DeVience, P. Cappellaro, A. Yacoby, and R. L. Walsworth. Fourier magnetic imaging with nanoscale resolution and compressed sensing speed-up using electronic spins in diamond. *Nature Nanotechnology*, 10(10):859–864, 2015.

[37] I Lovchinsky, A O Sushkov, E Urbach, N. P. De Leon, S Choi, K De Greve, R Evans, R Gertner, E Bersin, C. Muller, L McGuinness, F Jelezko, R L Walsworth, H Park, and M D Lukin. Nuclear magnetic resonance detection and spectroscopy of single proteins using quantum logic. *Science*, 351(6275):836–841, 2016.

[38] D. Rugar, H. J. Mamin, M. H. Sherwood, M. Kim, C. T. Rettner, K. Ohno, and D. D. Awschalom. Proton magnetic resonance imaging using a nitrogen-vacancy spin sensor. *Nature Nanotechnology*, 10(2):120–124, 2015.

[39] T. Häberle, D. Schmid-Lorch, F. Reinhard, and J. Wrachtrup. Nanoscale nuclear magnetic imaging with chemical contrast. *Nature Nanotechnology*, 10(2):125–128, 2015.

[40] Stephen J. Devience, Linh M. Pham, Igor Lovchinsky, Alexander O. Sushkov, Nir Bar-Gill, Chinmay Belthangady, Francesco Casola, Madeleine Corbett, Huiliang Zhang, Mikhail Lukin, Hongkun Park, Amir Yacoby, and Ronald L. Walsworth. Nanoscale NMR spectroscopy and imaging of multiple nuclear species. *Nature Nanotechnology*, 10(2):129–134, 2015.

[41] P Maletinsky, S Hong, M S Grinolds, B Hausmann, M D Lukin, R L Walsworth, M Loncar, and A Yacoby. A robust scanning diamond sensor for nanoscale imaging with single nitrogen-vacancy centres. *Nature Nanotechnology*, 7(5):320–324, 2012.

[42] Thomas Wolf, Philipp Neumann, Kazuo Nakamura, Hitoshi Sumiya, Takeshi Ohshima, Junichi Isoya, and Jörg Wrachtrup. Subpicotesla diamond magnetometry. *Physical Review X*, 5(4):041001, 2015.

[43] Claire A. McLellan, Bryan A. Myers, Stephan Kraemer, Kenichi Ohno, David D. Awschalom, and Ania C. Bleszynski Jayich. Patterned Formation of Highly Coherent Nitrogen-Vacancy Centers Using a Focused Electron Irradiation Technique. *Nano Letters*, 16(4):2450–2454, 2016.

[44] Tim R. Eichhorn, Claire A. McLellan, and Ania C. B. Jayich. Optimizing the formation of depth-confined nitrogen vacancy center spin ensembles in diamond for quantum sensing. *arXiv*, 1901.11519, 2019.

[45] A. A. Wood, A. G. Aeppli, E. Lilette, Y. Y. Fein, A. Stacey, L. C.L. Hollenberg, R. E. Scholten, and A. M. Martin. T2 -limited sensing of static magnetic fields via fast rotation of quantum spins. *Physical Review B*, 98(17):174114, 2018.

[46] A Ajoy, Y X Liu, and P Cappellaro. DC Magnetometry at the T2 Limit. *arXiv*, 1611.04691, 2016.

[47] Rogerio de Sousa. Electron spin as a spectrometer of nuclear-spin noise and other fluctuations. *Topics in Applied Physics*, 115:183–220, 2009.

[48] Bryan Myers. *Quantum decoherence of near-surface nitrogen-vacancy centers in diamond and implications for nanoscale imaging.* PhD thesis, University of California, Santa Barbara, 2016.

[49] N. Bar-Gill, L. M. Pham, C. Belthangady, D. Le Sage, P. Cappellaro, J. R. Maze, M. D. Lukin, A. Yacoby, and R. Walsworth. Suppression of spin-bath dynamics for improved coherence of multi-spin-qubit systems. *Nature Communications*, 3(1):858, 2012.

[50] Dominik Schmid-Lorch, Thomas Häberle, Friedemann Reinhard, Andrea Zappe, Michael Slota, Lapo Bogani, Amit Finkler, and Jörg Wrachtrup. Relaxometry and Dephasing Imaging of Superparamagnetic Magnetite Nanoparticles Using a Single Qubit. *Nano Letters*, 15(8):4942–4947, 2015.

[51] Amila Ariyaratne, Dolev Bluvstein, Bryan A. Myers, and Ania C.Bleszynski Jayich. Nanoscale electrical conductivity imaging using a nitrogen-vacancy center in diamond. *Nature Communications*, 9(1):2406, 2018.

[52] Chunhui Du, Toeno van der Sar, Tony X Zhou, Pramey Upadhyaya, Francesco Casola, Huiliang Zhang, Mehmet C Onbasli, Caroline A Ross, Ronald L Walsworth, Yaroslav Tserkovnyak, and Amir Yacoby. Control and local measurement of the spin chemical potential in a magnetic insulator. *Science*, 357(6347):195–198, 2017.

[53] B. Flebus and Y. Tserkovnyak. Quantum-Impurity Relaxometry of Magnetization Dynamics. *Physical Review Letters*, 121(18):187204, 2018.

[54] Boris Naydenov, Friedemann Reinhard, Anke Lämmle, V. Richter, Rafi Kalish, Ulrika F.S. D'Haenens-Johansson, Mark Newton, Fedor Jelezko, and Jörg Wrachtrup. Increasing the coherence time of single electron spins in diamond by high temperature annealing. *Applied Physics Letters*, 97(24):242511, 2010.

[55] Kenichi Ohno, F. Joseph Heremans, Lee C. Bassett, Bryan A. Myers, David M. Toyli, Ania C. Bleszynski Jayich, Christopher J. Palmstrøm, and David D. Awschalom. Engineering shallow spins in diamond with nitrogen delta-doping. *Applied Physics Letters*, 101(8):082413, 2012.

[56] K. M C Fu, C. Santori, P. E. Barclay, and R. G. Beausoleil. Conversion of neutral nitrogen-vacancy centers to negatively charged nitrogen-vacancy centers through selective oxidation. *Applied Physics Letters*, 96(12):121907, 2010.

[57] M. V. Hauf, B. Grotz, B. Naydenov, M. Dankerl, S. Pezzagna, J. Meijer, F. Jelezko, J. Wrachtrup, M. Stutzmann, F. Reinhard, and J. A. Garrido. Chemical control of the charge state of nitrogen-vacancy centers in diamond. *Physical Review B - Condensed Matter and Materials Physics*, 83(8):081304, 2011.

[58] B. A. Myers, A. Ariyaratne, and A. C. Bleszynski Jayich. Double-Quantum Spin-Relaxation Limits to Coherence of Near-Surface Nitrogen-Vacancy Centers. *Physical Review Letters*, 118(19):197201, 2017.

[59] Moloud Kaviani, Peter Deák, Bálint Aradi, Thomas Frauenheim, Jyh Pin Chou, and Adam Gali. Proper surface termination for luminescent near-surface NV centers in diamond. *Nano Letters*, 14(8):4772–4777, 2014.

[60] F. Y. Xie, W. G. Xie, L. Gong, W. H. Zhang, S. H. Chen, Q. Z. Zhang, and J. Chen. Surface characterization on graphitization of nanodiamond powder annealed in nitrogen ambient. *Surface and Interface Analysis*, 42(9):1514–1518, 2010.

[61] Shanying Cui. *Near-surface Nitrogen Vacancy Centers in Diamond*. PhD thesis, Harvard University, 2014.

[62] Alastair Stacey, Nikolai Dontschuk, Jyh Pin Chou, David A. Broadway, Alex K. Schenk, Michael J. Sear, Jean Philippe Tetienne, Alon Hoffman, Steven Prawer, Chris I. Pakes, Anton Tadich, Nathalie P. de Leon, Adam Gali, and Lloyd C.L. Hollenberg. Evidence for Primal sp 2 Defects at the Diamond Surface: Candidates for Electron Trapping and Noise Sources. *Advanced Materials Interfaces*, 6(3):1801449, 2019.

[63] M. Kim, H. J. Mamin, M. H. Sherwood, C. T. Rettner, J. Frommer, and D. Rugar. Effect of oxygen plasma and thermal oxidation on shallow nitrogen-vacancy centers in diamond. *Applied Physics Letters*, 105(4):042406, 2014.

[64] L Rondin, J. P. Tetienne, S Rohart, A Thiaville, T Hingant, P Spinicelli, J. F. Roch, and V Jacques. Stray-field imaging of magnetic vortices with a single diamond spin. *Nature Communications*, 4, 2013.

[65] J. P. Tetienne, T Hingant, L J Martínez, S Rohart, A Thiaville, L. Herrera Diez, K Garcia, J. P. Adam, J. V. Kim, J. F. Roch, I M Miron, G Gaudin, L Vila, B Ocker, D Ravelosona, and V Jacques. The nature of domain walls in ultrathin ferromagnets revealed by scanning nanomagnetometry. *Nature Communications*, 6, 2015.

[66] I. Gross, L. J. Martínez, J.-P. Tetienne, T. Hingant, J.-F. Roch, K. Garcia, R. Soucaille, J. P. Adam, J.-V. Kim, S. Rohart, A. Thiaville, J. Torrejon, M. Hayashi, and V. Jacques. Direct measurement of interfacial Dzyaloshinskii-Moriya interaction in X—CoFeB—MgO heterostructures with a scanning NV magnetometer (X=Ta, TaN, and W). *Physical Review B*, 94(6):064413, 2016.

[67] I. Gross, W. Akhtar, V. Garcia, L. J. Martínez, S. Chouaieb, K. Garcia, C. Carrétéro, A. Barthélémy, P. Appel, P. Maletinsky, J. V. Kim, J. Y. Chauleau, N. Jaouen, M. Viret, M. Bibes, S. Fusil, and V. Jacques. Real-space imaging of non-collinear antiferromagnetic order with a single-spin magnetometer. *Nature*, 549(7671):252–256, 2017.

[68] I. Gross, W. Akhtar, A. Hrabec, J. Sampaio, L. J. Martínez, S. Chouaieb, B. J. Shields, P. Maletinsky, A. Thiaville, S. Rohart, and V. Jacques. Skyrmion morphology in ultrathin magnetic films. *Physical Review Materials*, 024406(2):1–6, 2018.

[69] Patrick Appel, Brendan J. Shields, Tobias Kosub, Natascha Hedrich, René Hübner, Jürgen Faßbender, Denys Makarov, and Patrick Maletinsky. Nanomagnetism of Magnetoelectric Granular Thin-Film Antiferromagnets. *Nano Letters*, 19(3):1682–1687, 2019.

[70] L Thiel, Z Wang, M A Tschudin, D Rohner, I Gutiérrez-Lezama, N Ubrig, M Gibertini, E Giannini, A F Morpurgo, and P Maletinsky. Probing magnetism in 2d materials at the nanoscale with single-spin microscopy. *Science*, 364(6444):973–976, 2019.

[71] Soonwon Choi, Joonhee Choi, Renate Landig, Georg Kucsko, Hengyun Zhou, Junichi Isoya, Fedor Jelezko, Shinobu Onoda, Hitoshi Sumiya, Vedika Khemani, Curt Von Keyserlingk, Norman Y. Yao, Eugene Demler, and Mikhail D. Lukin. Observation of discrete time-crystalline order in a disordered dipolar many-body system. *Nature*, 543(7644):221–225, 2017.

[72] Joonhee Choi, Hengyun Zhou, Soonwon Choi, Renate Landig, Wen Wei Ho, Junichi Isoya, Fedor Jelezko, Shinobu Onoda, Hitoshi Sumiya, Dmitry A Abanin, and

Mikhail D Lukin. Probing Quantum Thermalization of a Disordered Dipolar Spin Ensemble with Discrete Time-Crystalline Order. *Physical Review Letters*, 122(4), 2019.

[73] S Pezzagna, B Naydenov, F Jelezko, J Wrachtrup, and J Meijer. Creation efficiency of nitrogen-vacancy centres in diamond. *New Journal of Physics*, 12(6):065017, 2010.

[74] Jane Y. Howe, Linda E. Jones, and Dorothy W. Coffey. The evolution of microstructure of CVD diamond by oxidation. *Carbon*, 38(6):931–933, 2000.

[75] S. Ali Momenzadeh, Rainer J. Stöhr, Felipe Favaro De Oliveira, Andreas Brunner, Andrej Denisenko, Sen Yang, Friedemann Reinhard, and Jörg Wrachtrup. Nano-engineered diamond waveguide as a robust bright platform for nanomagnetometry using shallow nitrogen vacancy centers. *Nano Letters*, 15(1):165–169, 2015.

[76] Philipp Fuchs, Michel Challier, and Elke Neu. Optimized single-crystal diamond scanning probes for high sensitivity magnetometry. *New Journal of Physics*, 20(12):125001, 2018.

[77] Noel H Wan, Brendan J Shields, Donggyu Kim, Sara Mouradian, Benjamin Lienhard, Michael Walsh, Hassaram Bakhru, Tim Schröder, and Dirk Englund. Efficient Extraction of Light from a Nitrogen-Vacancy Center in a Diamond Parabolic Reflector. *Nano Letters*, 18(5):2787–2793, 2018.

[78] Zhi Hui Wang and Susumu Takahashi. Spin decoherence and electron spin bath noise of a nitrogen-vacancy center in diamond. *Physical Review B - Condensed Matter and Materials Physics*, 87(11):115122, 2013.

[79] Matthew Pelliccione. *Local imaging of high mobility two-dimensional electron systems with virtual scanning tunneling microscopy*. PhD thesis, Stanford, 2013.

[80] L. Thiel, D. Rohner, M. Ganzhorn, P. Appel, E. Neu, B. Müller, R. Kleiner, D. Koelle, and P. Maletinsky. Quantitative nanoscale vortex imaging using a cryogenic quantum magnetometer. *Nature Nanotechnology*, 11(8):677–681, 2016.

[81] Alec Jenkins, Matthew Pelliccione, Guoqiang Yu, Xin Ma, Xiaoqin Li, Kang L. Wang, and Ania C. Bleszynski Jayich. Single spin sensing of domain wall structure and dynamics in a thin film skyrmion host. *Physical Review Materials*, 3(8):083801, 2019.

[82] Guoqiang Yu, Alec Jenkins, Xin Ma, Seyed Armin Razavi, Congli He, Gen Yin, Qiming Shao, Qing lin He, Hao Wu, Wenjing Li, Wanjun Jiang, Xiufeng Han, Xiaoqin Li, Ania Claire Bleszynski Jayich, Pedram Khalili Amiri, and Kang L. Wang. Room-Temperature Skyrmions in an Antiferromagnet-Based Heterostructure. *Nano Letters*, 18(2):980–986, 2018.

171

[83] S. Mühlbauer, B. Binz, F. Jonietz, C. Pfleiderer, A. Rosch, A. Neubauer, R. Georgii, and P. Böni. Skyrmion lattice in a chiral magnet. *Science*, 323(5916), 2009.

[84] X Z Yu, N Kanazawa, Y Onose, K Kimoto, W Z Zhang, S Ishiwata, Y Matsui, and Y Tokura. Near room-temperature formation of a skyrmion crystal in thin-films of the helimagnet FeGe. *Nature Materials*, 10(2):106–109, 2011.

[85] Stefan Heinze, Kirsten Von Bergmann, Matthias Menzel, Jens Brede, André Kubetzka, Roland Wiesendanger, Gustav Bihlmayer, and Stefan Blügel. Spontaneous atomic-scale magnetic skyrmion lattice in two dimensions. *Nature Physics*, 7(9):713–718, 2011.

[86] T Schulz, R Ritz, A Bauer, M Halder, M Wagner, C Franz, C Pfleiderer, K Everschor, M Garst, and A Rosch. Emergent electrodynamics of skyrmions in a chiral magnet. *Nature Physics*, 8(4):301–304, 2012.

[87] F. Jonietz, S. Mühlbauer, C. Pfleiderer, A. Neubauer, W. Münzer, A. Bauer, T. Adams, R. Georgii, P. Böni, R. A. Duine, K. Everschor, M. Garst, and A. Rosch. Spin Transfer Torques in MnSi at Ultralow Current Densities. *Science*, 330(6011), 2010.

[88] J Sampaio, V Cros, S Rohart, A Thiaville, and A Fert. Nucleation, stability and current-induced motion of isolated magnetic skyrmions in nanostructures. *Nature Nanotechnology*, 8, 2013.

[89] Albert Fert, Vincent Cros, and Joao Sampaio. Skyrmions on the track. *Nat Nano*, 8(3):152–156, 2013.

[90] X Z Yu, N Kanazawa, WZ Zhang, T Nagai, T Hara, K Kimoto, Y Matsui, Y Onose, and Y Tokura. Skyrmion flow near room temperature in an ultralow current density. *Nature Communications*, 3:988, 2012.

[91] Niklas Romming, Christian Hanneken, Matthias Menzel, Jessica E Bickel, Boris Wolter, Kirsten von Bergmann, André Kubetzka, and Roland Wiesendanger. Writing and Deleting Single Magnetic Skyrmions. *Science*, 341(6146):636 LP – 639, 2013.

[92] S Rohart, J Miltat, and A Thiaville. Path to collapse for an isolated N\'eel skyrmion. *PHYSICAL REVIEW B*, 93:214412, 2016.

[93] Seonghoon Woo, Kai Litzius, Benjamin Krüger, Mi Young Im, Lucas Caretta, Kornel Richter, Maxwell Mann, Andrea Krone, Robert M Reeve, Markus Weigand, Parnika Agrawal, Ivan Lemesh, Mohamad Assaad Mawass, Peter Fischer, Mathias Kläui, and Geoffrey S.D. Beach. Observation of room-temperature magnetic skyrmions and their current-driven dynamics in ultrathin metallic ferromagnets. *Nature Materials*, 15(5):501–506, 2016.

[94] Guoqiang Yu, Pramey Upadhyaya, Xiang Li, Wenyuan Li, Se Kwon Kim, Yabin Fan, Kin L. Wong, Yaroslav Tserkovnyak, Pedram Khalili Amiri, and Kang L. Wang. Room-Temperature Creation and Spin–Orbit Torque Manipulation of Skyrmions in Thin Films with Engineered Asymmetry. *Nano Letters*, 16(3):1981–1988, 2016.

[95] C Moreau-Luchaire, C Moutafis, N Reyren, J Sampaio, C. A.F. Vaz, N. Van Horne, K Bouzehouane, K Garcia, C Deranlot, P Warnicke, P Wohlhüter, J. M. George, M Weigand, J Raabe, V Cros, and A Fert. Additive interfacial chiral interaction in multilayers for stabilization of small individual skyrmions at room temperature. *Nature Nanotechnology*, 11(5):444–448, 2016.

[96] Anjan Soumyanarayanan, M Raju, A. L.Gonzalez Oyarce, Anthony K.C. Tan, Mi Young Im, A. P. Petrovic, Pin Ho, K H Khoo, M Tran, C K Gan, F Ernult, and C Panagopoulos. Tunable room-temperature magnetic skyrmions in Ir/Fe/Co/Pt multilayers. *Nature Materials*, 16(9):898–904, 2017.

[97] Albert Fert, Nicolas Reyren, and Vincent Cros. Magnetic skyrmions: Advances in physics and potential applications, 2017.

[98] A. Bogdanov and A. Hubert. Thermodynamically stable magnetic vortex states in magnetic crystals. *Journal of Magnetism and Magnetic Materials*, 138(3):255–269, 1994.

[99] S. Rohart and A. Thiaville. Skyrmion confinement in ultrathin film nanostructures in the presence of Dzyaloshinskii-Moriya interaction. *Physical Review B*, 88(18):184422, 2013.

[100] Xin Ma, Guoqiang Yu, Xiang Li, Tao Wang, Di Wu, Kevin S. Olsson, Zhaodong Chu, Kyongmo An, John Q. Xiao, Kang L. Wang, and Xiaoqin Li. Interfacial control of Dzyaloshinskii-Moriya interaction in heavy metal/ferromagnetic metal thin film heterostructures. *Physical Review B*, 94(18):180408(R), 2016.

[101] Xin Ma, Guoqiang Yu, Seyed A. Razavi, Stephen S. Sasaki, Xiang Li, Kai Hao, Sarah H. Tolbert, Kang L. Wang, and Xiaoqin Li. Dzyaloshinskii-Moriya Interaction across an Antiferromagnet-Ferromagnet Interface. *Physical Review Letters*, 119(2):027202, 2017.

[102] Xin Ma, Guoqiang Yu, Chi Tang, Xiang Li, Congli He, Jing Shi, Kang L. Wang, and Xiaoqin Li. Interfacial Dzyaloshinskii-Moriya Interaction: Effect of 5d Band Filling and Correlation with Spin Mixing Conductance. *Physical Review Letters*, 120(15):157204, 2018.

[103] H Ohldag, A Scholl, F Nolting, E Arenholz, S Maat, A T Young, M Carey, and J Stöhr. Correlation between Exchange Bias and Pinned Interfacial Spins. *Physical Review Letters*, 91(1), 2003.

[104] J Geshev, T Dias, S Nicolodi, R Cichelero, A Harres, J. J.S. Acuna, L G Pereira, J E Schmidt, C Deranlot, and F Petroff. Role of the uncompensated interface spins in polycrystalline exchange-biased systems. *Journal of Physics D: Applied Physics*, 44(9):095002, 2011.

[105] A. A. Thiele. Theory of the static stability of cylindrical domains in uniaxial platelets. *Journal of Applied Physics*, 41(3):1139–1145, 1970.

[106] M. Eltschka, M. Wötzel, J. Rhensius, S. Krzyk, U. Nowak, M. Kläui, T. Kasama, R. E. Dunin-Borkowski, L. J. Heyderman, H. J. van Driel, and R. A. Duine. Nonadiabatic Spin Torque Investigated Using Thermally Activated Magnetic Domain Wall Dynamics. *Physical Review Letters*, 105(5):056601, 2010.

[107] N. Bloembergen, E. M. Purcell, and R. V. Pound. Relaxation Effects in Nuclear Magnetic Resonance Absorption. *Physical Review*, 73(7):679–712, 1948.

[108] J. Li, M. P. Silveri, K. S. Kumar, J. M. Pirkkalainen, A. Vepsäläinen, W. C. Chien, J. Tuorila, M. A. Sillanpää, P. J. Hakonen, E. V. Thuneberg, and G. S. Paraoanu. Motional averaging in a superconducting qubit. *Nature Communications*, 4(1):1420, 2013.

[109] M. Kronseder, T. N.G. Meier, M. Zimmermann, M. Buchner, M. Vogel, and C. H. Back. Real-time observation of domain fluctuations in a two-dimensional magnetic model system. *Nature Communications*, 6(1):6832, 2015.

[110] M Mochizuki, X Z Yu, S Seki, N Kanazawa, W Koshibae, J Zang, M Mostovoy, Y. Tokura, and N. Nagaosa. Thermally driven ratchet motion of a skyrmion microcrystal and topological magnon Hall effect. *Nature Materials*, 13(3):241–246, 2014.

[111] K Wagner, A Kákay, K. Schultheiss, A Henschke, T Sebastian, and H Schultheiss. Magnetic domain walls as reconfigurable spin-wave nanochannels. *Nature Nanotechnology*, 11(5):432–436, 2016.

[112] Xiuzhen Yu, Daisuke Morikawa, Tomoyuki Yokouchi, Kiyou Shibata, Naoya Kanazawa, Fumitaka Kagawa, Taka hisa Arima, and Yoshinori Tokura. Aggregation and collapse dynamics of skyrmions in a non-equilibrium state. *Nature Physics*, 14(8):832–836, 2018.

[113] J. A. Cape and G. W. Lehman. Magnetic domain structures in thin uniaxial plates with perpendicular easy axis. *Journal of Applied Physics*, 42(13):5732–5756, 1971.

[114] Wanjun Jiang, Xichao Zhang, Guoqiang Yu, Wei Zhang, Xiao Wang, M. Benjamin Jungfleisch, John E Pearson, Xuemei Cheng, Olle Heinonen, Kang L Wang, Yan Zhou, Axel Hoffmann, and Suzanne G.E. Te Velthuis. Direct observation of the skyrmion Hall effect. *Nature Physics*, 13(2):162–169, 2017.

[115] A Neubauer, C Pfleiderer, B Binz, A Rosch, R Ritz, P G Niklowitz, and P Böni. Topological Hall effect in the A-phase of MnSi. *Physical Review Letters*, 102(18):186602, 2009.

[116] R. Tomasello, E. Martinez, R. Zivieri, L. Torres, M. Carpentieri, and G. Finocchio. A strategy for the design of skyrmion racetrack memories. *Scientific Reports*, 4(1):6784, 2014.

[117] Kai Litzius, Ivan Lemesh, Benjamin Krüger, Pedram Bassirian, Lucas Caretta, Kornel Richter, Felix Büttner, Koji Sato, Oleg A. Tretiakov, Johannes Förster, Robert M. Reeve, Markus Weigand, Iuliia Bykova, Hermann Stoll, Gisela Schütz, Geoffrey S.D. Beach, and Mathias Klaüi. Skyrmion Hall effect revealed by direct time-resolved X-ray microscopy. *Nature Physics*, 13(2):170–175, 2017.

[118] T. Hingant, J. P. Tetienne, L. J. Martínez, K. Garcia, D. Ravelosona, J. F. Roch, and V. Jacques. Measuring the magnetic moment density in patterned ultrathin ferromagnets with submicrometer resolution. *Physical Review Applied*, 4(1):014003, 2015.

[119] M T. Johnson, P J H. Bloemen, F J A. den Broeder, and J J. de Vries. Magnetic anisotropy in metallic multilayers. *Rep. Prog. Phys*, 59:1409–1458, 1996.

[120] Soo Young Jang, S. H. Lim, and S. R. Lee. Magnetic dead layer in amorphous CoFeB layers with various top and bottom structures. *Journal of Applied Physics*, 107(9):09C707, 2010.

[121] Jaivardhan Sinha, Masamitsu Hayashi, Andrew J. Kellock, Shunsuke Fukami, Michihiko Yamanouchi, Hideo Sato, Shoji Ikeda, Seiji Mitani, See Hun Yang, Stuart S. P. Parkin, and Hideo Ohno. Enhanced interface perpendicular magnetic anisotropy in Ta—CoFeB—MgO using nitrogen doped Ta underlayers. *Applied Physics Letters*, 102(24):242405, 2013.

[122] Benjamin Buford, Pallavi Dhagat, and Albrecht Jander. Estimating exchange stiffness of thin films with perpendicular anisotropy using magnetic domain images. *IEEE Magnetics Letters*, 7:1–5, 2016.

[123] M J. Donahue and D G. Porter. OOMMF User's Guide, Version 1.0. Technical report, NIST, 1999.

[124] Niculin Andri Saratz. *Inverse Symmetry Breaking in Low-Dimensional Systems*. PhD thesis, ETH Zurich, 2010.

[125] Eduardo A. Lima and Benjamin P. Weiss. Obtaining vector magnetic field maps from single-component measurements of geological samples. *Journal of Geophysical Research: Solid Earth*, 114(6), 2009.

[126] K. Zeissler, M. Mruczkiewicz, S. Finizio, J. Raabe, P. M. Shepley, A. V. Sadovnikov, S. A. Nikitov, K. Fallon, S. McFadzean, S. McVitie, T. A. Moore, G. Burnell, and C. H. Marrows. Pinning and hysteresis in the field dependent diameter evolution of skyrmions in Pt/Co/Ir superlattice stacks. *Scientific Reports*, 7(1):15125, 2017.

[127] F Jonietz, S Mühlbauer, C Pfleiderer, A Neubauer, W Münzer, A Bauer, T Adams, R Georgii, P Böni, R A Duine, K Everschor, M Garst, and A Rosch. Spin transfer torques in MnSi at ultralow current densities. *Science*, 330(6011):1648–1651, 2010.

[128] Y. Tokunaga, X. Z. Yu, J. S. White, H. M. Rønnow, D. Morikawa, Y. Taguchi, and Y. Tokura. A new class of chiral materials hosting magnetic skyrmions beyond room temperature. *Nature Communications*, 6(1):7638, 2015.

[129] Joshua D. Bocarsly, Colin Heikes, Craig M. Brown, Stephen D. Wilson, and Ram Seshadri. Deciphering structural and magnetic disorder in the chiral skyrmion host materials CoxZnyMnz (x+y+z=20). *Physical Review Materials*, 3(1):014402, 2019.

[130] B Fåk, R A Sadykov, J Flouquet, and G Lapertot. Pressure dependence of the magnetic structure of the itinerant electron magnet MnSi. *Journal of Physics Condensed Matter*, 17(10):1635–1644, 2005.

[131] K. Shibata, J. Iwasaki, N. Kanazawa, S. Aizawa, T. Tanigaki, M. Shirai, T. Nakajima, M. Kubota, M. Kawasaki, H. S. Park, D. Shindo, N. Nagaosa, and Y. Tokura. Large anisotropic deformation of skyrmions in strained crystal. *Nature Nanotechnology*, 10(7):589–592, 2015.

[132] L. W. Molenkamp and M. J.M. de Jong. Observation of Knudsen and Gurzhi transport regimes in a two-dimensional wire. *Solid State Electronics*, 37(4-6):551–553, 1994.

[133] M. J.M. De Jong and L. W. Molenkamp. Hydrodynamic electron flow in high-mobility wires. *Physical Review B*, 51(19):13389–13402, 1995.

[134] Philip J.W. Moll, Pallavi Kushwaha, Nabhanila Nandi, Burkhard Schmidt, and Andrew P Mackenzie. Evidence for hydrodynamic electron flow in PdCoO2. *Science*, 351(6277):1061–1064, 2016.

[135] R. Krishna Kumar, D. A. Bandurin, F. M.D. Pellegrino, Y. Cao, A. Principi, H. Guo, G. H. Auton, M. Ben Shalom, L. A. Ponomarenko, G. Falkovich, K. Watanabe, T. Taniguchi, I. V. Grigorieva, L. S. Levitov, M. Polini, and A. K. Geim. Superballistic flow of viscous electron fluid through graphene constrictions. *Nature Physics*, 13(12):1182–1185, 2017.

[136] D A Bandurin, I Torre, R Krishna Kumar, M Ben Shalom, A Tomadin, A Principi, G H Auton, E Khestanova, K S Novoselov, I V Grigorieva, L A Ponomarenko, A K

Geim, and M Polini. Negative local resistance caused by viscous electron backflow in graphene. *Science*, 351(6277):1055–1058, 2016.

[137] Andrew Lucas and Sean A Hartnoll. Resistivity bound for hydrodynamic bad metals. *PNAS*, 114(43), 2017.

[138] P. R. Wallace. The band theory of graphite. *Physical Review*, 71(9):622–634, 1947.

[139] K. S. Novoselov, A. K. Geim, S. V. Morozov, D. Jiang, M. I. Katsnelson, I. V. Grigorieva, S. V. Dubonos, and A. A. Firsov. Two-dimensional gas of massless Dirac fermions in graphene. *Nature*, 438(7065):197–200, 2005.

[140] C. R. Dean, A. F. Young, I. Meric, C. Lee, L. Wang, S. Sorgenfrei, K. Watanabe, T. Taniguchi, P. Kim, K. L. Shepard, and J. Hone. Boron nitride substrates for high-quality graphene electronics. *Nature nanotechnology*, 5(10):722–6, 2010.

[141] Dmitri K Efetov and Philip Kim. Controlling electron-phonon interactions in graphene at ultrahigh carrier densities. *Physical Review Letters*, 105(25), 2010.

[142] Jian Hao Chen, Chaun Jang, Shudong Xiao, Masa Ishigami, and Michael S. Fuhrer. Intrinsic and extrinsic performance limits of graphene devices on SiO 2. *Nature Nanotechnology*, 3(4):206–209, 2008.

[143] R. N. Gurzhi. Minimum of Resistance in Impurity Free Conductors. *Sov. Phys. JETP*, 27:1019, 1968.

[144] Jesse Crossno, Jing K Shi, Ke Wang, Xiaomeng Liu, Achim Harzheim, Andrew Lucas, Subir Sachdev, Philip Kim, Takashi Taniguchi, Kenji Watanabe, Thomas A Ohki, and Kin Chung Fong. Observation of the Dirac fluid and the breakdown of the Wiedemann-Franz law in graphene. *Science*, 351(6277):1058–1061, 2016.

[145] Leonid Levitov and Gregory Falkovich. Electron viscosity, current vortices and negative nonlocal resistance in graphene. *Nature Physics*, 12(7):672–676, 2016.

[146] Alessandro Principi and Giovanni Vignale. Violation of the Wiedemann-Franz Law in Hydrodynamic Electron Liquids. *Physical Review Letters*, 115(5), 2015.

[147] J. Gooth, F. Menges, N. Kumar, V. Süβ, C. Shekhar, Y. Sun, U. Drechsler, R. Zierold, C. Felser, and B. Gotsmann. Thermal and electrical signatures of a hydrodynamic electron fluid in tungsten diphosphide. *Nature Communications*, 9(1):4093, 2018.

[148] Denis A. Bandurin, Andrey V. Shytov, Leonid S. Levitov, Roshan Krishna Kumar, Alexey I. Berdyugin, Moshe Ben Shalom, Irina V. Grigorieva, Andre K. Geim, and Gregory Falkovich. Fluidity onset in graphene. *Nature Communications*, 9(1):4533, 2018.

[149] Haoyu Guo, Ekin Ilseven, Gregory Falkovich, and Leonid S Levitov. Higher-than-ballistic conduction of viscous electron flows. *Proceedings of the National Academy of Sciences*, 114(12):3068–3073, 2017.

[150] Andrew Lucas and Kin Chung Fong. Hydrodynamics of electrons in graphene. *Journal of Physics Condensed Matter*, 30(5):053001, 2018.

[151] Egor I Kiselev and Jörg Schmalian. Boundary conditions of viscous electron flow. *Physical Review B*, 99(3):35430, 2019.

[152] Joseph A. Sulpizio, Lior Ella, Asaf Rozen, John Birkbeck, David J. Perello, Debarghya Dutta, Moshe Ben-Shalom, Takashi Taniguchi, Kenji Watanabe, Tobias Holder, Raquel Queiroz, Ady Stern, Thomas Scaffidi, Andre K. Geim, and Shahal Ilani. Visualizing Poiseuille flow of hydrodynamic electrons. *arXiv*, 2019.

[153] A. A. Zibrov, C. Kometter, H. Zhou, E. M. Spanton, T. Taniguchi, K. Watanabe, M. P. Zaletel, and A. F. Young. Tunable interacting composite fermion phases in a half-filled bilayer-graphene Landau level. *Nature*, 549(7672):360–364, 2017.

[154] Gregory Falkovich and Leonid Levitov. Linking Spatial Distributions of Potential and Current in Viscous Electronics. *Physical Review Letters*, 119(6), 2017.

[155] Haoyu Guo. *Signatures of Hydrodynamic Transport in an Electron System*. PhD thesis, MIT, 2018.

[156] Bradley J. Roth, Nestor G. Sepulveda, and John P. Wikswo. Using a magnetometer to image a two-dimensional current distribution. *Journal of Applied Physics*, 65(1):361–372, 1989.

[157] K. Chang, A. Eichler, J. Rhensius, L. Lorenzelli, and C. L. Degen. Nanoscale Imaging of Current Density with a Single-Spin Magnetometer. *Nano Letters*, 17(4):2367–2373, 2017.

[158] Gabriele F Giuliani and John J Quinn. Lifetime of a quasiparticle in a two-dimensional electron gas. *PHYSICAL REVIEW B*, 26(8):4421, 1982.

[159] L Wang, I Meric, P Y Huang, Q. Gao, Y Gao, H Tran, T Taniguchi, K Watanabe, L M Campos, D A Muller, J Guo, P Kim, J Hone, K L Shepard, and C R Dean. One-dimensional electrical contact to a two-dimensional material. *Science*, 342(6158):614–617, 2013.

[160] Karina A. Guerrero-Becerra, Francesco M.D. Pellegrino, and Marco Polini. Magnetic hallmarks of viscous electron flow in graphene. *Physical Review B*, 99(4):041407, 2019.

[161] H. Polshyn, M. Yankowitz, S. Chen, Y. Zhang, K. Watanabe, T. Taniguchi, C. R. Dean, and A. F. Young. Phonon scattering dominated electron transport in twisted bilayer graphene. *arXiv*, 2019.

[162] André Thiaville, Stanislas Rohart, Emilie Jué, Vincent Cros, and Albert Fert. Dynamics of Dzyaloshinskii domain walls in ultrathin magnetic films. *EPL*, 100:57002–p1–p6, 2012.

[163] S. Dreyer, J. Norpoth, C. Jooss, S. Sievers, U. Siegner, V. Neu, and T. H. Johansen. Quantitative imaging of stray fields and magnetization distributions in hard magnetic element arrays. *Journal of Applied Physics*, 101(8), 2007.

[164] M. Baćani, M. A. Marioni, J. Schwenk, and H. J. Hug. How to measure the local Dzyaloshinskii Moriya Interaction in Skyrmion Thin Film Multilayers. *arXiv*, page 1611.00673, 2016.

[165] F. Dolde, H. Fedder, M. W. Doherty, T. Nöbauer, F. Rempp, G. Balasubramanian, T. Wolf, F. Reinhard, L. C.L. Hollenberg, F. Jelezko, and J. Wrachtrup. Electric-field sensing using single diamond spins. *Nature Physics*, 7(6):459–463, 2011.

[166] Eric Van Oort and Max Glasbeek. Electric-field-induced modulation of spin echoes of N-V centers in diamond. *Chemical Physics Letters*, 168(6):529–532, 1990.